UNICA

UNIVERSITÀ
DEGLI STUDI
DI CAGLIARI

Ph.D. DEGREE IN
Electronic and Computer Engineering

Cycle XXXVIII

TITLE OF THE Ph.D. THESIS

Data Trustworthiness in Synchronized Power System Measurements: Algorithms and Methodologies

Scientific Disciplinary Sector
IMIS-01/B

Ph.D. Student	Davide Sitzia
Supervisor	Prof. Paolo Castello
Co-Supervisor	Prof. Paolo Attilio Pegoraro

Final exam. Academic Year 2024/2025
Thesis defence session: February 2026

Contents

Introduction

Climate change is reshaping the life of modern societies, representing one of the most urgent and complex challenges of the XXI century. Achieving global climate targets requires, among others, a profound transformation of energy systems, driving them towards decarbonization and sustainability. In this context, the increasing penetration of renewable and distributed energy resources, together with the electrification of mobility, is pushing the power grid closer to its operational limits. While essential for reducing greenhouse gas emissions, this transition introduces new forms of variability and uncertainty, making it necessary to monitor and control power systems with unprecedented accuracy and promptness. Ensuring stability, resilience, and efficiency therefore critically depends on the availability of high-quality measurement data.

To address these new challenges, power systems are undergoing a major digitalization process to increase the efficiency and reliability of monitoring, control, and protection applications. The digital transformation of power systems is paving the way for a new generation of architectures and devices, such as Merging Units (MUs) and Intelligent Electronic Devices (IEDs), which respectively digitize and analyze electrical signals. IEDs can implement several functionalities, including synchrophasor estimation, power quality analysis, and fault detection, thus integrating, within a single device, tasks that were traditionally carried out by dedicated instruments such as Phasor Measurement Units (PMUs), Power Quality Meters (PQMs), and Digital Fault Recorders (DFRs). Nonetheless, long-standing devices are still widely employed by system operators, and interoperability between them must therefore be ensured.

In this scenario, measurement science assumes a crucial role. The reliability of these applications depends on the ability to characterize, validate, and guarantee the quality of data streams. Accurate measurements are an essential prerequisite for reliable monitoring, control, and automation of power systems. Ensuring such quality requires accurate characterization of measurement instruments under controlled conditions, where sources of uncertainty due to input signal variability or external influences can be minimized. Complete charac-

terization, in turn, requires in-depth analysis of device functionality, including measurement outputs, synchronization, and data communication.

Building on these considerations, this thesis proposes a set of methodologies, algorithms, and analysis tools to enhance measurement data quality and ensure reliability in modern power system applications. The proposed techniques are analyzed, implemented, and optimized in the context of synchronized measurements in power systems.

The work is organized into four chapters, structured as follows:

- Chapter 1 introduces the context of the thesis, describing the architectures of modern synchronized power system monitoring and the main instruments involved. Particular emphasis is placed on the sources of uncertainty in electrical measurements and on how these influence the reliability and interpretability of the acquired data. The chapter also addresses Power Quality (PQ), a crucial aspect of modern power grids whose monitoring has become increasingly important to enhance the trustworthiness of measurement data and the overall reliability of the system.

- Chapter 2 addresses the detection of anomalies in measurement data flows, focusing on time series analysis for event identification. In this context, the Matrix Profile (MP) is introduced and adapted to power system measurements, demonstrating its effectiveness for real-time event detection in both Sampled Value (SV) and synchrophasor data streams.

- Chapter 3 deals with the statistical modeling of synchrophasor measurement errors. It presents a comprehensive methodology for the analysis of PMU data aimed at identifying intrinsic uncertainty sources and mitigating the effects of external influences, thereby improving the robustness of the resulting error models. Finally, statistical models are proposed for both Magnitude Errors (MEs) and Phase-Angle Errors (PEs).

- Chapter 4 explores the White Rabbit (WR) synchronization protocol as a means for accurate time distribution in modern electrical substations and monitoring architectures. The discussion focuses on the architectural aspects of synchronization distribution, emphasizing its contribution to enhancing data quality for advanced applications such as harmonic synchrophasor estimation and high-rate signal acquisition through devices like MUs. To this end, an Field Programmable Gate Array (FPGA)-based solution is proposed for disciplining the end-device clock, aimed at optimizing system determinism.

- Finally, the Conclusions summarize the main outcomes of the work and discuss their implications and possible future developments.

Chapter 1

Architectures and instrumentation for synchronized power system monitoring

Modern power systems are increasingly complex and dynamic, driven by the growing penetration of renewable energy sources and distributed generation. This evolution is reshaping traditional monitoring and control paradigms, making it essential to acquire high-quality information that is both reliable and time-synchronized across the entire electrical infrastructure. Accurate and coherent measurements are crucial to ensure system observability, support decision-making processes, and maintain stability under variable and often unpredictable operating conditions.

In this framework, this chapter introduces the technological background of synchronized measurement architectures, presenting the main instruments, system configurations, and reference standards adopted in modern power systems. Particular attention is devoted to the infrastructures and devices that enable the acquisition and exchange of synchronized data, which together form the backbone of the digital monitoring chain.

The discussion also addresses the issue of Power Quality (PQ), whose analysis, traditionally limited to distribution networks, is gaining importance in transmission systems as well. The widespread use of non-linear and inverter-based generation technologies has introduced new forms of distortion and variability that must be properly monitored to preserve the quality and reliability of the

electrical service.

Finally, an overview of the main sources of uncertainty affecting the considered measurement instruments is provided, highlighting how each element of the measurement chain, from signal conditioning to data communication, contributes to the overall uncertainty and underlining the need for their proper characterization to ensure trustworthy and traceable measurement results.

1.1 Measurement, communication and synchronization architectures and protocols

In the context of synchronized measurements, two complementary paradigms have emerged as key enablers of the ongoing digital transformation of the electrical grid: the Wide Area Monitoring System (WAMS) and the IEC/IEEE 61850 standard. WAMSs are geographically extended monitoring infrastructures based on time-synchronized measurements provided by Phasor Measurement Units (PMUs) across the grid, whose data are aggregated and time-aligned by Phasor Data Concentrators (PDCs). Their communication and data exchange are regulated by the IEEE C37.118.2 [1] standard. At the substation level, the IEC/IEEE 61850 [2] standard suite represents a core component of the digitalization process, defining a unified framework for communication and data exchange between Merging Units (MUs) and Intelligent Electronic Devices (IEDs). Together, these technologies constitute the foundation of synchronized measurement and communication architectures, ensuring that measurement data are both temporally consistent and uniformly shared across heterogeneous monitoring devices.

1.1.1 Wide Area Monitoring Systems

WAMSs represent the most established implementation of distributed monitoring architectures in transmission networks. A WAMS collects time-synchronized measurements from geographically dispersed substations, ensuring coherent observation of the system state across the entire transmission network. This information allows the early detection of voltage instabilities, oscillations, and faults, facilitating preventive and corrective actions that improve grid stability and operational security. A typical WAMS architecture is composed of three hierarchical levels: field devices, data concentrators, and control centers. The field level includes PMUs, which estimate synchronized phasors, frequency, and Rate of Change of Frequency (ROCOF) from multiple locations in the grid. These data are collected and time-aligned by PDCs, which in turn transmit aggregated and validated information to a control center, typically a Supervisory

Control and Data Acquisition (SCADA) system, for real-time supervision and control of the electrical grid [3].

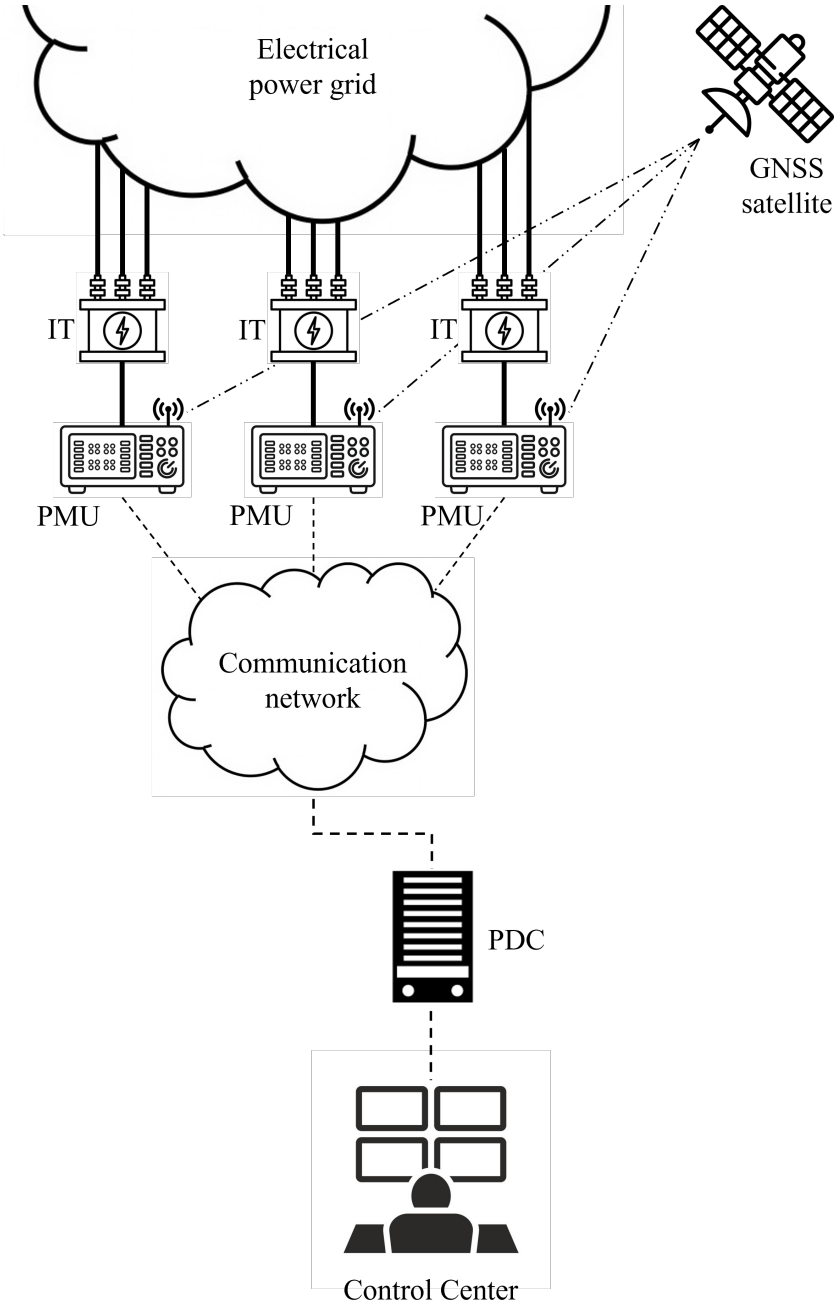

Figure 1.1: Schematic representation of a WAMS.

Phasor Measurement Units PMUs represent the fundamental sensing elements of a WAMS, providing time-synchronized measurements of voltage and current phasors, together with frequency and ROCOF. These quantities are accompanied by a time tag, known as a timestamp, which associates each measurement with an absolute temporal reference. This leads to the concept of the synchrophasor, namely the phasor representation of a voltage or current waveform referred to the instant of the Coordinated Universal Time (UTC) second. Given a sinusoidal signal $x(t)$, representing an ideal voltage or current waveform in the power system:

$$x(t) = X_m \cos\big(2\pi f(t - t_0) + \phi\big), \tag{1.1}$$

where X_m is the signal amplitude, f is the system frequency, and ϕ is the phase angle at the reference time t_0, the corresponding synchrophasor is defined by the IEC/IEEE 60255-118-1 standard [4] as the complex quantity:

$$\mathbf{X}(t) = X_{\text{rms}} e^{j\phi}, \tag{1.2}$$

where X_{rms} is the Root Mean Square (RMS) value of the signal within the considered observation window, and the phase-angle ϕ is referred to the absolute time provided by the UTC reference. By linking the phase information to a common time base, synchrophasors enable the coherent comparison of electrical quantities measured at different locations of the power grid. This capability is essential for the assessment of power system observability and for the development of time-coherent monitoring architectures.

Each PMU is composed of distinct functional blocks, which are further described, together with the possible sources of uncertainty they may introduce, in Section 1.3. The input signals are acquired through Instrument Transformers (ITs), which adapt voltage and current levels to the device's input range. The analog waveforms are then digitized and processed to estimate the corresponding synchrophasors, frequency, and ROCOF. The estimated quantities are encapsulated into data frames and transmitted through the IEEE C37.118.2 communication protocol [1], which ensures data interoperability among devices from different vendors.

Time synchronization represents a fundamental requirement for the correct operation of PMUs. It is typically achieved by disciplining the internal clock to an external UTC reference, provided either by an embedded Global Navigation Satellite System (GNSS) receiver or by network synchronization protocols such as the Precision Time Protocol (PTP). The synchronization accuracy directly affects the quality of the phase-angle estimation, and therefore the overall measurement uncertainty.

In the context of estimation algorithms, the IEC/IEEE 60255-118-1 standard

defines two compliance classes, namely Protection Class (P-class) and Measurement Class (M-class), which specify different requirements in terms of estimation accuracy, response time, and reporting latency under both steady-state and dynamic conditions. In general, P-class algorithms are optimized for fast-response measurements by employing shorter observation windows, allowing rapid tracking of signal variations and making these devices suitable for protection-oriented applications. Conversely, M-class algorithms use longer observation windows to achieve higher accuracy and improved rejection of noise and disturbances, which makes them preferable for monitoring and post-analysis purposes. The performance of PMUs is generally assessed through the Total Vector Error (TVE), which combines Magnitude Errors (MEs) and Phase-Angle Errors (PEs) into a single indicator. In both P- and M-class devices, the maximum admissible TVE under steady-state conditions must not exceed 1 %.

The synchrophasor data produced by PMUs are then collected, time-aligned, and managed by PDCs, which constitute the next layer of the WAMS infrastructure.

Phasor Data Concentrator PDCs are the components of the WAMS responsible for collecting, filtering, and time-aligning measurement data from PMUs. They can be implemented either as dedicated hardware devices or as software applications deployed on general-purpose servers, ensuring the proper aggregation and synchronization of synchrophasor data across the monitoring infrastructure. As defined in the IEEE C37.247-2019 standard [5], the PDC encompasses a set of functions that operate on synchrophasor data received from PMUs or other PDCs.

The synchrophasor infrastructure typically involves a hierarchical organization of PDCs. Local PDCs, generally installed within substations, aggregate data from a limited number of sources and forward it to regional or mid-level PDCs. These mid-level PDCs are responsible for aggregating streams from multiple substations and typically have greater computational resources to manage the increased volume and complexity of incoming data. At the top of the hierarchy, high-level PDCs perform data aggregation, storage, and real-time monitoring, often providing a system-wide view of the electric network. These PDCs may also handle data from interconnected networks, such as cross-border exchanges between Transmission System Operators (TSOs).

Beyond basic time alignment of synchrophasor data, a PDC shall also manage delayed or disordered data to maintain the latency requirements of the outgoing data stream. Several techniques have been proposed to address this, including the intelligent data forwarding strategies described in [6], which optimize the output flow based on dynamic policies. Examples of data management

policy include variable reporting rates or alternative sorting strategies based on packet arrival time rather than timestamps [7]. To ensure reliable operation, whether implemented on hardware or software, a PDC shall meet strict performance criteria. These include limits on processing latency, error limits in data conversion, and robustness under abnormal traffic conditions, such as duplicated packets or synchronization inconsistencies [5]. Some recent PDC implementations have introduced advanced techniques for efficient latency management [8] and adaptive data buffering [9], aimed at enhancing the responsiveness and reliability of synchrophasor-based applications. These solutions exemplify the adoption of edge computing paradigms, which enable low-latency processing and local decision-making directly at the data source.

The standard that regulates the exchange of information between devices measuring and/or transmitting synchrophasor data has recently been revised through the release of IEEE C37.118.2-2024 standard [1]. This marks the fourth major update to the standard, which originated in 1995 with the introduction of synchronous data communication for power systems. In 2011 [10], the communication protocol was decoupled from the measurement specifications and defined as a standalone standard. The new revision, released in 2024, introduces significant changes aimed at improving interoperability among devices, as well as enhancing their communication and control capabilities. While new functionalities have been introduced, backward compatibility with IEEE C37.118.2-2011 is preserved, ensuring that existing devices remain operational and interoperable [1]. One of the key additions in the update is support for discrete event data, a form of event-based communication that can be transmitted asynchronously within the periodic synchrophasor data stream. This functionality was leveraged in [11] to enable the PDC to propagate event/anomaly detections at higher levels in the monitoring hierarchy, supporting higher-level decision making.

Furthermore, the new standard supports the evolution of the PMU from a passive device to an active component within control architectures. In fact, the update introduces new command types that upper levels of the synchrophasor infrastructure can communicate [1]. These include commands for retrieving historical data stored locally on the PMU and for configuring the device dynamically. While the importance of communication security is acknowledged in the updated standard, a formal specification of security mechanisms remains an open issue.

1.1.2 IEC/IEEE 61850: digitalization of electrical substations

Within WAMSs, a central role is played by the PMUs, which interface directly with the power grid. However, the ongoing evolution of the electrical system is driving a parallel transformation at the substation level, where digitalization is leading to the progressive integration or replacement of conventional equipment with MUs. These devices acquire voltage and current signals from instrument transformers and transmit the corresponding Sampled Values (SVs) at high reporting rates, enabling advanced processing by downstream IEDs. This transition has been enabled by the IEC/IEEE 61850 family of standards, which defines a unified model for communication and interoperability in substation automation systems. Analog connections are replaced by Ethernet-based process buses carrying digital data streams generated by MUs or Stand-Alone Merging Units (SAMUs). This approach reduces copper wiring, improves signal integrity, and allows protection, control, and monitoring functions to coexist within a single digital platform.

MUs convert voltage and current waveforms into SVs in compliance with the IEC 61850-9-2 standard [12]. The UCA 61850-9-2LE specification [13], a widely adopted de facto standard, defines interoperability guidelines and two typical sampling rates, 80 and 256 samples per cycle. The SVs may be directly transmitted to local or remote aggregators, or processed by IEDs implementing PMU, Power Quality Meter (PQM) or Digital Fault Recorder (DFR) functionalities [14], [15]. The protocol also includes the SmpCnt field, which sequentially indexes each packet, enabling straightforward detection of missing samples before detailed analysis [16].

In this context, the term MU generally refers to any device responsible for acquiring analog voltage and current signals and converting them into digital SVs. This definition also encompasses SAMUs, which are stand-alone units designed to interface conventional transformers, typically lacking digital outputs, with IEDs capable of processing SVs. Likewise, it includes MUs integrated directly into modern digital instrument transformers equipped with native digital outputs. IEDs can operate at high sampling rates, capturing transient phenomena and recording thousands of samples per second. When equipped with event detection functionalities, as in the case of DFRs [17], they do not transmit SVs directly but instead use protocols such as Manufacturing Message Specification (MMS) and Generic Object Oriented Substation Event (GOOSE), defined in the IEC 61850 standards, to communicate measurement data and detected events to other substation devices.

Both MUs and IEDs verify stream integrity and detect inconsistencies caused

by missing or invalid packets, as well as loss of synchronization. However, they do not assess the actual information conveyed by the digital data. Nowadays, commercial MUs acquire, digitize, and transmit samples in compliance with the reference standards. Recent developments have introduced enhanced features, such as precise time synchronization management even with low-cost hardware [18], and tools supporting complex Hardware-in-the-Loop (HiL) simulations [19]. Nonetheless, fast analysis of the acquired samples aimed at identifying anomalies or events has not yet been implemented in MUs.

1.1.3 Synchronization protocols in power systems

Accurate time synchronization is a fundamental requirement for the operation of distributed monitoring networks in power systems, ensuring the temporal alignment of data collected from different points of the grid. Such alignment is essential for coherent measurement comparison and for advanced applications like state estimation, fault localization, and stability assessment. Traditional synchronization relies on GNSS technologies, such as the Global Positioning System (GPS), which provide an absolute reference to UTC. Although widely used, satellite-based solutions may suffer from signal loss or interference, especially at the individual device level, thus motivating the adoption of complementary timing mechanisms. Alternative solutions employ time distribution protocols implemented over physical infrastructures, including Inter-Range Instrumentation Group Timecodes (IRIG) timecodes and packet-based methods such as the IEEE 1588 PTP. Compared with GNSS-based synchronization, these approaches offer the advantage of disseminating timing information across local or wide area networks, allowing multiple devices to share a common reference without each requiring a dedicated satellite receiver. This not only improves robustness against interference or signal unavailability but also facilitates scalable synchronization within digital substations and interconnected monitoring infrastructures. In this scenario, recently increasing attention has been devoted to the White Rabbit (WR) technology, an extension of PTP that enables subnanosecond synchronization accuracy [20].

The PTP protocol, one of the most widely adopted nowadays, defines specific profiles to ensure compatibility among hardware from different manufacturers. These profiles not only guarantee time accuracy within defined limits but also enable continuous monitoring and maintenance of synchronization performance, thus enhancing system resilience. Each profile specifies a set of optional features and parameter values designed to ensure interoperability across devices from multiple vendors while maintaining the required precision and performance. The IEC 61850-5 standard [21] defines the time accuracy require-

ments for event time tagging and synchronized measurements, summarized into five performance classes, from T1 to T5, covering accuracy levels from 1 ms to 1 μs. To meet the requirements of class T5, the IEC/IEEE 61850-9-3 profile [22], also known as the PTP Power Utility Profile (PUP), was developed to enable accurate and resilient distribution of time information within the electrical network. The specifications of the profile encompass technical, configuration, and hierarchical aspects. Technically, it operates at Level 2 of the Open Systems Interconnection (OSI) stack, ensuring precise and deterministic communication. The configuration parameters allow each device to be uniquely set up by defining fixed transmission intervals and enabling delay-measurement mechanisms in boundary and transparent clocks. In addition, a system of priority codes determines the role of each device within the synchronization chain, establishing a clear hierarchy that supports stable and reliable time distribution.

Despite its effectiveness, the PTP-PUP still shows limitations when higher accuracy or robustness is required, especially in critical power system applications. To fill this gap, the WR protocol represents a highly promising solution, whose potential in synchronized power system measurements will be explored in Chapter 4.

Finally, it is worth noting that cybersecurity aspects concerning availability and integrity are crucial for packet-based synchronization protocols. The topic is actively discussed within the scientific and standardization community, as reflected in Annex P of IEC/IEEE 61588-2021 standard [23] and in the multi-layered approach to synchronization security. It is clear that maliciously introduced delays and corrupted packets can jeopardize monitoring activities, but this happens also in other time- and latency-sensitive WAMS applications [24]. A detailed analysis of security aspects is beyond the scope of this thesis, as they concern all packet-based communications within and beyond substations. In this context, WR once again proves advantageous, as its reliance on a dedicated infrastructure such as Sync Ethernet (SyncE) shifts the security perimeter to a more controlled environment compared to conventional PTP, while confidentiality remains generally non-critical for synchronization.

1.2 Power Quality monitoring

According to the IEEE 1159-2019 standard [25], PQ is defined as the wide variety of electromagnetic phenomena that characterize the voltage and current at a given instant in a specific point of the power system. Monitoring these phenomena plays a fundamental role in assessing the capability of the network to supply energy within acceptable quality limits. Poor PQ can compromise the correct operation of electrical equipment, reduce component lifetime, and

introduce additional losses. Conversely, the capability to quantify and trace PQ disturbances enables system operators to identify malfunctioning components, detect the origin of faults, and plan effective mitigation strategies. For this reason, the development of accurate PQ measurement and analysis tools has become an integral part of modern monitoring infrastructures.

In modern power systems, the continuous assessment of PQ represents a key element for ensuring the reliability and efficiency of electricity supply. Traditionally, PQ monitoring has been primarily associated with distribution networks, where the impact of non-linear loads and distributed generation most evidently manifests through distortions, voltage fluctuations, and other disturbances affecting end users. However, the power grid evolution, driven by the increasing penetration of distributed generation sources, has extended the relevance of PQ issues to transmission systems as well, where they can influence the stability and performance of protection, control, and monitoring functions.

1.2.1 Power Quality disturbances

As defined in IEC 61000-2-5:2017 [26], electromagnetic phenomena are classified into several groups according to their origin and nature. This classification provides a general overview of electromagnetic disturbances, not limited to power systems, by distinguishing between conducted and radiated phenomena, and between low-frequency and high-frequency ranges. Among these, conducted low-frequency phenomena represent the main PQ disturbances encountered in electrical systems, including transients, amplitude variations, and frequency variations. For reference, it is worth noting that, in [25], the terms high frequency and low frequency are not associated with specific frequency ranges but rather indicate relative differences in the predominant spectral content of the phenomena within each category.

Figure 1.2 illustrates some of the main PQ disturbances that can affect power systems [27]. These phenomena can be grouped according to the quantity they influence, such as voltage magnitude, waveform shape, frequency, or phase balance, and according to their duration. Most of the categorized phenomena refer to voltage signals, as they directly determine the quality of supply. However, monitoring current quality is also essential, since current disturbances can affect voltage quality and potentially cause damage to connected loads.

Among the events affecting voltage magnitude, interruptions, sags, and swells represent some of the most critical ones. Interruptions occur when the supply voltage drops below 10 % of its nominal value and can be instantaneous, short, or long depending on duration. Voltage sags are defined as temporary reductions of the RMS voltage to values between 10 % and 90 % of the nominal,

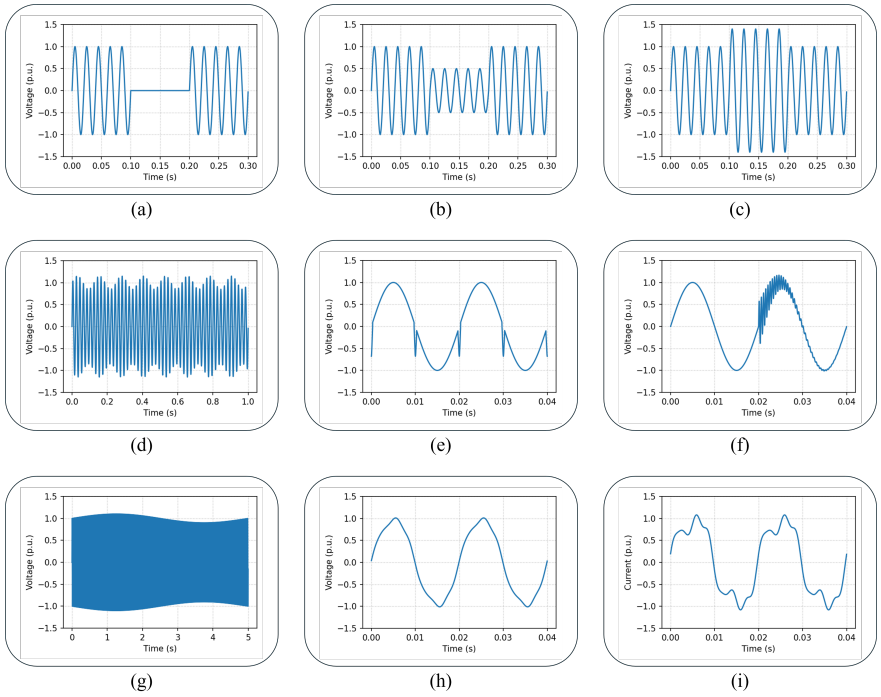

Figure 1.2: Examples of typical PQ disturbances affecting voltage and current waveforms, including interruptions (a), sags (b), swells (c), flickers (d), notches (e), transients (f), slow RMS modulations (g), and harmonics (h) and (i).

typically lasting from half a cycle to one minute. They are usually caused by faults, motor starts, or large load variations. Conversely, voltage swells consist of RMS increases above 110 % of the nominal value and are often induced by single-phase-to-ground faults or by the disconnection of large inductive loads.

Other disturbances arise from the lack of symmetry in three-phase systems: in ideal balanced conditions, only positive-sequence components are present; however, asymmetrical loads or line impedances generate negative- and zero-sequence components that can reduce the efficiency of rotating machines and increase the heating of conductors. The voltage unbalance factor, expressed as the ratio between the negative- and positive-sequence components, is the most common index to quantify this condition and should remain below $2 - 3\,\%$ in transmission networks [28].

Waveform distortions primarily affect current signals, since they originate from the non-linear behavior of many electronic and power conversion devices. These distorted currents interact with the system impedance, producing voltage distortions that can propagate through the network. Consequently, although both voltage and current waveforms can exhibit distortion, the current harmonics generated by non-linear loads are typically the root cause of most waveform

distortions observed in power systems. These distortions can be represented as the superposition of harmonic and interharmonic components on the fundamental waveform.

The Total Harmonic Distortion (THD) is the most widely used index to quantify the overall contribution of harmonics, defined as:

$$\mathrm{THD}[\%] = 100 \times \frac{\sqrt{\sum_{k=2}^{\infty} I_k^2}}{I_1} \tag{1.3}$$

where I_k is the RMS value of the k-th harmonic and I_1 is that of the fundamental component. A low THD indicates a waveform close to the ideal sinusoid, while high values denote strong distortion and potential malfunctioning of equipment. Besides harmonics, some converters can introduce repetitive narrow notches in the voltage waveform, known as notching, which combine the characteristics of a periodic disturbance and a high-frequency transient, and can interfere with frequency estimation algorithms based on zero-crossing detection.

Further degradation of waveform quality can be caused by the presence of a Direct Current (DC) component, often introduced by rectifier stages or asymmetries in converter switching, and by voltage fluctuations, which appear as slow modulations of the voltage envelope. The latter can generate visible flicker in lighting systems and are commonly associated with arc furnaces or rapidly varying industrial loads.

Finally, frequency variations constitute another important category of PQ phenomena. They result from imbalances between the total generated and consumed power and are particularly relevant in systems with a high penetration of renewable sources, where inertia is reduced. Although typically limited to few tenths of hertz around the nominal frequency, such variations can affect the synchronization of protection and control devices, especially when occurring simultaneously with other disturbances.

From a measurement perspective, the characterization of these phenomena relies on indices that quantify their amplitude, duration, frequency content, or rate of occurrence. These indices constitute the basis of standardized assessment procedures and are essential to ensure comparability among measurement sites and instruments. Their accurate computation requires sufficient temporal resolution and precise time synchronization, which in turn depend on the performance of the measurement devices and the associated timing systems. The most commonly used instruments for monitoring PQ phenomena are the PQMs, which, when installed at different points in the network, can collectively provide important information for grid management [29].

1.2.2 Power Quality Meters

The IEEE 1159-2019 standard [25] defines a PQM as an instrument intended to measure, record, and analyze the parameters associated with PQ phenomena in electrical systems. Instruments used for this purpose can range from simple analog voltmeters to complex, permanently installed multi-site monitoring systems. The selection of a suitable device depends on the monitoring objectives and on the type of disturbances to be detected, as each instrument presents specific capabilities and limitations in terms of response to system variations and measurement accuracy. In practice, terms such as PQ analyzer, power disturbance analyzer, PQ meter, PQ monitor, and revenue meter with PQ function are often used interchangeably to describe instruments that perform this role.

The PQM is a hybrid instrument designed to monitor and analyze both steady-state and transient PQ phenomena. It continuously evaluates standard PQ indices, such as RMS voltage, THD, and flicker, while also detecting short-duration events including voltage dips and swells. This dual capability enables a comprehensive assessment of the electrical supply quality, combining long-term statistical evaluation with the detection of fast disturbances. PQM performance is defined by IEC 61000-4-30 [30], which establishes two main classes for PQ measurement instruments. Class A devices ensure high accuracy, precise synchronization, and full traceability, making them suitable for compliance verification and reference measurements. Class S devices, instead, are intended for general monitoring and comparative assessments, offering simplified requirements and lower implementation costs. Depending on the configuration, the PQM can record and store event-related data in dedicated files compliant with the Power Quality Data Interchange Format (PQDIF) format [31], which can be transmitted to a data concentrator or locally stored for subsequent retrieval. Its programmable nature allows the device to adapt its monitoring logic to different objectives and grid locations, making it suitable for both local and distributed measurement systems.

The integration of PQMs within WAMS represents an important step toward a more comprehensive and multi-layered monitoring of transmission systems. While PMUs provide time-synchronized measurements of voltage and current phasors, enabling real-time situational awareness and dynamic analysis, PQMs complement these functions by offering continuous assessment of power quality indices and detection of short-duration disturbances. The approach proposed in [32] extends this concept by integrating heterogeneous measurement data within a unified architecture. Alongside PMUs and PQMs, the system also incorporates DFRs, which record high-frequency voltage and current waveforms during faults or switching events, capturing pre-, during-, and post-fault infor-

mation as well as binary data such as breaker statuses. Through a dedicated system integrator, the proposed platform correlates synchrophasor time series with PQM and DFR event records, using geographical and temporal alignment to merge data characterized by different accuracies, sampling rates, and formats. This heterogeneous integration enhances grid observability and supports advanced post-event analyses, facilitating the identification of disturbance origins and improving the reliability and situational awareness of the monitoring infrastructure. Such an approach also aligns with the growing trend of embedding PQ detection capabilities into instruments not originally designed for this purpose, as will be further illustrated in Chapter 2 through the case of MUs.

1.3 Sources of uncertainty in synchronized power system measurements

The accuracy of electrical measurements depends on a complex interplay of factors related to both the measurement devices and the surrounding environmental conditions. Both in controlled environments, such as laboratory setups, during calibration or testing activities, and in field operation, multiple sources of uncertainty contribute to the discrepancy between the estimated and the true value of the measurand. Moreover, when dealing with synchronized instruments such as PMUs or MUs, which represent the core focus of this thesis, time synchronization and management play a leading role in determining the overall uncertainty. Understanding and quantifying these contributions is essential to ensure data reliability, enable proper uncertainty propagation, and establish the metrological traceability of power system measurements.

1.3.1 Architecture-related sources of uncertainty

Figure 1.3 shows the typical architecture of a synchronized measurement device, such as a PMU or a PQM, and schematizes the main functional blocks. Each of them represents a potential source of errors, therefore contributing to the overall uncertainty on the final estimates.

Signal conditioning module The measurement process begins with the analog signal conditioning stage, which interfaces the electrical quantities, previously transduced into lower-voltage or lower-current waveforms by devices such as ITs, with the electronic circuitry of the device. This module, which is part of the instrument's Data Acquisition (DAQ) system, adapts the voltage and current signals to the input range of the Analog-to-Digital Converter (ADC), ensuring proper scaling and galvanic isolation from the transducer output. In

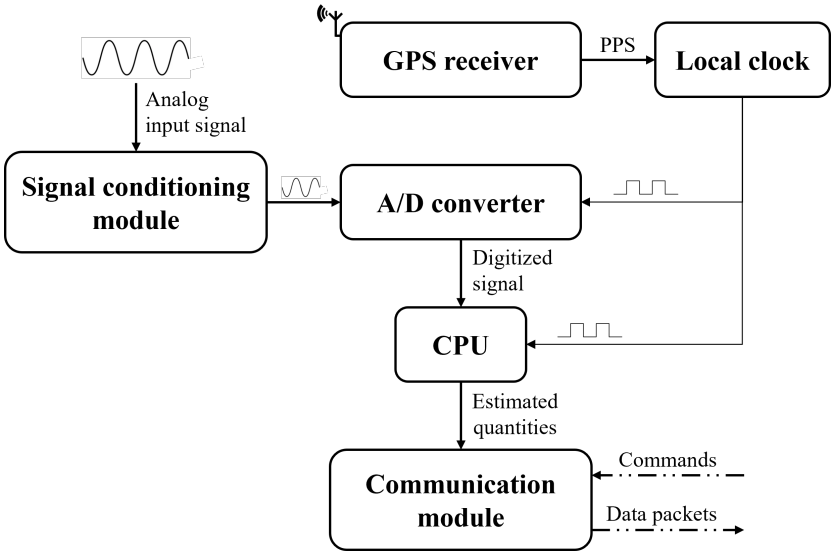

Figure 1.3: Architecture of a synchronized measurement instrument for power systems.

addition, the conditioning stage generally includes filtering operations aimed at limiting noise and unwanted spectral components, thereby isolating the relevant information contained in the waveforms to be digitized. Since analog circuitry is inherently more sensitive to temperature variations and electromagnetic interference than digital components, this stage represents one of the main contributors to the overall measurement uncertainty, particularly in field applications.

Analog-to-Digital converter The ADC constitutes the second element of the DAQ system and is responsible for producing the discrete representation of the conditioned signal. It can introduce uncertainty due to several factors, primarily related to sampling, quantization, and converter linearity. The converter must operate within its specified input range to avoid saturation or clipping, which would irreversibly distort the waveform and compromise the accuracy of the estimations. Furthermore, any deviation from ideal linearity in the transfer characteristic may introduce errors that propagate through the measurement chain. Even under proper sampling conditions, quantization introduces an unavoidable error that depends on the converter resolution, manifesting as additive noise in the digitized signal. Another critical aspect is the accuracy and stability of the sampling clock: phase noise and jitter translate into PEs in the reconstructed waveform, which are particularly detrimental in synchronized measurements such as those performed by PMUs. In these cases, even small temporal deviations can produce significant phase uncertainties, directly impacting the estimation of synchrophasors, frequency, and ROCOF.

Time synchronization Time synchronization is ensured through the combined operation of the GPS receiver and the local oscillator. Regarding the synchronization source, GPS technology is not the only option available; it can be replaced by other approaches, either through synchronization signals as Pulse per Second (PPS) or IRIG-B, or packet-based protocols such as the PTP, configured according to the appropriate Power or Utility Profile. The synchronization source provides the reference to UTC, while the local clock disciplines the acquisition process and allows the Central Processing Units (CPUs) to perform accurate timestamping of the acquired data. The long-term stability of the local oscillator, affected by drift and temperature, defines the device's timing performance between synchronization updates, which typically occur once per second. Given the critical role of timing accuracy in synchronized measurements, continuously monitoring the synchronization status is essential to detect degradation, prevent data misalignment, and ensure the reliability of time-tagged measurement streams.

CPU and estimation algorithms The CPU governs the acquisition process and executes the estimation algorithms. At this stage, the uncertainty introduced is entirely software-related and depends on the specific algorithm implemented. The case of phasor estimation in PMUs is particularly illustrative. In this process, algorithms extract magnitude, phase angle, frequency, and ROCOF, assuming quasi-sinusoidal conditions over the observation window. Different estimation methods and parameter choices such as window length, spectral model, or noise treatment can lead to variations in accuracy, especially under dynamic or distorted conditions. Arithmetic precision, numerical rounding, and timing synchronization within the processing routine also contribute to the overall uncertainty, although their impact is typically negligible compared to other sources.

Communication module Once the estimation process has been completed and the measurements have been time-tagged, the data are transmitted through the communication module to higher levels of the monitoring hierarchy, such as PDCs. Although this stage does not alter the value of the measured quantities, it influences data completeness and timeliness. Packet loss, transmission delays, or desynchronization between data streams can compromise the effective usability of the measurements for real-time applications. Moreover, communication infrastructures are increasingly exposed to cybersecurity threats, such as data manipulation or denial-of-service attacks, which may affect the availability or integrity of measurement data. These aspects, although highly relevant for the reliability of modern monitoring infrastructures, fall outside the scope of this

thesis.

1.3.2 Environmental and operational factors

Across all stages, environmental conditions affect component behavior and, consequently, the measurement accuracy. Variations in temperature may alter analog gain, offset, and impedance, modify filter responses, or affect the stability of reference voltages and clock frequencies, thereby changing the overall uncertainty. In addition, mechanical stress, humidity, and electromagnetic interference can further influence the performance of both analog and digital circuitry, especially in outdoor or industrial environments where measurement devices are often exposed to harsh operating conditions. The combined effects of temperature fluctuations and electronic drifts define the long-term stability and reliability of the instrument. Consequently, international standards provide explicit guidelines on the environmental conditions to be maintained during measurement and testing procedures.

1.3.3 Summary and device performance evaluation

Ultimately, all modules of a synchronized measurement device, whether a MU, a PQM, or a PMU, contribute to the overall uncertainty. Quantifying their combined effect is challenging because the contributions are not strictly independent and may vary with operating conditions. For this reason, international standards define synthetic performance indices that provide a meaningful yet compact characterization of accuracy. Once again, the case of synchrophasor measurements is particularly illustrative: the most widely adopted performance index is the TVE, which combines MEs, PEs, and synchronization errors into a single metric. Nevertheless, the separation of these contributions remains essential for understanding the physical origin of measurement uncertainty and for improving the reliability and interpretability of synchronized data in power system monitoring.

Chapter 2

Time series analysis of synchronized measurements in power systems

The evolving power grid, characterized by the increasing occurrence of Power Quality (PQ) events and network anomalies, calls for the adoption of advanced event detection and identification methods. These must be applied to the analysis of measurement data streams produced by devices distributed across monitoring infrastructures, in order to ensure the timely identification, accurate classification, and effective communication of anomalous conditions within the monitoring hierarchy. In this perspective, event detection is not merely aimed at identifying disturbances, but constitutes a key mechanism for preserving data trustworthiness. By recognizing and qualifying anomalous phenomena, it enables the filtering or contextualization of affected measurements, thus supporting an accurate assessment of the reliability and quality of synchronized data streams.

Within this context, various strategies have been proposed for event detection. After outlining the most relevant ones, this chapter explores the application and adaptation of the Matrix Profile (MP) to the power systems domain and to different types of electrical measurements. Introduced in 2016 [33], the MP is a domain-independent and exact technique [34] originally developed for time series analysis and conceived for the post-mortem exploration of long datasets. Owing to its versatility, the MP has been also successfully applied outside of power systems, in the field of biomedical signal processing, specifically Photoplethysmography (PPG) analysis, where its capability to reveal recurring patterns has proven particularly effective [35].

The approach proposed in this work extends its applicability by reformulating it for the processing of short and real-time time series, enabling prompt and reliable detection of events directly at the measurement edge. This shift transforms a powerful offline analytical tool into a practical framework for operational awareness in modern monitoring architectures.

The first part of the discussion focuses on Sampled Values (SVs) streams generated by Merging Units (MUs) or Stand-Alone Merging Units (SAMUs), building upon the methodologies and results first presented in [36] and further characterized in [37], where the MP was demonstrated to be an effective tool for real-time event detection in digital substation environments. The second part shows how the MP can be extended to the analysis of synchrophasor data in Phasor Measurement Unit (PMU)–Phasor Data Concentrator (PDC) architectures, following the approach introduced in [11], and how it can support both local and hierarchical event analysis within Wide Area Monitoring Systems (WAMSs).

2.1 Event detection approaches in power system data streams

As discussed in Section 1.2, several types of events can affect power systems, causing a degradation of the quality of the energy provided. Some are related to ordinary grid operations (e.g., breaker tripping), others to external causes such as lightning or adverse weather. Waveform recording during anomalous events is important to allow post-mortem analysis: for instance, analysis of stored waveforms allows similar events to be correlated, helping to identify their sources [38], [39].

Among PQ events, voltage dips and swells are particularly relevant, as they can result from both operational maneuvers and disturbances. Traditional methods aim to detect this kind of events using threshold-based approaches that rely on Root Mean Square (RMS) estimates within the considered observation window. The method proposed in [29] adopts an RMS-based approach for locating the source of voltage dips, thus enabling the use of conventional PQ measurements without the need for synchronized waveform acquisition. Building upon the studies in [40], [41], where RMS variation and phase displacement were identified as effective indicators for distinguishing between upstream and downstream events, the work in [29] extends this framework to real-field multi-level networks, improving event aggregation and classification robustness under practical operating conditions. However, such approaches are more likely to fail in more complex scenarios, for instance, when multiple events overlap (e.g., a dip occurring during a fluctuation), making it difficult to distinguish between them

and accurately identify the voltage dip. Such accurate discrimination is crucial, as it enhances the reliability and stability of power system operation by allowing operators to understand the causes of these events and take appropriate actions to mitigate future occurrences [32], [42].

To address these limitations, recent research has increasingly focused on more advanced techniques for the identification and classification of events in power signals. Broadly, these techniques can be divided into two categories: signal processing approaches and data-driven methods based on Machine Learning (ML). Signal processing methods remain a solid reference in the literature, typically relying on threshold-based or statistical analyses [43], as well as time–frequency techniques such as Wavelet Transform [44] and Hilbert–Huang Transform [45]. These approaches are well suited for capturing localized disturbances in both time and frequency, but may struggle when dealing with the nonlinearities and variability of modern power systems.

To overcome these challenges, data-driven solutions based on ML have gained increasing attention. They mainly target event classification tasks and commonly employ Convolutional Neural Networks (CNNs) optimized for the automatic recognition of PQ disturbances. However, their effectiveness is strongly dependent on the availability and quality of labeled datasets, as well as on the computational resources required for training and deployment. To mitigate these limitations, lightweight architectures such as Dynamic Pocket Networks [46] have been proposed, enabling efficient event classification with reduced computational burden. Despite these advantages, ML techniques also present critical drawbacks: they typically require large and well-curated labeled datasets, may exhibit poor generalization when exposed to unseen operating conditions, and often behave as black-box models, limiting interpretability and trust in operational environments.

In this context, alternative approaches based on time series analysis, such as the MP, have recently proven effective for event detection in power data streams due to their versatility and ease of application [33]. Unlike ML-based methods, the MP does not require training or large labeled datasets, making it particularly suitable in scenarios where event signatures are unknown or difficult to model in advance. In fact, the great strength of MP lies in the fact that it is essentially parameter-free, eliminating the need for learning or validation phases. While its computational cost can increase with longer time series, potentially challenging real-time deployment, this limitation can be mitigated through efficient implementations, as the STOMP incremental update [34] and the Mueen's Algorithm for Similarity Search (MASS) [47].

Despite its inherently general-purpose design and its successful application across a wide range of domains [33], the MP was first introduced to power system

measurements in [48], where it was employed to detect and label different types of tripping events by analyzing time series derived from PMU data streams. In the following sections, the applicability of the MP is explored on different types of measurement data. It is first thoroughly investigated for event detection on SV data streams, with a detailed characterization across subsequence lengths, noise levels, and PQ phenomena [36], [37]. Subsequently, its use is extended to PDC-level detection and event correlation across multiple PMU data streams, leveraging a layered approach that combines preliminary anomaly highlighting with MP-based similarity analysis [11].

2.2 The Matrix Profile technique

The MP is a time-series analysis technique based on the computation of the Euclidean distance between subsequences of a signal. It provides a unified framework for both anomaly detection and motif discovery. In the context of time-series analysis, the notions of *anomaly* and *motif* are here introduced qualitatively: an anomaly refers to a portion of the sequence that differs, to some extent, from all other portions of the same sequence, whereas a motif is a pattern that recurs, more or less faithfully, within the sequence. It is important to note that a motif may occur sporadically and does not imply periodicity. Periodic behavior, on the other hand, can be analyzed through an intermediate step of the MP algorithm known as the Distance Profile (DP). A way to formalize both anomaly and motif definitions is through the computation of Euclidean distances between subsequences, which constitutes the core of the MP methodology. This section presents the mathematical formulation of the MP algorithm together with its intermediate step, the DP.

2.2.1 Matrix Profile

Consider a generic time series T defined as:

$$T = [t_0, t_1, \ldots, t_i, \ldots, t_{n-1}] \tag{2.1}$$

The computation of the MP requires selecting a subsequence length, denoted by the integer m. The choice of m is not unique and should be made according to the characteristics of the time series under analysis. Indeed, different values of the subsequence length will lead to different MP outputs, emphasizing more or less clearly the presence of anomalies or motifs. Each subsequence S_i of T is:

$$S_i = [t_i, t_{i+1}, \ldots, t_{i+m-1}] \quad \text{for } i = 0, 1, \ldots, n-m \tag{2.2}$$

The comparison between subsequences should be based solely on their shape rather than on absolute levels or scaling factors, allowing the algorithm to detect patterns that are structurally similar even if they differ in offset or magnitude. For this reason, in the MP, each subsequence is z-normalized to remove the influence of shifts in the mean value and variations in amplitude:

$$Z_i[k] = \frac{S_i[k] - \mu_i}{\sigma_i} \text{ for } k = 0, \ldots, m-1 \tag{2.3}$$

where k indexes the elements of the subsequence, and μ_i and σ_i denote the mean and standard deviation of S_i, respectively. The Euclidean distance between the subsequence Z_i and Z_j is:

$$D(Z_i, Z_j) = \sqrt{\sum_{k=0}^{m-1} \big(Z_i[k] - Z_j[k]\big)^2} \tag{2.4}$$

This step ultimately determines the computational complexity of the MP. A naive implementation requires $\mathcal{O}(n^2 m)$ operations, making it impractical for large datasets. Algorithms such as Scalable Time series Anytime Matrix Profile (STAMP) reduce this to $\mathcal{O}(n^2 \log n)$ through the use of Fast Fourier Transform (FFT), while Scalable Time series Ordered-search Matrix Profile (STOMP) further lowers the complexity to $\mathcal{O}(n^2)$ by incrementally updating the dot product between adjacent subsequences, effectively removing the dependence on the subsequence length m [34].

The application of Equation 2.4 yields the matrix M, whose elements contain the distances between each subsequence and all the other subsequences of the same length:

$$M = \begin{bmatrix} D(Z_0, Z_0) & \ldots & D(Z_j, Z_0) & \ldots & D(Z_{n-m}, Z_0) \\ \vdots & & \vdots & & \vdots \\ D(Z_0, Z_i) & \ldots & D(Z_j, Z_i) & \ldots & D(Z_{n-m}, Z_i) \\ \vdots & & \vdots & & \vdots \\ D(Z_0, Z_{n-m}) & \ldots & D(Z_j, Z_{n-m}) & \ldots & D(Z_{n-m}, Z_{n-m}) \end{bmatrix} \tag{2.5}$$

The "profile" of the matrix M, from which the technique derives its name, is obtained by computing the minimum value of each row of the matrix:

$$\text{MP}[i] = \min_{j \neq i} D(Z_i, Z_j) \tag{2.6}$$

From Equation 2.6, it follows that the MP quantifies the minimum distance between each subsequence of a time series and its closest matching neighbor, thereby providing a detailed characterization of the signal in terms of similar-

ity. Based on this representation, previously defined discords and motifs can be identified as the subsequences associated with the maximum and minimum values of the MP, respectively, as formalized in Equations 2.7 and 2.8.

$$discord = \arg\max_i \mathrm{MP}[i] \tag{2.7}$$

$$motif = \arg\min_i \mathrm{MP}[i] \tag{2.8}$$

A closer look at the technique reveals another interesting feature: the possibility of analyzing periodic signals. This is made possible through the DP, an intermediate step of the MP.

2.2.2 Distance Profile

To understand the mechanism of the DP, it is necessary to take a step back and focus on the meaning of the rows of the matrix M, defined in Equation 2.5. Each row (and column) of M corresponds to one instance of the DP and represents the outcome of the MP's key step, namely the Euclidean distance computation. The elements of each DP vector represent the distance of the Z_j argument in Equation 2.4 (hereafter referred to as the base subsequence Z_b) from all other subsequences of the same length.

Let Z_b denote the base subsequence, defined as

$$Z_b = [t_b, t_{b+1}, \ldots, t_{b+m-1}] \tag{2.9}$$

where b is the starting index of the subsequence. The DP associated with Z_b contains the distances between Z_b and all other subsequences of the same length:

$$\mathrm{DP}_b[i] = D(Z_i, Z_b), \qquad i = 0, 1, \ldots, n - m \tag{2.10}$$

In the presence of a periodic or quasi-periodic time series, local minima appear in the DP at positions corresponding to the best matches of Z_b, following the characteristic periodicity of the signal. Let $\widehat{P}_k$ denote the distance in samples between the k-th and $(k+1)$-th minima of the DP. Each $\widehat{P}_k$ provides an estimate of the period in samples, which can be converted into time through

$$\widehat{T}_k = \widehat{P}_k \, \Delta t \tag{2.11}$$

where Δt is the sampling interval, and $\widehat{T}_k$ is the corresponding period expressed in time units. Different choices of Z_b generate time-shifted DPs, but they do not overturn the period estimation, since Z_b still recurs within the time series with the same cadence.

Once the period has been estimated, the fundamental frequency can be di-

rectly obtained as its reciprocal. This makes it possible to perform multiple analyses on the time series within a single, unified MP-based framework, enabling frequency estimation and anomaly/motif detection to be carried out jointly.

2.3 Matrix Profile for event detection in Sampled Value streams

In this section, the application of the MP to the analysis of SVs provided by MUs is presented. This discussion builds upon the work in [37], where the use of the MP was in-depth investigated for the analysis of SV streams, as a technical extension of [36]. The central part of the investigation concerns the characterization of the MP technique under various configurations and operating conditions, aimed at investigating the feasibility of enhancing the functionality of next-generation MUs. The analysis considered different subsequence lengths in the MP, noise levels, and signals affected by PQ phenomena. The performance of the technique was evaluated through two indicators: the accuracy in estimating the temporal position of events and the computational time. Furthermore, the MP was compared with similar approaches, demonstrating its high robustness to noise and overlapping PQ phenomena, as well as its greater ease of implementation compared to other methods. Finally, the discussion is completed with the application of the proposed technique to real-world case studies, which validate its effectiveness under practical operating conditions.

2.3.1 Method characterization

The characterization of the MP performance in terms of anomaly and event detection and localization accuracy is presented through a sensitivity analysis aimed at evaluating how parameter settings and operating conditions influence the method's robustness and accuracy. The analysis is carried out on simulated sample sequences representing plausible data streams of a MU, each consisting of a 1 s recording of single-tone sinusoidal signals. It is worth noting that the MP method treats each SV stream, corresponding to a single phase, as an independent time series, and therefore does not account for polyphase events. Since time-series analysis is independent of the signal type, generic voltage or current signals are considered.

The nominal system frequency is set to 50 Hz and the sampling rate to 4000 Hz, resulting in 80 samples per cycle, as specified in [13]. This configuration provides a time resolution of 250 µs. To approximate realistic operating conditions in actual power networks, the signal frequency is set to 50.05 Hz, a

value adopted in several functional tests of IEC 62586-2:2017 [49]. This deviation of a few tens of mHz ensures an off-nominal condition, resulting in non-synchronous sampling process. The signal amplitude is set to 10 a.u. (arbitrary units), while the initial phase is set to 0 rad. To simulate distortions introduced by the acquisition stage, uncorrelated white Gaussian noise is superimposed on the simulated sample sequences, resulting in an overall Signal-to-Noise Ratio (SNR) of 80 dB.

The test signal includes a PQ event located at the center of the 1 s observation window, corresponding to sample index 2000. The anomaly consists of a magnitude swell with an amplitude of 5 a.u. and a duration of 5 ms (20 samples). Such an event would be difficult to detect using standard Power Quality Meters (PQMs), mainly due to its short duration of 5 ms, which is significantly lower than the typical time resolution of half a cycle. Moreover, the non-synchronous sampling process caused by the off-nominal condition would lead to inconsistent and oscillating results in the RMS computation performed by the PQM.

In the following, the effectiveness of the MP in detecting the described PQ event is demonstrated under different disturbance conditions. The MP was computed considering four different subsequence lengths: 80, 160, 320, and 640 samples (corresponding to 1, 2, 4, and 8 nominal cycles, respectively). For each scenario, 100 independent tests were performed, with randomly generated additive noise, to ensure statistical validation of the results. The mean value represents the expected performance, while the associated uncertainty combines the 95^{th} percentile of the results with a systematic contribution accounting for the temporal resolution of the method, estimated as half the subsequence length. The MP performance was evaluated through two indices: estimation accuracy and computation time. The former represents the time difference between the estimated and actual starting instants of the swell. The estimated instant is determined as the position corresponding to the global maximum of the MP, which marks the highest discordance within the analyzed time series. The latter is expressed on a relative scale with respect to the performance obtained for a subsequence length of 80 samples.

Impact of noise The first test condition investigates the influence of noise at different SNR levels. Figure 2.1 shows the estimation accuracy of the MP as a function of the SNR, ranging from 20 to 80 dB. Even in the worst case, with an SNR of 20 dB, when the noise floor is comparable to the swell amplitude, the MP performance does not exhibit any significant degradation. Conversely, the estimation accuracy depends on the subsequence length: as expected, the shorter the subsequence, the more accurate the event localization. The 1-cycle subsequence ensures nearly optimal performance, with a mean error and as-

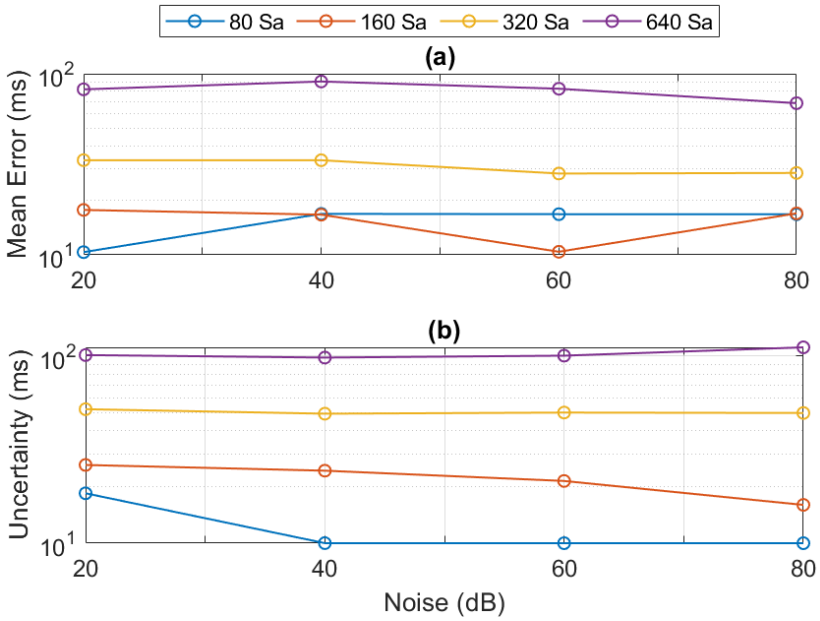

Figure 2.1: Swell starting time detection under different subsequence lengths and SNR levels: mean error (a) and associated uncertainty (b).

sociated uncertainty of approximately 10 ms, corresponding to the systematic contribution inherent in the MP computation. Nevertheless, even with an 8-cycle subsequence, the MP-based method keeps the mean error within 100 ms.

Impact of signal frequency Here, the dependence of the MP performance on the signal frequency is evaluated. As shown in Figure 2.2, the analysis covers the entire testing range for frequency measurements, from 42.5 to 57.5 Hz, as specified in [49]. The results demonstrate that the MP-based method is independent of the signal frequency. As in the previous test case, the estimation accuracy and the associated uncertainty are primarily determined by the subsequence length.

Impact of modulation frequency To evaluate the robustness of the proposed method in the presence of combined events, a test signal affected by amplitude modulation was used. The modulation depth was set to 5 a.u., equal to that of the swell, following a sinusoidal pattern whose frequency was varied within $[1/3, 2, 5, 8.8, 33 + 1/3]$ Hz, as inspired by the flicker standard [50] and the PMU standard [4].

As shown in Figure 2.3, the best performance is achieved at low modulation frequencies, with results consistent with the previous test cases. When

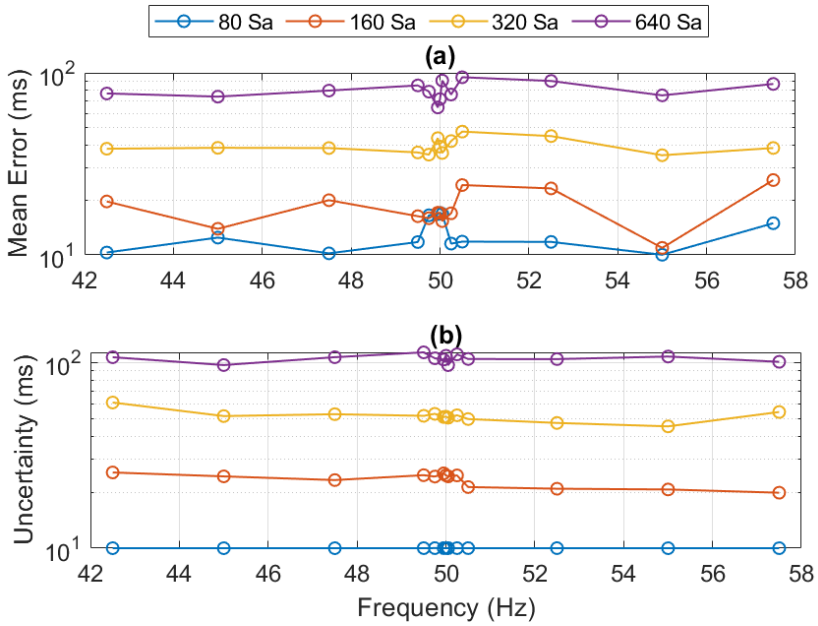

Figure 2.2: Swell starting time detection under different subsequence lengths and signal frequencies: mean error (a) and associated uncertainty (b).

the modulation frequency lies between 5 and 10 Hz, a performance improvement is observed for all subsequence lengths, particularly evident for 320 and 640 samples, where the subsequence length and modulation period become comparable. In this condition, the MP is likely to follow the modulation pattern and is facilitated in detecting the sharp transition introduced by the swell event. Conversely, at the highest modulation frequencies, the ratio between the subsequence length and the modulation period becomes irrational, and the estimation errors return to their expected values. Examining the associated uncertainties in the lower plot, a noticeable reduction can be observed compared with the previous cases. This allows concluding that the combined effect of two stationary conditions, off-nominal frequency and amplitude modulation, enhances the accuracy in detecting the transient event, namely the swell.

Impact of sampling rate The time resolution of the acquired signal, which is a function of the sampling rate, may significantly affect the method performance. To evaluate the MP performance with varying sampling rates, an application scenario is considered in which the SV stream is generated by a MU compliant with IEC 61850-9-2LE [13]. This standard contemplates only two sampling rates, namely 80 or 256 samples per nominal cycle. The adoption of different sampling rates, although technically feasible in customized implementations, would introduce interoperability issues and would not align with the

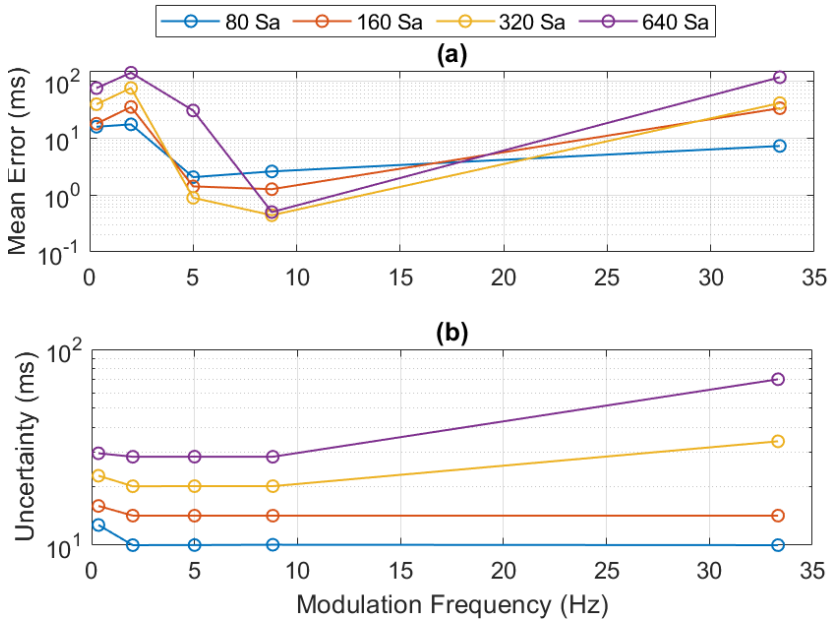

Figure 2.3: Swell starting time detection under different subsequence lengths and modulation frequencies: mean error (a) and associated uncertainty (b).

main principles of the IEC 61850 framework. Results are shown in Figure 2.4 in the form of error distributions obtained with 80 and 256 samples per cycle. For this analysis, a noise level of 60 dB was considered. Both the histogram and the Cumulative Distribution Function (CDF) plots exhibit a remarkable similarity between the two configurations. This result demonstrates the independence of the MP method accuracy from the sampling rate and its capability to ensure optimal detection performance even with relatively low time resolution of the acquired signal.

Standard test cases Once the MP sensitivity to variations of internal and external influence quantities has been evaluated, its robustness is here validated by considering two distinct PQ events, in order to provide a set of test cases that is more representative of plausible operating conditions.

Fake dip The first considered event is the so-called fake dip, a phenomenon observable at the secondary winding of a voltage inductive transformer in the presence of magnetic core saturation. This test signal is defined in Annex A of IEC TR 61869-103 [51] and still represents a challenging benchmark for PQ event identification algorithms. The corresponding waveform, shown in Figure 2.5(a), consists of a 50 Hz sinusoidal signal with an RMS amplitude of 20 kV and a total duration of 1 s. The event was inserted at a time instant of

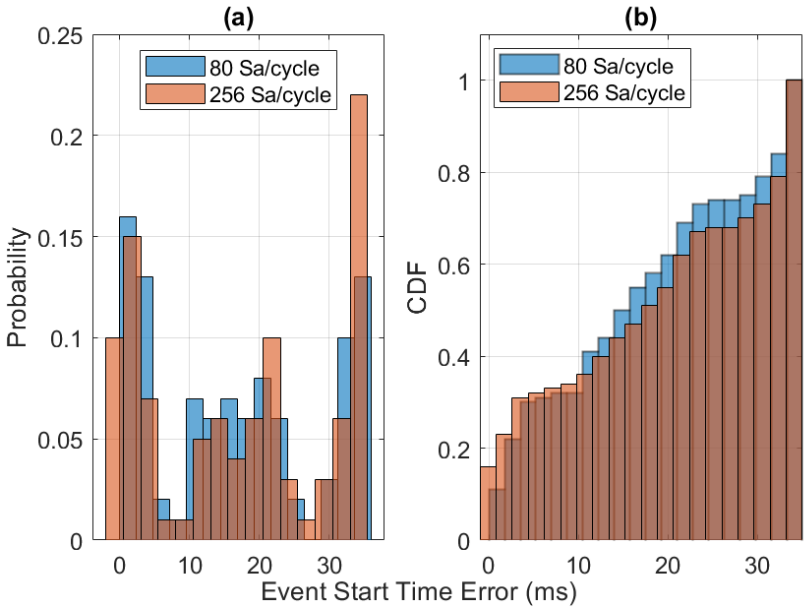

Figure 2.4: MP error distribution under a signal frequency of 50.05 Hz and noise level of 60 dB: histogram (a) and CDF (b).

0.4 s, corresponding to sample index 1600, and has a duration of approximately three nominal cycles. For this case, the results are presented by showing the MP output as a function of the subsequence length, as illustrated in Figure 2.5(b). The highest accuracy in the temporal localization of the event is achieved with a subsequence length of 160 samples. Nevertheless, all the considered configurations provide satisfactory results, as they successfully identify the event within ± 1 nominal cycle.

Rapid Voltage Change The second considered case is an RVC event, as described in test condition A13.5.2 of IEC 62586-2 [49]. As shown from the waveform in Figure 2.6(a), the signal frequency is constant at 50 Hz, while the signal RMS magnitude varies among three different levels. In the first 0.2 s, it is set to the rated value of 230 V; between 0.2 and 0.8 s, it drops to 208.6 V; and in the last 0.2 s, it settles at 223.1 V. In this case, within the 1-s observation interval, the MP must identify two transitions: the first occurring at 0.2 s, from 100 to 91 % of the rated voltage, and the second at 0.8 s, from 91 to 97 %. The MP output is shown in Figure 2.6(b), again as a function of the subsequence length. The method successfully detects both transitions and identifies the start of the first PQ event. The highest accuracy is achieved with a subsequence length of 320 samples, while the location error remains within a remarkably narrow range, namely between -10 and $+11$ ms.

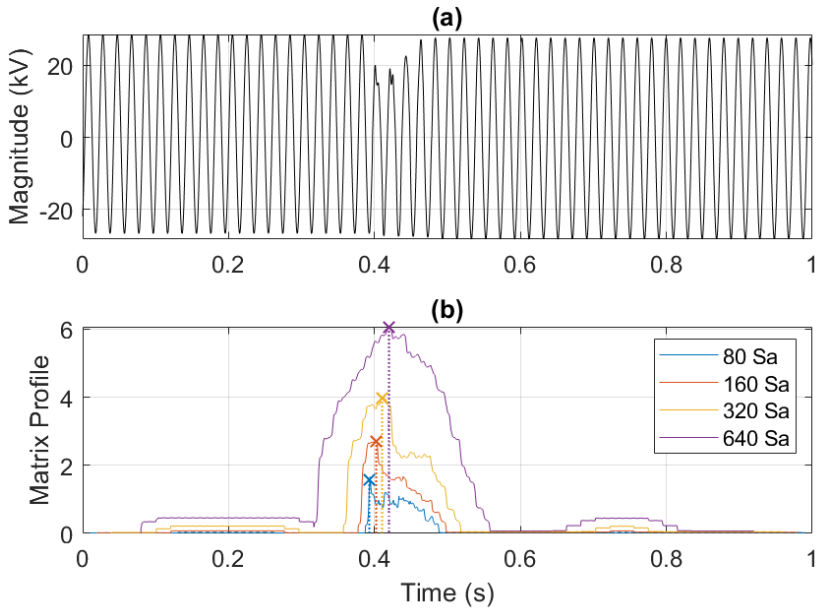

Figure 2.5: Fake dip detection under different subsequence lengths as recorded at the secondary winding of a voltage inductive transformer in case of magnetic core saturation [51]: test waveform (a) and MP output results (b).

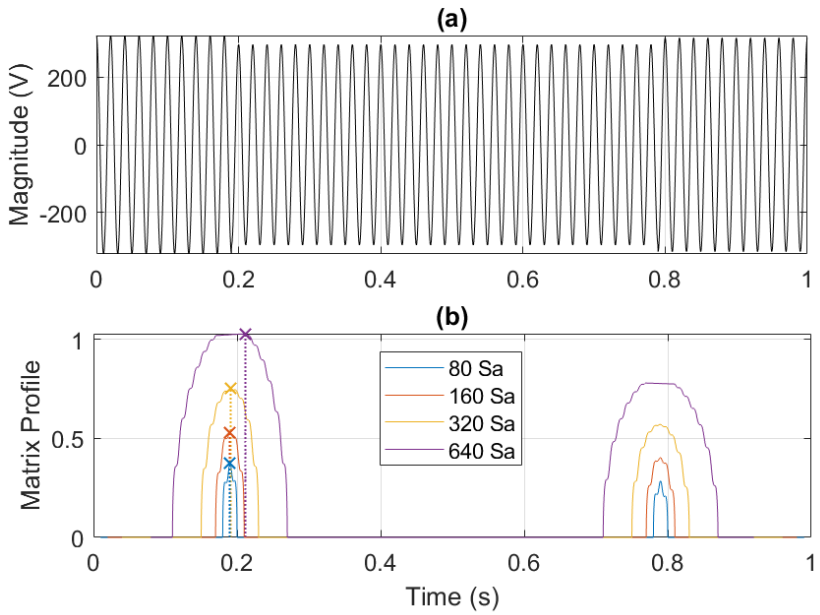

Figure 2.6: Rapid Voltage Change (RVC) detection under different subsequence lengths as per test condition A13.5.2 of IEC 62586-2: test waveform (a) and MP output results (b).

Summary The performance of the proposed method across the different test conditions is summarized in Table 2.1 as a function of the subsequence length. For each condition, the performance is evaluated in terms of both accuracy in detecting the event time occurrence and computational time. The former is expressed through the mean error and the corresponding uncertainty computed over the range of the considered parameter (for instance, in the case of additive noise, the overall variability across all SNR levels). The latter is reported in relative terms with respect to the results obtained with a subsequence length of 80 samples.

Table 2.1: Characterization of the MP-based detection of PQ events in SV streams as a function of the subsequence length

Test	Subsequence Length (samples)	Err ± Unc (ms)	Time (%)
Noise	80	15.2 ± 11.7	100.0
	160	15.4 ± 21.0	95.5
	320	30.8 ± 40.4	71.3
	640	81.0 ± 81.8	67.9
Frequency	80	10.1 ± 16.6	100.0
	160	18.2 ± 21.9	89.1
	320	39.7 ± 40.8	72.6
	640	80.4 ± 82.0	69.2
AM Modulation	80	9.0 ± 17.2	100.0
	160	17.7 ± 37.6	97.3
	320	31.2 ± 73.0	73.2
	640	72.1 ± 137.9	68.6
Fake Dip	80	-6.5 ± 11.5	100.0
	160	2.8 ± 20.3	93.7
	320	9.8 ± 40.2	72.4
	640	20.3 ± 80.1	68.9
Rapid Voltage Change	80	-10.3 ± 11.2	100.0
	160	-10.0 ± 20.1	91.4
	320	-9.5 ± 40.6	73.4
	640	11.3 ± 80.1	68.2

From the summary table, it is evident that the estimation accuracy mainly depends on the subsequence length, increasing as the length decreases. Conversely, the use of longer subsequences provides the benefit of reducing the computation time, by up to 30 % in the case of 640 samples. It is therefore worth examining the reasons behind the decrease in computation time observed as the subsequence length increases. This behavior is consistent with the findings reported in [34], where the authors show that the computation time of STOMP

slightly decreases for larger subsequences. This trend can be explained by two concurrent factors: as the subsequence length m grows, the total number of subsequences $(N - m + 1)$ to be analyzed decreases, thus reducing the number of pairwise comparisons; moreover, FFT-based implementations become relatively more efficient for longer sequences, since the computational overhead per evaluated window is amortized over a larger number of samples.

Considering the optimal results from the standpoint of event localization metrics, the characterization therefore suggests adopting an 80-sample subsequence despite the higher computational cost, as it ensures the best performance under most of the challenging operating conditions considered. Overall, the proposed method demonstrates to be a reliable detection approach for different types of PQ events, showing remarkable robustness even in the presence of high noise levels and combined disturbances.

2.3.2 Comparative analysis

This section compares the performance of the MP method with the most relevant and comparable approaches for real-time anomaly detection in time series identified in the literature. In particular, three reference techniques are considered: the first based on the RMS approach presented in [36], the second relying on the Discrete Wavelet Transform (DWT), and the third employing an enhanced version of the z-score method, referred to as the Modified Z-Scores (MZS) approach.

Comparison methods The RMS-based detection method described in [36] identifies outliers based on statistical thresholds. In this approach, the sample sequence is divided into 80-sample subsequences with a one-sample overlap, and for each of them, the RMS value is computed. Once the entire sequence has been processed, the mean μ_{RMS} and the standard deviation σ_{RMS} of the obtained RMS values are calculated. Under nominal conditions, the RMS values can be statistically modeled through a Gaussian distribution, where the standard deviation accounts for measurement and quantization noise. The MP- and RMS-based methods share the use of a moving window of equal length and both adopt an automatic detection criterion without requiring additional parameters. What differentiates them is the detection mechanism: in the MP method it is pattern-based, identifying abrupt discontinuities from recurring patterns, whereas in the RMS method it is threshold-based, detecting outliers under the assumption of quasi-stationary signals.

The DWT is a well-known signal processing technique that decomposes a signal into components characterized by both time and frequency resolution [52].

Through the successive application of low-pass and high-pass filters, the method separates the signal into approximation and detail coefficients, each representing specific frequency bands at different time scales. This property enables the analysis of localized variations and the identification of transient behaviors that are often invisible to classical spectral methods. As a result, the DWT is particularly effective for detecting anomalies by examining rapid or short-duration variations in the signal characteristics across multiple decomposition levels [53]. In this analysis, the comparison is carried out using the DWT with a Daubechies wavelet of order 4 applied to the entire sample sequence and decomposed over three levels. For each level, the standard deviation of the detail coefficients is computed, and a threshold equal to three times this value is defined. Coefficients exceeding the threshold are then selected as indicators of potential anomalies. Any discordant points are identified at the indices corresponding to the maximum value within each set of coefficients exceeding the threshold. These indices are then rescaled to map them back to their correct positions within the original sample sequence under analysis. The final discord position, corresponding to the estimated anomaly location, is obtained as a weighted mean of the scaled indices. Specifically, the detected discord indices at levels 0, 1, and 2 are weighted by 0.25, 0.50, and 1.00, respectively. This weighting scheme allows the final estimate to emphasize the contribution of higher-frequency details, which provide greater temporal resolution in identifying transient events.

Lastly, the MZS method is a real-time peak detection algorithm that dynamically adapts its threshold to identify abrupt changes in time series data, even in the presence of noise [54]. Unlike static thresholding techniques, it continuously updates its detection criteria based on recent samples, thus ensuring adaptability without requiring prior knowledge of the signal characteristics. Unlike the MP, which relies on a single parameter, the MZS method is governed by three main parameters: lag, influence, and threshold. The lag parameter controls the adaptation speed to long-term trends, the influence parameter determines how detected peaks affect the threshold update, and the threshold defines the number of standard deviations a data point must deviate from the moving mean to be considered an anomaly. Following the values adopted in [55], the parameters lag, influence, and threshold were set to 15, 0.4, and 3, respectively, to achieve a configuration that provides a balanced trade-off between noise rejection capability and detection sensitivity.

Comparison results The comparison of the three presented methods with the MP is carried out by simulating a challenging and realistic scenario, using a sample sequence affected by overlapping electrical phenomena. The testing signal has a unit amplitude of 1 a.u. and a frequency of 50.05 Hz. An amplitude

modulation with a depth of 5 % and a frequency of 5 Hz is superimposed on the signal, while an additive white Gaussian noise with an SNR of 40 dB is added to account for measurement and quantization noise. At the sequence midpoint, a sudden amplitude change, referred to as a jump, is applied. The performance of the analyzed methods is assessed by varying the jump magnitude from 10 % to 60 %, while maintaining a constant duration of 5 ms. The chosen event duration is motivated by the fact that such a short disturbance can be challenging to detect with standard techniques and has therefore been adopted as a stress test for the considered methods. As in the MP characterization phase, 100 independent tests are performed for each scenario, considering randomly generated additive noise.

The overall performance of the four analyzed methods is reported in Table 2.2, where the mean error values in event location and the corresponding uncertainty are provided for each jump amplitude. In this context, the uncertainty is computed as the 95th percentile of the error distribution over the 100 runs. Results show small errors for the MP method, ranging from 0.32 to 1.40 ms, with an uncertainty that decreases as the jump amplitude increases. The MZS method exhibits a relatively stable performance across different jump amplitudes, with error values consistently between 2.06 and 2.10 ms. This stability reflects no significant variation in detection capability as the jump amplitude increases, though maintaining relatively high uncertainty values. In the DWT method, larger errors are observed for smaller jumps, while its uncertainty significantly decreases at higher levels. Finally, the RMS-based method is unable to detect small jumps of 10 % and 20 %, being strongly affected by the superimposed modulation event. However, it maintains low uncertainty across all tests.

In conclusion, the MP offers a good balance between event detection accuracy and uncertainty across all analyzed cases, without requiring specific configurations to adapt to different jump types. Its capability to maintain low error and uncertainty values, even under challenging conditions, confirms its robustness and adaptability compared to the other analyzed methods. Unlike the MZS, DWT, and RMS-based approaches, the MP achieves accurate detection without the need for tuning parameters or prior knowledge of the signal characteristics, demonstrating a higher level of generalization and reliability.

2.3.3 Real test case

In this section, the application of the proposed approach to a set of synchronous data streams is presented. The objective is to assess the capability of the MP to correctly detect and locate the same event as synchronously recorded at different

Table 2.2: Comparison of methods performances across different jump amplitudes

Jump Amplitude	Method	Err ± Unc (ms)
10 %	MP	0.32 ± 2.92
	MZS	2.10 ± 11.54
	DWT	-172.12 ± 198.40
	RMS	-
20 %	MP	0.84 ± 1.81
	MZS	2.07 ± 11.52
	DWT	-172.57 ± 191.48
	RMS	-
30 %	MP	1.11 ± 1.17
	MZS	2.07 ± 11.57
	DWT	-173.52 ± 189.21
	RMS	5.00 ± 0.03
40 %	MP	1.24 ± 0.58
	MZS	2.07 ± 11.56
	DWT	-85.65 ± 116.35
	RMS	5.00 ± 0.03
50 %	MP	1.31 ± 0.55
	MZS	2.06 ± 11.59
	DWT	-8.82 ± 53.80
	RMS	5.00 ± 0.03
60 %	MP	1.40 ± 0.45
	MZS	2.10 ± 11.56
	DWT	3.37 ± 3.41
	RMS	5.00 ± 0.02

nodes of the grid. This analysis serves as a validation of the method's robustness in the presence of varying SNR levels and ongoing dynamics. Moreover, it enables a parallel examination of synchronous data streams and the aggregation of information related to the detected events.

The examined event was drawn from the Grid Event Signature Library (GESL), developed by the Oak Ridge National Laboratory (ORNL), a database of real power system events released to support the development of applications for electric network analysis [56]. In particular, the Event Signature ID 2015 is considered here, corresponding to a single-phase-to-ground fault that occurred on January 12th, 2016 on the US Western Interconnection. The dataset includes 14 PMU data streams, each with a reporting rate of 60 frames per second, in the context of a power system with a nominal frequency of 60 Hz. In this discussion, attention is restricted to the current phasors of two PMUs, namely PMU #2

and PMU #8, although similar considerations can be extended to the other data streams. To evaluate the MP performance within a SV framework, the PMU estimates of phasor magnitude, phase angle, and frequency are used to reconstruct a plausible approximation of the current waveform by means of a shape-preserving piecewise cubic interpolation technique introduced in [57]. In continuity with the simulation setup, the observation interval is limited to 1 s, and the sampling rate is set to 4800 Hz to maintain a rate of 80 samples per cycle.

Figures 2.7 and 2.8 show the results of the MP-based approach as a function of the subsequence length.

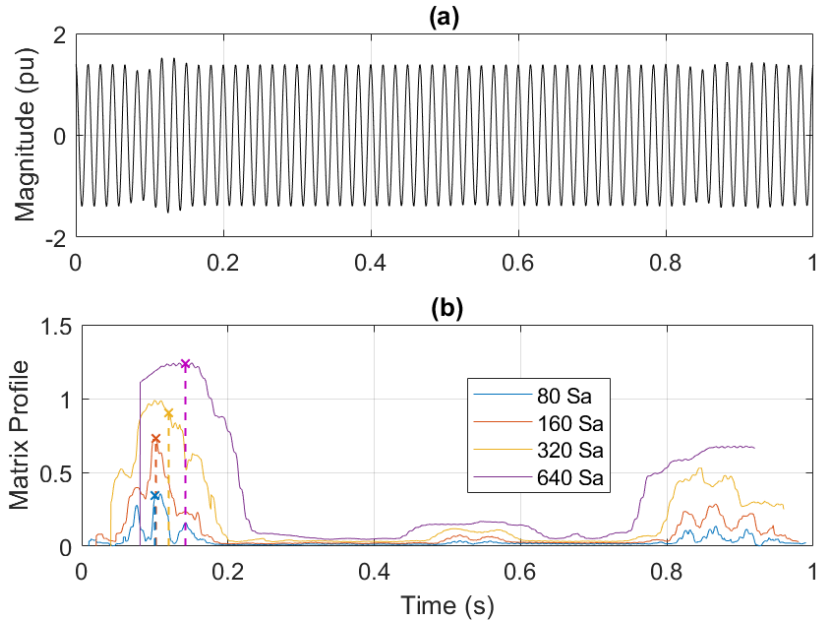

Figure 2.7: Waveform and MP-based analysis of a single-phase-to-ground fault recorded by PMU #2: time-domain signal (a) and detection results for different subsequence lengths (b).

The upper plots display the reconstructed current waveforms as captured by the two PMUs. In both data streams, the contingency occurs at 106 ms. The subsequent oscillations, however, differ depending on the considered PMU. In the PMU #2 stream, a modulated pattern appears around 810 ms, whereas in the PMU #8 stream, two magnitude variations are visible around 520 and 860 ms. The lower plots show the MPs obtained for different subsequence lengths, ranging from 80 to 640 samples, and considering the same cases analyzed in the simulation stage. It is worth noting that, in its current implementation, the MP method detects only the event characterized by the highest discrepancy with respect to the dataset, without providing the positions of other

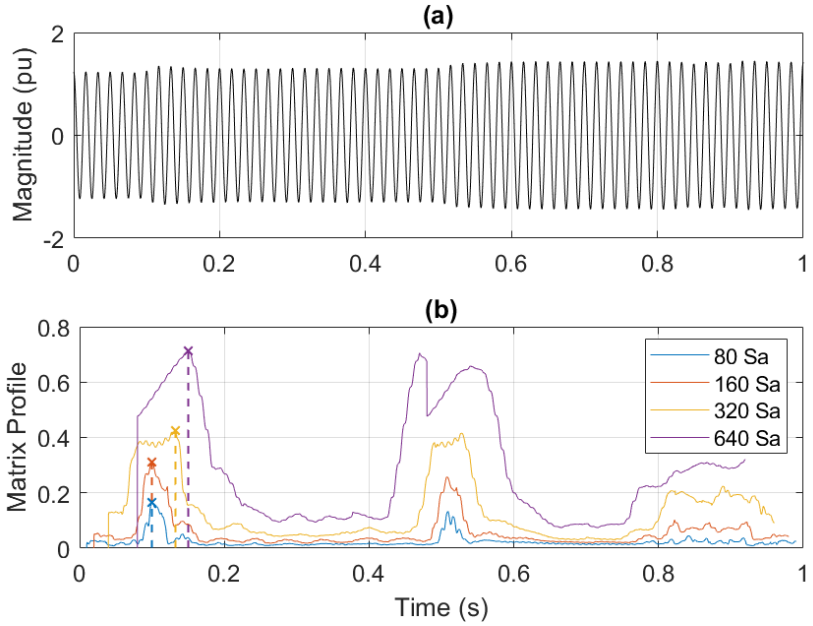

Figure 2.8: Waveform and MP-based analysis of a single-phase-to-ground fault recorded by PMU #8: time-domain signal (a) and detection results for different subsequence lengths (b).

noteworthy events, such as the magnitude variations caused by the power system response to the contingency. From the MP graphs, in both PMU streams, the proposed method successfully detects the event within a narrow interval around its actual occurrence time of 106 ms. Moreover, the detection performance proves to be extremely consistent between the two PMU streams: for the same subsequence length, the event is detected at nearly the same time instant. The best performance is achieved with a subsequence length of 160 samples, for which the event is detected at 101.5 ms and 99.5 ms in the PMU #2 and PMU #8 streams, respectively.

As a further validation, the same analysis was repeated in the presence of Gaussian noise with an SNR of 80 dB, superimposed on the current signals over 100 statistically independent realizations. The results of these tests are reported in Table 2.3, where the statistics of the detected time instant are presented in terms of mean error and associated uncertainty.

The results are extremely consistent across the two streams. In particular, shorter subsequences allow for a more precise localization of the event occurrence, while longer subsequences still ensure a mean error on the order of 2 nominal cycles.

Table 2.3: Statistical comparison of event detection time among two different PMU streams

Subsequence Length (samples)	PMU #2 Err ± Unc (ms)	PMU #8 Err ± Unc (ms)
80	-5.4 ± 8.7	-5.4 ± 8.9
160	-4.0 ± 18.8	-6.1 ± 18.6
320	15.1 ± 39.5	24.2 ± 37.3
640	35.4 ± 75.1	41.7 ± 78.4

2.4 Phasor Data Concentrator functionalities enhancement through Matrix Profile-based event detection

In this section, the MP-based approach is employed to introduce a new generation of PDC, namely the detection at PDC level (d@PDC) [11], featuring enhanced functionalities compared to traditional PDCs. In particular, the proposed d@PDC enables early detection of events and anomalies in incoming PMU data streams through a layered processing architecture composed of a first low-complexity stage for preliminary data screening and a second stage based on the MP. The key innovation lies in the introduction of a dedicated layer for event detection and analysis at the PDC level, where the d@PDC acts as an active element within a synchrophasor-based monitoring system, capable of performing preliminary analysis of incoming data. This can improve situation awareness and support the early identification of potentially harmful disturbances in the power system.

In the following, the proposed architecture is first described in detail, then the method is tested on simulated data and subsequently validated using real synchrophasor measurements obtained from the GESL.

2.4.1 Proposed approach

The proposed d@PDC aims to extend the functionality of the PDC node beyond its conventional role of time-aligning synchrophasor data, enabling anomaly detection and analysis. To keep the processing burden low, the d@PDC adopts a layered structure composed of two consecutive stages. The first stage performs a preliminary detection of anomalies in the incoming PMU data streams through a computationally light, threshold-based mechanism relying on z-scores. The second stage employs the MP method to verify the possible presence of such anomalies across the monitored area. If the z-score highlights an anomaly, an

MP-based similarity analysis is then carried out among the data streams to determine whether the event is local, perceived by only some PMUs, or global, perceived by all PMUs.

The main steps performed by the proposed d@PDC are outlined in Algorithm 1, which provides a detailed description of the implemented procedure and its operating logic.

Algorithm 1 - d@PDC: Detection and Analysis of Events from PMU Streams

Continuously:
i) Collect and align PMU data streams at the PDC.
ii) Monitor PMU streams for anomalies on a reference time window through z-score as in (Equation 2.12).
if *an anomaly is detected in one stream according to the threshold condition in Equation 2.13* **then**
  iii) Extract a subsequence (reference pattern) of length n centered on the anomaly
  for *each PMU stream* **do**
    iv) Compute the DP with respect to the reference pattern as in Equation 2.10;
    v) Identify the closest match and compare it to the threshold Equation 2.14
  if *the pattern is matched in all PMUs* **then**
    Classify the event as global
  else
    Classify the event as local

As previously introduced, the proposed procedure expands the traditional operation scheme of a PDC node. However, the conventional functionality, in which synchrophasor data from multiple PMU streams are continuously collected and time-aligned, is preserved and performed in step (i) of Algorithm 1.

The first proposed innovation is implemented in step (ii), where the basic functionalities of the d@PDC are complemented by a continuous background processing of PMU data aimed at monitoring the possible presence of anomalies. This is achieved through the computation of the z-score, applied to contiguous non-overlapping windows of magnitude values with a duration of 1 s, modeled as in Equation 2.1. The z-score represents a standardized value that quantifies how far a given element of the time series deviates from the mean, normalized by the standard deviation. The z-score z_i corresponding to the i^{th} sample of the time series is evaluated as:

$$z_i = \frac{x_i - \mu}{\sigma} \tag{2.12}$$

where μ and σ are the mean and standard deviation of the values in the processed window.
A magnitude value is flagged as anomalous if it exceeds a given threshold γ:

$$|z_i| > \gamma \tag{2.13}$$

where the value of γ can be set according to the desired sensitivity in the de-

tection of discrepancies. The crossing of the threshold γ would determine the activation of the MP, thereby initiating the event identification process in the other PMU streams. This logic aims to minimize the computational burden of the d@PDC. In fact, a continuous full MP computation would require comparing all subsequences of the time series. For this reason, the MP is executed only when an anomaly is detected, acting as a selective refinement mechanism rather than a continuous monitoring tool.

If a value exceeding the threshold is detected, a fixed-length pattern of n samples centered on the outlier is extracted from the time series, as indicated in step (iii) of Algorithm 1. The extracted data segment then serves as the reference pattern for the similarity search across the other PMU streams. The reference pattern, which becomes the base subsequence Z_b defined in Equation 2.9, is subsequently compared with consecutive portions of each PMU data stream using the DP. Accordingly, the $\mathbf{DP}_b$ vector, computed in step (iv) of Algorithm 1 by sliding Z_b, centered on the detected anomaly, along the time series corresponding to a generic PMU stream, is obtained as shown in Equation 2.10, where the index i iterates over the samples of the considered comparison PMU time series. This process is repeated for all the considered PMU streams. To minimize the computation time, the brute-force implementation was avoided, and the DP was computed using the MP implementation based on the MASS algorithm, available in the STUMPY [58] Python library.

Matching subsequences are identified by minimum values in $\mathbf{DP}_b$ compared to a dynamic threshold, used to evaluate whether the match is significant. This dynamic threshold, denoted as γ_d, is derived from the statistical properties of the PMU stream from which the reference pattern is extracted. Specifically, γ_d is computed as the mean value of the corresponding DP, representing the average dissimilarity between the base subsequence and all possible subsequences in that stream:

$$\gamma_d = \frac{1}{N} \sum_{i=1}^{N} \mathrm{DP}_b[i] \tag{2.14}$$

where N denotes the length of $\mathbf{DP_b}$, and the index i iterates over the elements of the DP computed using Z_b on the PMU stream from which the anomaly was originally detected. This operation corresponds to step (v) of Algorithm 1. If all PMUs show a matching subsequence within the threshold defined in Equation 2.14, the anomaly is classified as global, observed in different ways in all streams within a given time window, otherwise it is considered local.

Based on the above considerations, the proposed selective activation approach significantly reduces the average computational burden compared to continuous MP computation. The two-layer structure operates predominantly with

linear complexity, $\mathcal{O}(n_{\text{PMU}} \cdot N)$, where n_{PMU} is the number of PMU streams, while the higher computational cost, $\mathcal{O}(n_{\text{PMU}} \cdot N^2)$ using the MASS algorithm, occurs only in the limited cases where an anomaly is detected. This makes the proposed approach computationally efficient and well suited for real-time implementations.

At the end of the process, the d@PDC is enabled to send a dedicated data packet to the next PDC levels as an independent message, in accordance with the standard for asynchronous data communication [1]. This message will contain four parameters about the detected event: the type of anomaly, which can be global or local, the start and end timestamps of the analyzed time window in which the anomaly was identified, and the list of involved PMUs.

2.4.2 Testing and validation of the proposed method

In the following, testing and validation results of the proposed approach are presented, based on both simulated and real data obtained from the GESL developed by the ORNL. In the performed tests, the threshold γ was set to three times the standard deviation, while a fixed-length reference pattern with a window of 10 magnitude values was selected. According to the principle of the MP, this represents the only user-defined parameter of the method. As previously explained, the window is centered on the point of maximum deviation to capture the most representative portion of the detected event.

Simulated data In the simulation phase, three PMU data streams were considered in the presence of a signal with a nominal amplitude of 100 V RMS. In addition, Gaussian noise with an SNR of 60 dB was superimposed to account for a realistic PMU measurement noise. The reporting rate of the PMU streams is set to 50 frame per second (fps). To better illustrate the operation of the d@PDC, the analysis is limited to the magnitude values of the PMU measurements, on which the detection policy of this framework is based.

Perturbations of the nominal signal were introduced as magnitude step changes, and different event durations were simulated. These events reproduce possible voltage variations detected by distinct PMUs located at remote points of the electrical system, also taking into account the distance among the measurement devices. The characteristics of the simulated events, in terms of magnitude variation and time duration as observed by the three PMUs, are summarized in Table 2.4.

Figure 2.9 shows the time trend of the magnitude measurements from the three simulated PMUs under test over a 1 s observation window. As summarized in Table 2.4, each signal exhibits a different amplitude drop. PMU1, assumed to

Table 2.4: Parameters of the simulated events for each PMU

PMU	Magnitude Variation (%)	Duration (ms)
PMU1	−15	80
PMU2	−5	120
PMU3	−2.5	120

be the closest to the event, shows the largest magnitude variation, with a 15 % drop lasting 80 ms. The event was simulated by introducing a marked temporal separation and amplitude difference among the PMU streams, in order to allow a preliminary validation of the d@PDC strategy. Figure 2.10 shows the z-score values of the three streams together with the detection thresholds. The event

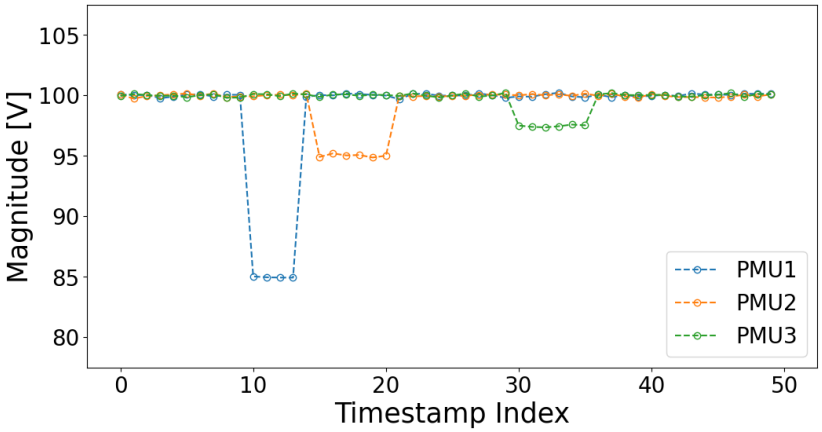

Figure 2.9: Simulated data: magnitude of data streams from the three PMUs.

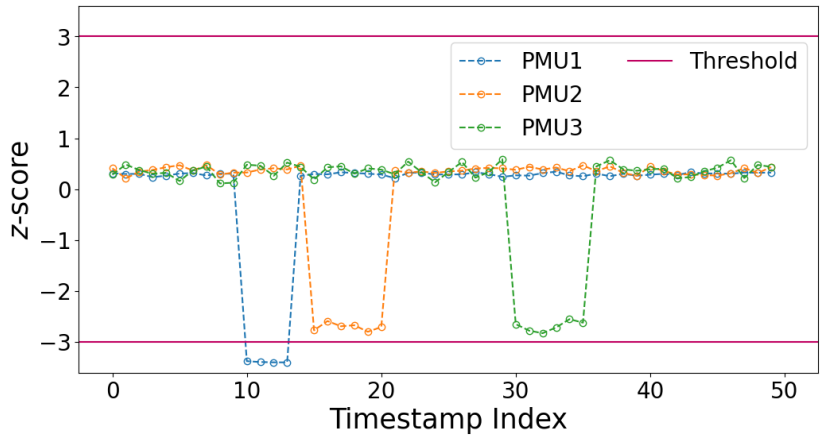

Figure 2.10: Simulated data: z-scores of input data

is identified in the PMU1 stream at timestamp 10, where the z-score exceeds the threshold. This triggers the selection of the reference pattern according to Equation 2.13 and the subsequent pattern-matching phase. Figure 2.11 shows the subsequence of 10 magnitude values extracted from the PMU1 data stream, corresponding to a 200 ms time window, selected as the reference pattern. This reference pattern is then used, through the computation of the DPs, to identify possible similar behaviors in the data streams of the other PMUs, as described in step (iv) of Algorithm 1.

The DP results for all PMUs are shown in Figure 2.12, where the red crosses indicate the position of the best match for each PMU. The zero DP value observed in the PMU1 stream at the best-match point confirms that it represents the origin of the reference pattern. In all other cases, the minimum DP values lie

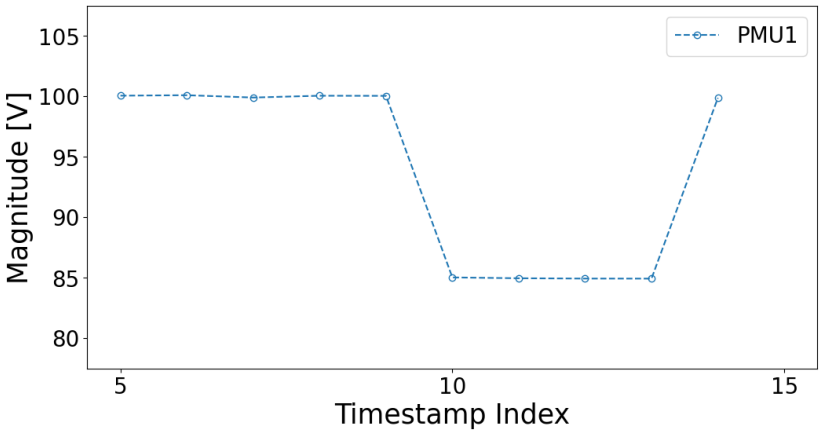

Figure 2.11: Simulated data: reference pattern

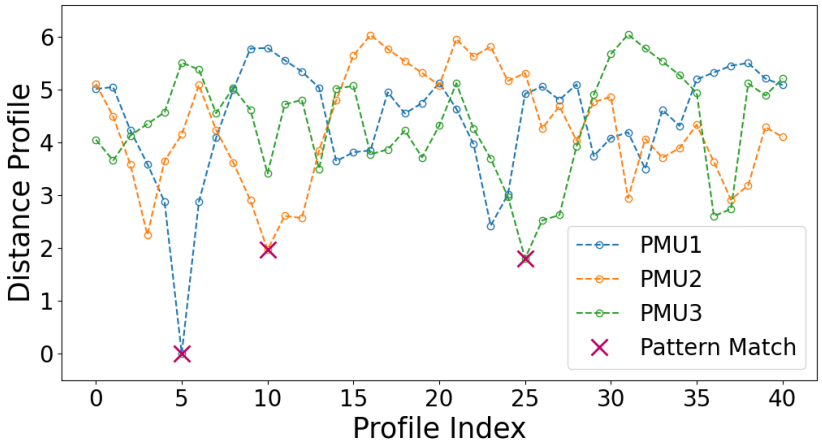

Figure 2.12: Simulated data: DPs of input data

below the dynamic threshold, indicating that patterns similar to the reference are present across the PMU streams. Consequently, the anomaly is classified as global, and the corresponding data can be transmitted to the next-level PDC for further analysis. To verify the event classification logic, the test was repeated by removing the disturbance from PMU3. As a result, the pattern was successfully identified only in PMU1 and PMU2. The system correctly classified the anomaly as local, assuming that the event affected two nearby PMUs, since it did not impact all the considered streams.

Real test case To validate the proposed detection scheme, real synchrophasor data from the GESL dataset were considered, focusing on a disturbance recorded by several PMUs. The dataset identified as signature ID 2015 contains time-synchronized measurements from 14 PMUs with a reporting rate of 30 fps on

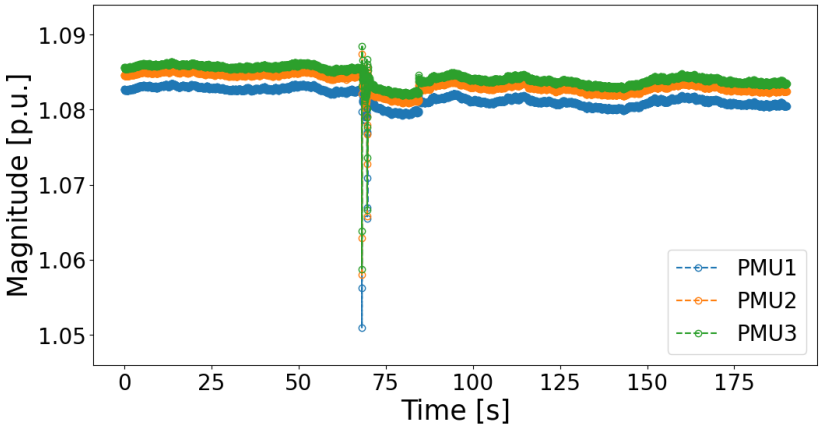

Figure 2.13: Real data: magnitude of data streams from the three PMUs.

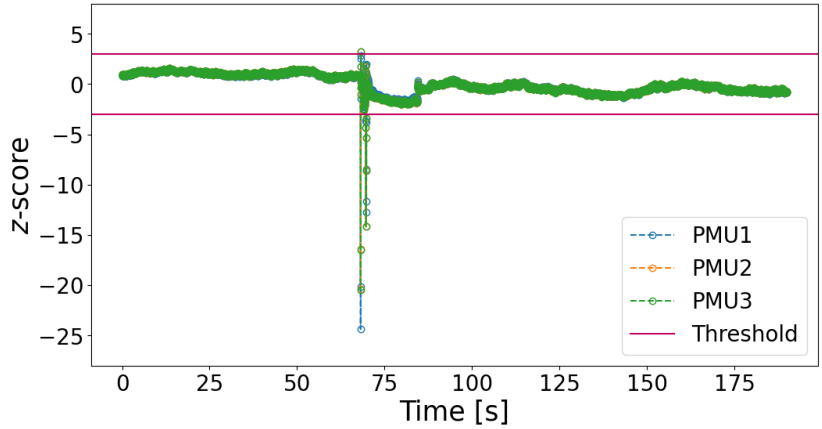

Figure 2.14: Real data: z-scores of input data

a 60 Hz system, recorded in 2016. For simplicity, only PMUs 2, 3, and 8 are considered in this study. According to the event tags attached to the dataset, the measurements captured a nonspecific equipment failure involving a single-phase-to-ground fault on overhead conductors.

Figure 2.13 shows the normalized voltage magnitude trends recorded by the three considered PMUs. A sharp voltage drop is observed, around the relative timestamp 70, simultaneously across all three PMU streams. This is followed by a transient oscillation and a step change in the voltage level. The overall time window is approximately 177 s-long. The selected reference pattern from the PMU1 data stream, corresponding to a 10-sample interval of 0.3 s, is shown in Figure 2.15.

Figure 2.14 shows the resulting z-score values obtained after processing by

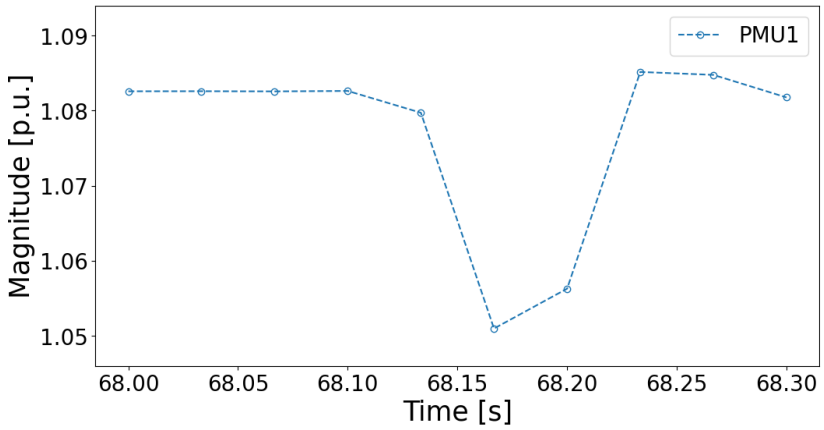

Figure 2.15: Real data: selected pattern

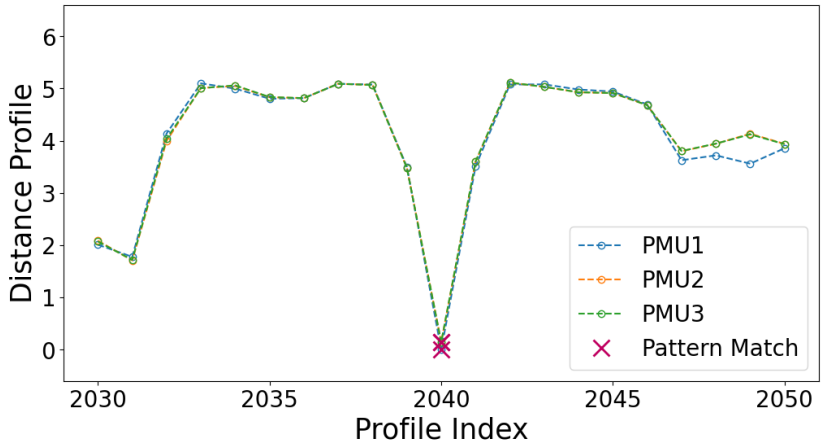

Figure 2.16: Real data: DPs of input data

the d@PDC, following the execution of step (i) of Algorithm 1, together with the applied detection threshold. The event was correctly identified, as the z-score clearly exceeds the threshold in all three PMU streams.

Figure 2.16 shows the DPs computed for each PMU stream using the reference pattern depicted in Figure 2.15. The red crosses mark the positions of the closest matches for each PMU. As expected, the PMU1 stream, from which the pattern is extracted, exhibits the minimum distance at the corresponding profile index. This match, included only for completeness, is not considered in the subsequent event analysis. The reference pattern is indeed compared exclusively with the other PMU streams, and the dynamic threshold is applied to evaluate the match significance. Since all the obtained distances lie below the threshold, the event is correctly classified as global.

Chapter 3

Comprehensive methodology for the characterization of random errors in Phasor Measurement Units

Synchrophasor data provided by Phasor Measurement Units (PMUs) are employed in Wide Area Monitoring Systems (WAMSs) for several applications, including real-time state estimation of the electrical grid, event localization, and support to protection and control functions. The effectiveness of these applications is therefore inherently linked to the reliability and quality of the synchrophasor data, which in turn depend on the performance of the PMUs. A detailed characterization of the measurement output of these devices is therefore crucial. However, this process must be carried out carefully, since, as discussed in Section 1.3, several sources of uncertainty can compromise the quality of the acquired measurements. It is thus necessary to ensure that variations of external parameters affecting the device operation are continuously monitored and, when possible, controlled so that they remain within well-defined and acceptable ranges.

Building on these premises, this study focuses on architectures and methodologies for the laboratory characterization of PMUs under controlled conditions. The discussion draws on the studies presented in [59], [60] and aims to present a rigorous methodology for constructing statistical models of synchrophasor measurement errors. The proposed methodology is designed in order to be able to isolate the intrinsic behavior of the PMU from any external influences, and

therefore provide an accurate representation of the device's performance. To this end, this chapter first reviews the most commonly adopted error models and the approaches used in the literature to assess them, highlighting their main limitations. It then introduces a robust laboratory-based procedure designed to eliminate external sources of uncertainty that may compromise the validity of the characterization results. Finally, the experimental results obtained from tests performed on commercial devices at the Instrumentation and Measurement Laboratory of the University of Cagliari are presented, from which separate statistical models for Magnitude Errors (MEs) and Phase-Angle Errors (PEs) are derived.

3.1 Review of statistical models for PMU random errors

According to classical measurement theory, the uncertainty of PMU measurements can be expressed as the sum of a systematic and a random component. In evaluating synchrophasor measurements, special attention is given to modeling the random component of measurement errors, typically represented by statistical distributions. While the systematic component can be compensated through prior knowledge of the corresponding offsets, estimated by means of specific characterization procedures, the random component represents an intrinsic and unavoidable element that must be accurately quantified and described. In particular, its contribution plays a decisive role in the overall uncertainty, directly affecting protection and control decisions, whereas the shape of its statistical distribution becomes particularly relevant in advanced monitoring applications relying on complex mathematical models, such as state estimation [61], line parameter estimation [62], and fault location [63].

In recent literature, several statistical models have been proposed to describe PMU measurement errors, although a coherent framework regarding the origin of the data used to derive or assume such models is still lacking. In [64], a comprehensive statistical analysis of PMU measurement errors was carried out, showing that the traditionally assumed Gaussian nature of such errors does not hold in practice. The authors examined both real and synthetic datasets and found that PMU voltage and current measurements are affected by non-Gaussian noise, whose distribution can be effectively described using Gaussian Mixture Models (GMMs). However, their data-driven methodology also accounts for external influence quantities within the measurement chain, including current transformer saturation and cable length, thereby diverting the analysis from the intrinsic metrological characterization of the PMUs. Similarly, [65] an-

alyzed distribution-level synchrophasor measurements collected from real-world systems through both online and offline experiments. By comparing synchronized measurements from multiple PMUs, the study demonstrated that measurement errors follow non-Gaussian distributions characterized by asymmetry and multiple peaks. The authors proposed the use of GMMs to represent these errors more accurately and realistically, noting that non-Gaussian behavior persists even under controlled laboratory conditions. In [66], the focus was again on GMMs, proposed for modeling the random component of PMU measurement errors. The authors introduced a two-mode GMM with parameters estimated through a constrained Expectation–Maximization algorithm, aiming to reproduce the bimodal nature of the simulated error distributions. By analyzing differences between consecutive samples, they also devised a method to infer the random error distribution without requiring true reference values. In [67], long-tail non-Gaussian distributions were identified through the analysis of redundant field measurements collected from the North American transmission network. The study demonstrated that, under real operating conditions, PMU measurement errors deviate from the Gaussian assumption typically adopted in power system applications, exhibiting heavy-tailed behaviors consistent with t-Student, Laplace, or logistic distributions. However, the conclusions are inherently affected by the non-stationary nature of field data, which makes it difficult to isolate the intrinsic contribution of the measurement device. A more controlled approach was adopted in [68], where a laboratory characterization based on dynamic test signals and a high-precision calibrator was performed. However, the use of dynamic waveforms directly influences the resulting error distributions, which in this case reflect the measurement conditions rather than the intrinsic behavior of the device itself. Consequently, the resulting statistical models cannot be regarded as fully representative of the PMU's inherent random error characteristics. Finally, the hypothesis of non-Gaussian measurement noise was assumed in [69] to assess its impact on state estimation algorithms, considering Laplace, Weibull, Uniform, and Gaussian-mixture distributions. However, the justification for non-Gaussianity was attributed to external factors such as electromagnetic interference and inverter-based generation, thus once again diverting the focus from the intrinsic behavior of the PMUs.

In this scenario, these results, if not properly contextualized, may lead to misleading assumptions in applications where the choice of the statistical model of measurement errors is critical. Attention should therefore be paid to the measurement conditions under which such models are applied. Data collected under uncontrolled conditions or from dynamic test signals may not reflect the intrinsic behavior of the measurement instrument, as the former include the influence of external phenomena and the latter are affected by signal variability

and non-stationary effects that distort the underlying statistical distribution.

Building on this consideration, a systematic methodology is proposed for the experimental characterization of PMU measurement errors, aimed at minimizing external sources of uncertainty that introduce nonstationarity into measurement data. The proposed approach draws inspiration from [70], where the analysis performed on PMUs from different vendors was carried out under controlled laboratory conditions, and its effectiveness is demonstrated through the results presented in [59], [60]. Specifically, [60] extends the study in [70] to current measurements, while [59] presents an in-depth experimental investigation on a set of PMUs from the same manufacturer, aimed at assessing the variability of the statistical error models as a function of operating conditions and unit-to-unit differences within a controlled test environment.

3.2 Synchrophasor data collection and analysis in controlled laboratory environment

In the proposed methodology, the PMU is analyzed as a closed system, under nominal operating conditions and isolated from any external influence, namely controlled environmental parameters and sinusoidal input signals at 50 Hz with a waveform as close as possible to the ideal one. For this reason, Instrument Transformers (ITs), typically present in real-world architectures to condition current and voltage signals for acquisition by the PMUs and representing the main sources of uncertainty during the signal acquisition stage [71], are not considered in the analysis. Indeed, they require dedicated characterization campaigns [72], the results of which can later be combined with those of the PMUs to obtain comprehensive uncertainty models.

The proposed approach achieves this goal by addressing two complementary aspects: the design of a laboratory setup aimed at minimizing uncertainties arising from environmental factors and input signals, and the implementation of a rigorous data analysis methodology intended to identify non-stationarities and components clearly attributable to factors external to the PMUs. These two aspects are presented and discussed separately in the following sections.

3.2.1 Laboratory test architecture

The architecture developed for the experimental tests is illustrated in Figure 3.1. The diagram includes three PMUs and represents the general layout of the characterization setup, although some of the results presented in Section 3.3 refer to test configurations in which the PMUs were tested individually.

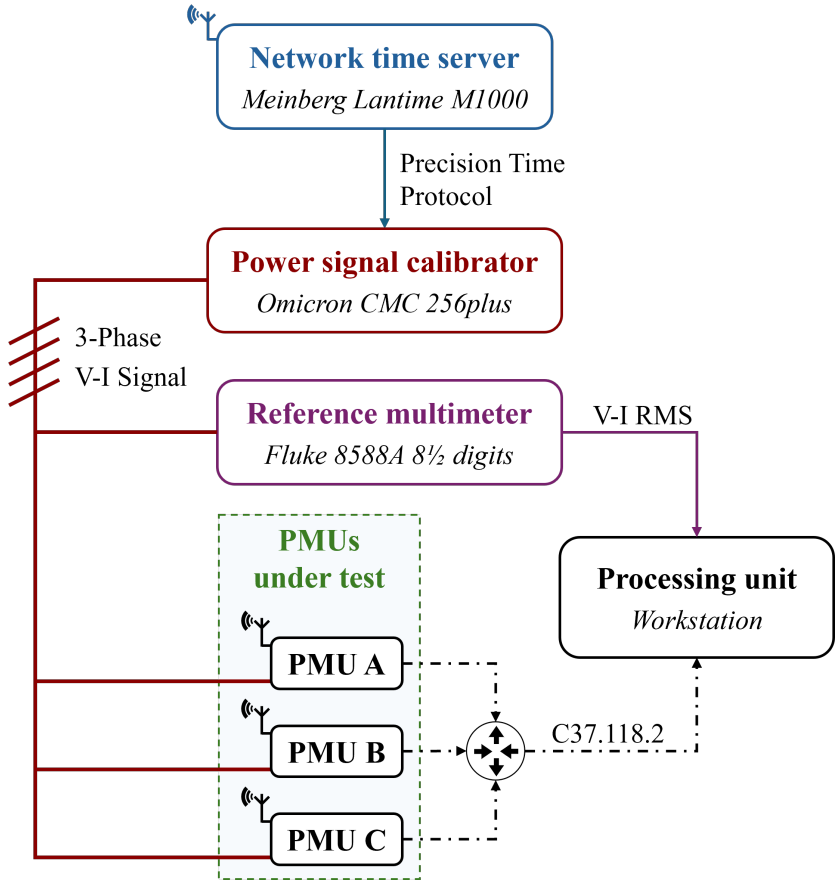

Figure 3.1: Laboratory test architecture developed at the laboratory of Instrumentation and Measurement of the University of Cagliari.

As displayed in Figure 3.1, the three PMUs under test (PMU A, B, and C) receive the three-phase voltage and current signals from the Omicron CMC 256plus power signal calibrator [73]. This instrument represents a key element of the characterization setup, as it provides stable and controlled input signals to the PMUs under test, allowing an accurate evaluation of their behavior under electrical steady-state conditions [74]–[77]. The tests are carried out at a voltage level of 100 V and at current levels ranging from 0.5 A to 5.0 A. For these levels, the manufacturer declares the same typical accuracy, equal to 0.015 % of reading plus 0.005 % of the device Full-Scale Range (FSR).

Both the calibrator and the PMUs operated under a single time synchronization source to ensure a common phase reference. The calibrator was synchronized via the Precision Time Protocol (PTP) in the Utility Profile configuration, provided by the external Global Navigation Satellite System (GNSS) receiver Meinberg Lantime M1000. The PMUs were synchronized either through their

embedded Global Positioning System (GPS) receivers or through the same PTP signal distributed by the GNSS receiver, depending on their embedded hardware configuration. To guarantee a high level of synchronization accuracy, all antennas were installed on the laboratory roof at a sufficient distance from one another to avoid interference, and their connection cables were of equal length. Nevertheless, a further assessment of the calibrator voltage output accuracy was performed before proceeding with the actual PMU characterization process. This preliminary procedure, recommended to ensure the quality of the generated calibration signal, is intended not only to characterize the calibrator offset errors, so that they could be compensated for when evaluating the MEs of the PMUs, but also to assess the experimental uncertainty of the generated signal, verifying its compatibility with the measurement uncertainty of the PMUs. The reference instrument selected for this evaluation is the Fluke 8588A 8 1/2-digit multimeter [78], which is able to provide a high resolution of 7 1/2 digits in the measurement of Alternating Current (AC) voltage and current signals. The manufacturer claims an accuracy of 5 ppm of reading plus 5 ppm of the FSR, considering a 95 % confidence level for voltage Root Mean Square (RMS) measurements. For current RMS measurements, at the same confidence level, the declared accuracy is 10 ppm of reading plus 10 ppm of the FSR up to 1 A, and 50 ppm of reading plus 20 ppm of the FSR up to 10 A. These specifications allow the multimeter to be adopted as a reference characterization device for the voltage and current outputs of the CMC 256plus.

All devices were managed by a single control unit, which also acted as a data collector, acquiring both the voltage and current RMS measurements from the multimeter and the IEEE C37.118.2 synchrophasor packets [1], as well as performing the processing required for the statistical analysis.

3.2.2 Proposed methodology

The proposed methodology for PMU ME and PE characterization is here presented. It is important to underline that these two quantities may exhibit different behaviors [70], and therefore they must be analyzed separately. To investigate the intrinsic behavior of the Devices Under Test (DUTs), the data used for the characterization must be as little as possible affected by external factors, which could introduce non-stationarities and compromise the statistical analysis. This is ensured first by means of an appropriate characterization architecture, as described in Section 3.2.1, and then through dedicated analysis tools designed and assembled to identify and mitigate these unwanted influences, as described hereafter.

Figure 3.2 shows a schematic representation of the proposed approach. Syn-

chrophasor data are processed through several stages, each involving specific analysis tools. The ultimate objective of deriving statistically significant distribution models for the MEs and PEs of the PMUs under test is achieved through a generalized procedure applicable to both quantities. Nevertheless, as highlighted, the analysis must proceed along two parallel and independent paths, reflecting the different behavioral nature of the two quantities of interest.

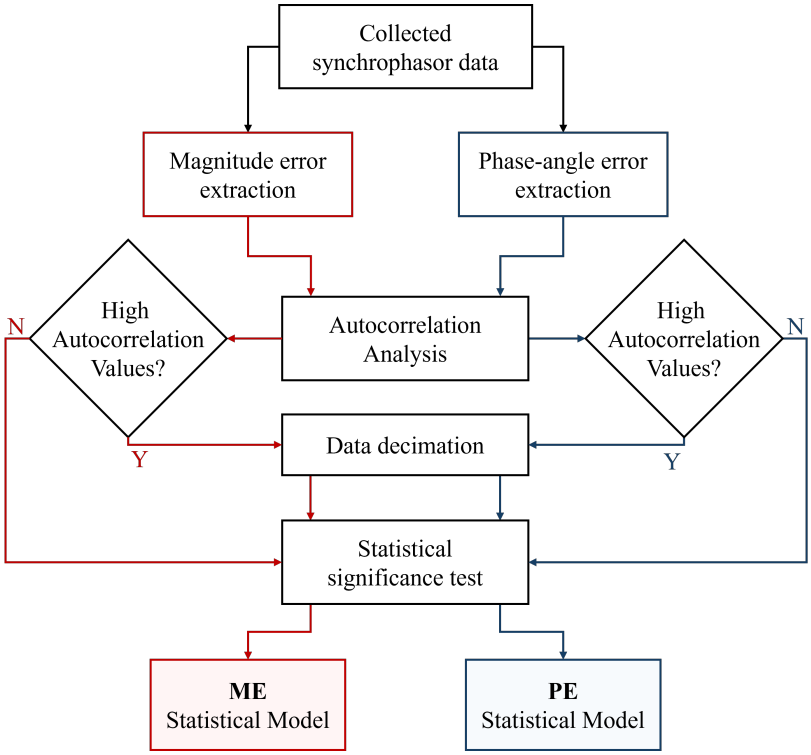

Figure 3.2: General scheme of the methodology proposed for PMU error characterization.

3.2.2.1 Preliminary performance evaluation and error definition

The statistical analysis of magnitude and phase-angle errors is to be preceded by a preliminary evaluation of the PMU performance compliance, which is carried out through the Total Vector Error (TVE) index, defined in [4] as:

$$\text{TVE } [\%] = 100 \cdot \frac{\sqrt{\Delta X_r^2 + \Delta X_i^2}}{|\bar{X}|} \tag{3.1}$$

where ΔX_r is the difference between the real parts of the reference and measured synchrophasors, while ΔX_i is its counterpart for the imaginary parts. Moreover, $|\bar{X}|$ denotes the magnitude of the reference synchrophasor $\bar{X}$, where $|\cdot|$ is the

magnitude operator. The TVE index is representative of the overall behavior of PMUs, since it incorporates the ME and PE, thus providing a quantitative feedback on performance and the verification of synchrophasor standard compliance, which imposes a 1 % upper limit in steady-state operating conditions [4]. In this context, synchronization plays a crucial role in PEs, as their behavior depends on the evolution of the device time base. Considering a system frequency of 50 Hz, a time base shift of 1 µs results in a PE of approximately 0.03 crad, corresponding to a 0.03 % increase in TVE.

Following the performance verification of PMUs under test, the characterization procedure bifurcates, considering from this point forward the magnitude and phase-angle measurements separately. Errors on these quantities can be computed starting from the estimated and reference synchrophasors:

$$\text{ME } [\%] = 100 \cdot \frac{|\widehat{\bar{X}}| - |\bar{X}|}{|\bar{X}|} \tag{3.2}$$

$$\text{PE } [\text{crad}] = 100 \cdot (\angle\widehat{\bar{X}} - \angle\bar{X}) \tag{3.3}$$

where $\widehat{\bar{X}}$ is the measured synchrophasor and $\angle\cdot$ indicates the angle operator.

3.2.2.2 Data preprocessing and verification of statistical independence

Once the measurement errors have been computed, the actual characterization procedure begins, and the first step involves cleaning the data from possible contributions external to the device operation. A visual inspection of the dataset under examination is recommended to identify the portions most suitable for statistical analysis. Although data are collected in a controlled laboratory environment, non-stationary processes may still interfere during experimental tests, for instance due to small, uncontrollable fluctuations in environmental parameters. An example is shown in Figure 3.3, which reports the temporal evolution of voltage measurements acquired during a testing campaign in the Instrumentation and Measurement Laboratory of the University of Cagliari.

The example provided highlights a non-stationary behavior, evidenced by a variation of the mean value over time. Environmental parameters such as temperature can interact with the device operation, leading to local fluctuations in the arithmetic mean of the error vector. When such phenomena occur, analyzing smaller portions of the dataset increases the likelihood of identifying stationary data windows suitable for statistical analysis.

The phenomena just described are generally nondeterministic. However, in synchronized measurement characterization architectures, data collection can

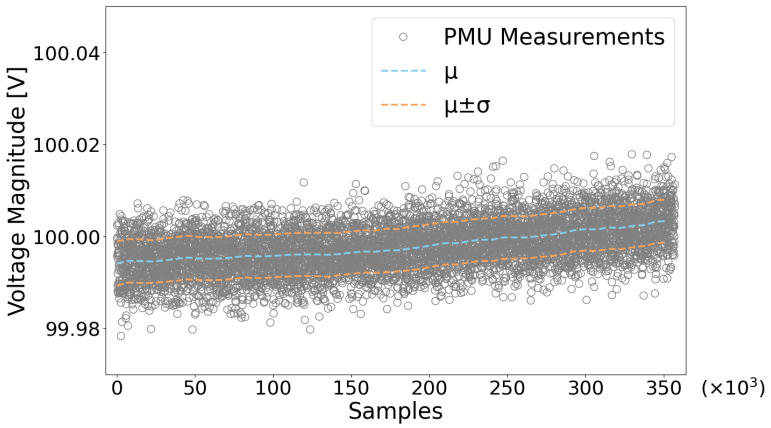

Figure 3.3: Effect of environmental parameter fluctuations on measurement data in a two-hour laboratory test.

also be affected by deterministic influences related to the synchronization system. In such systems, each device operates according to its internal clock, which is cyclically updated by the synchronization mechanism to compensate the natural drift. With the adoption of PTP and GPS in the present test setup, the clock correction rate is equal to 1 s. These periodic corrections may manifest as recurring patterns that introduce parasitic periodicities superimposed on the measurement data, ultimately distorting the statistical properties of the dataset. Such periodic components, if not directly attributable to the DUT, must be avoided when constructing a valid statistical model, as they do not originate from the DUT itself and furthermore violate the assumption of randomness that underlies most statistical analyses. In some cases, depending on the specific DUT, identifying and removing these patterns may not be straightforward, since their amplitude may be comparable to that of the background noise or their periodicity may extend over long time intervals. For this reason, visual inspection alone is insufficient to reliably detect such effects.

To address this issue, an autocorrelation analysis of the data is proposed as an integral part of the methodology. This analysis allows quantifying the degree of dependency between samples as a function of their temporal distance, thus revealing the presence of hidden deterministic behaviors or periodicities that could otherwise remain unnoticed. By highlighting correlations that persist over successive samples, the Autocorrelation Function (ACF) serves as a diagnostic tool to verify the statistical independence of the data, which is an essential prerequisite for the validity of the subsequent distribution modeling based on ergodicity assumption. Indeed, high autocorrelation values within a limited data window indicate a lack of statistical independence, leading to empirical

distributions that are not representative of the true stochastic behavior of the measurement errors.

3.2.2.3 Significance tests

At this stage of the analysis, stationary ME and PE datasets are available, as ensured by the precautions adopted during data acquisition and preprocessing. It is therefore possible to proceed with the actual statistical analysis, which represents the final step of the proposed methodology. The type of analysis to be performed depends on the specific research objectives. In this case, the main goal is to verify whether the Gaussian model provides an adequate statistical description of the MEs and PEs. In fact, the MEs are expected to follow a normal distribution, as there is no apparent reason to assume a different statistical behavior. The case of the PEs, however, can be more complex due to the influence of synchronization effects.

To verify the Gaussianity of the data, the Shapiro-Wilk (SW) test [79] is employed. This test assesses the normality of a dataset by comparing the empirical distribution of the analyzed vector with the theoretical Gaussian distribution. The result is expressed in terms of the p-value, which can assume positive values lower than 1. The p-value indicates whether the null hypothesis of normality should be rejected, based on a predefined significance level α. When the p-value is lower than α, the null hypothesis is rejected and the dataset cannot be considered normally distributed. In this analysis, the significance level is set to 0.05, a commonly adopted threshold in the scientific literature [64], [65], [70].

The SW test is particularly suitable for medium-sized datasets, as it provides a good trade-off between sensitivity and robustness in detecting deviations from normality. For large samples, the test may indicate non-normality even in the presence of negligible deviations, whereas for small samples it may fail to reveal significant departures from the Gaussian model. In the R programming language [80], where the SW test is included in the base package, the maximum input vector size for the corresponding function is limited to 5000 samples. For the purposes of the present analysis, this sample size is adequate; for larger datasets, alternative methods such as the Anderson–Darling or Kolmogorov–Smirnov tests are recommended.

3.3 Experimental results

In this section, the results of the characterization process carried out on data collected during experimental tests at the Instrumentation and Measurement Laboratory of the University of Cagliari are presented. The discussion will

consider three commercial PMU, same type and manufacturer but different uptime, which were tested using three-phase steady-state voltage and current signals, respectively with 100 V RMS and 5 A RMS values, thereby simulating the typical operating regime of these devices when they are interfaced with ITs in transmission grids. The PMUs were tested following two different approaches: first individually, in what follows referred to as stand-alone tests, then in a parallel (for voltage tests) or series (for current tests) configuration, feeding them with the same signals from the calibrator, under the condition of negligible load effects, ensured by the high impedance of the PMU voltage input channels and the low impedance of the current ones. In all cases, the tests lasted two hours and were performed at a controlled ambient temperature of 23 °C, as specified in [81] and in compliance with [4]. During the tests, particular attention was paid to the time synchronization quality of the PMUs, verified through the analysis of the status word contained in the C37.118.2 packets. Synchronization monitoring was performed in real time throughout the data acquisition process by means of dedicated software capable of interrupting the test in the event of a detected synchronization issue. All the PMUs were tested with a reporting rate configuration of 50 frame per second (fps).

The discussion that follows is organized according to the same steps described in Section 3.2.2. As a preliminary stage, the performance of the PMUs is first evaluated. Then, the most representative results are presented to demonstrate the effectiveness of the proposed characterization methodology. As a further extension of the study, in Section 3.3.5 results from the current characterization of two different PMU models are also reported.

3.3.1 PMU performance evaluation

As a result of the preliminary evaluation of the PMUs performance, Table 3.1 reports the voltage TVE % obtained for the three PMUs from the same manufacturer (identified as PMU 1, PMU 2, and PMU 3), which had operated for different periods before the laboratory tests presented in this work. The reported values refer to the stand-alone configuration.

Table 3.1: Performance evaluation of PMUs through the TVE index

DUT	**Maximum Voltage TVE** [%]		
	Phase A	**Phase B**	**Phase C**
PMU 1	0.16	0.16	0.16
PMU 2	0.14	0.14	0.13
PMU 3	0.16	0.16	0.16

The results confirm the compliance of all the PMUs, as the TVE % values are lower than 1 % for all phases, exhibiting comparable magnitudes. The reported values account only for the contribution of the PMUs in terms of magnitude error, since the characterization of the calibrator output signal by means of the 8 1/2-digit multimeter was performed prior to all evaluations on the PMU measurements. The ME introduced by the calibrator were compensated on the three voltage phases following the evaluation of the statistical mean of the measurements provided by the multimeter. This procedure was carried out in two different configurations: with no instrumental load on the calibrator, meaning that the PMUs were disconnected, and with the instrumental load applied. The analysis of the multimeter measurements revealed similar results between the two conditions. During the no-load test, the calibrator exhibited magnitude error offsets of -10.8 ppm, -228.5 ppm, and 160.9 ppm for phases A, B, and C, respectively, and -17.4 ppm, -233.2 ppm, and 157.3 ppm during the load test. Given the similarity of the results, the measurements obtained under load conditions were adopted for the compensation procedure, as they represent the most realistic operating laboratory configuration.

The results of the analysis are reported in Table 3.2 in terms of the mean and standard deviation of the errors for the three PMUs. As can be observed, the experimental uncertainty associated with the estimated offsets is below 2 ppm, expressed as the standard deviation of the observations, and can be attributed to both the multimeter and the calibrator. Conversely, the dispersion of the PMU magnitude measurements is approximately ten times higher than that of the multimeter, allowing the calibrator errors to be modeled as offsets from the PMU perspective and therefore compensated as systematic errors.

Table 3.2: Statistical characterization of the calibrator generation errors and comparison with the PMU MEs

Mean and Standard Deviation Values in ppm						
DUT	**Phase A**		**Phase B**		**Phase C**	
	μ	σ	μ	σ	μ	σ
Calibrator	-17.4	1.5	-233.2	1.5	157.3	1.8
PMU 1	-699.2	21.9	-1118.6	19.3	-459.8	19.0
PMU 2	-759.3	19.6	-949.1	20.0	-618.4	17.4
PMU 3	-952.5	18.0	-1358.5	19.6	-780.3	18.3

3.3.2 Autocorrelation analysis

In the following step, the possible presence of deterministic mechanisms and correlations within the data was assessed. This was carried out using the ACF,

a tool capable of quantifying the degree of correlation of a sequence with time-shifted versions of itself, allowing the identification of any periodicities or trends that violate the assumption of statistical independence required for the construction of valid models. High autocorrelation values at specific lags may indicate the presence of deterministic mechanisms or systematic components.

Figures 3.4 and 3.5 show representative results of the analysis for the MEs and PEs, respectively. In particular, the ACFs of the data related to phase C of PMU 1 are reported. Equivalent results were obtained in all other cases, therefore the considerations discussed here can be regarded as generally valid for all the PMUs under test.

From Figure 3.4, a desirable behavior for statistical analysis can be observed,

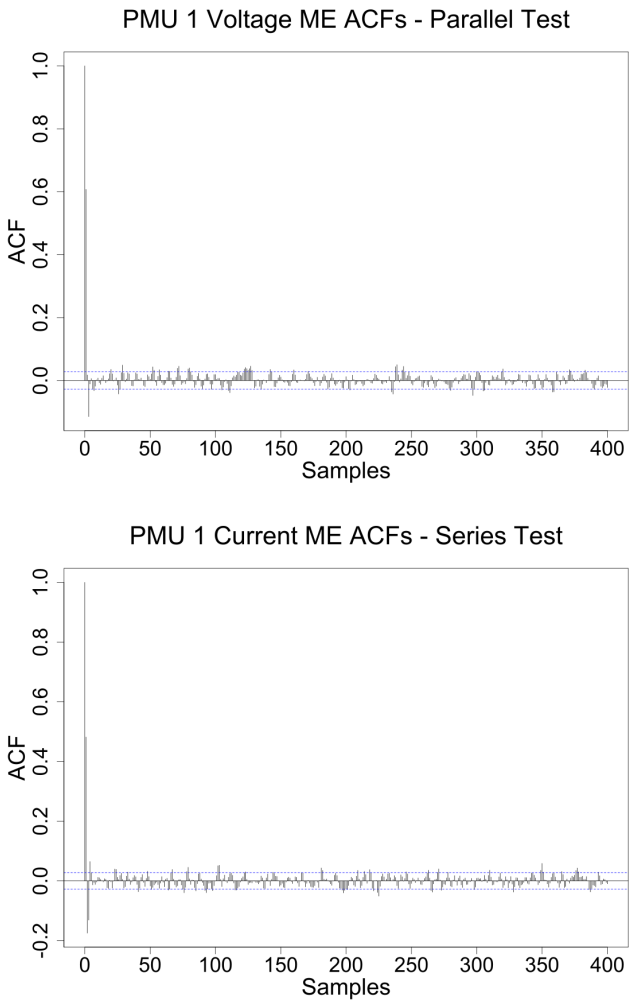

Figure 3.4: PMUs 1 voltage and current ME ACFs, parallel-series test.

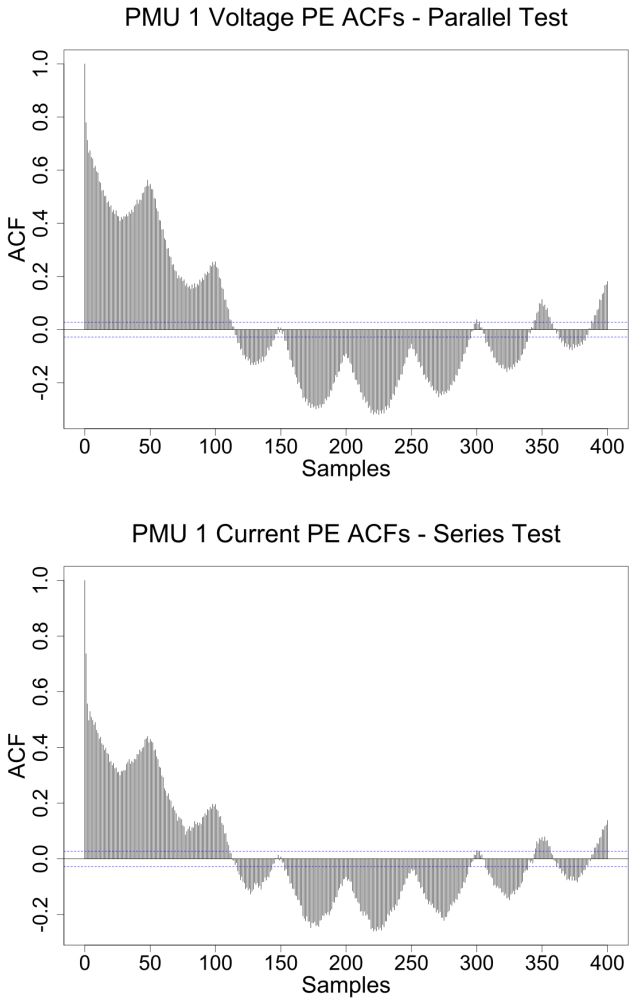

Figure 3.5: PMUs 1 voltage and current PE ACFs, parallel-series test.

evidenced by the rapid drop of the ACF values immediately to the right of the origin. This holds true for both voltage and current errors and indicates a strong decorrelation among the ME data, which reflects excellent stationarity of the acquisition process. In other words, adjacent samples behave independently, and even more so at larger lags, thus confirming the statistical significance and reliability of the dataset under analysis.

Conversely, Figure 3.5 highlights the different nature of the PEs, for which the same conclusion cannot be drawn. In this case, the ACF values do not exhibit a rapid decay as the lag increases; instead, local maxima appear at lags of 50 and 100. This indicates the presence of correlation peaks between samples separated by those intervals, revealing a deterministic behavior. As discussed

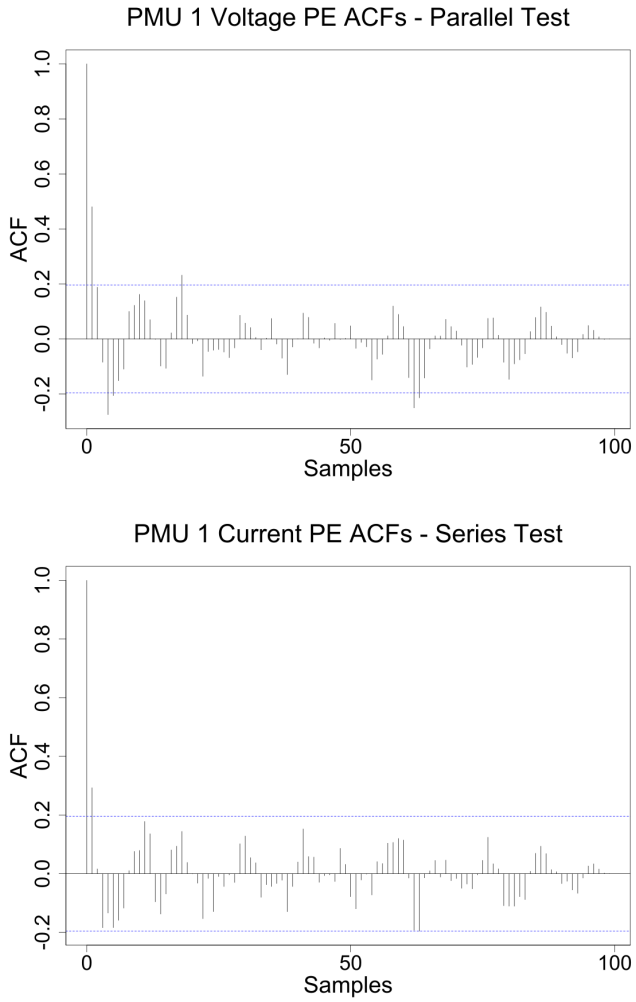

Figure 3.6: PMUs 1 voltage and current PE ACFs after data decimation, parallel-series test.

also in [70], this outcome is not unexpected, since the PE is mainly affected by the synchronization process, which typically performs clock corrections every second, corresponding to 50 samples at 50 fps.

Since, in a black-box configuration, it is not possible to unambiguously determine which device is the source of such determinism, whether the PMU itself or the calibrator, the decimation strategy was adopted to mitigate this effect and enhance the statistical significance of the data. Figure 3.6 shows the ACFs of the PE after decimation, which was performed using a factor equal to the synchronization update frequency, that is 50 samples. The two plots demonstrate the successful outcome of the decimation process, as they reveal a clear decrease

in the autocorrelation values, indicating that the data samples are more weakly correlated and therefore more suitable for statistical analysis. This procedure was applied to all the PE datasets, which exhibited similar behaviors in their ACFs.

3.3.3 Quantitative assessment of normality

Following the autocorrelation analysis and the subsequent data decimation, a quantitative assessment of data normality was performed through significance tests. Tables 3.3 and 3.4 report the results of the Gaussianity analysis on voltage and current measurement errors using the SW test, considering the parallel and series setups, respectively. The stand-alone configuration yielded similar SW responses and is therefore omitted for brevity. The tests were carried out on the MEs and PEs of each phase, considering four dataset sizes from 100 to 3000 samples. Using different dataset lengths allowed assessing device behavior over various time intervals and achieving a broader characterization for multiple application contexts.

The results confirm that the Gaussianity assumption holds for the MEs of both voltage and current measurements. The behavior of the PEs is different for each PMU examined: in particular, it can be seen that PMU 3 allows the Gaussianity assumption to be considered valid for all the data sets considered, but this is not always the case for PMU 1 and PMU 2. As it can be seen from the tables, the voltage (Table 3.3) and current (Table 3.4) tests provide similar results: PMU 1 can be regarded as Gaussian from the 1000-value data set down,

Table 3.3: SW test results for voltage parallel test

DUT	**Sample Size**	**p-value from SW Test**					
		MEs			**PEs**		
		Ph. A	**Ph. B**	**Ph. C**	**Ph. A**	**Ph. B**	**Ph. C**
PMU 1	**3000**	0.98	0.99	0.98	0.00	0.00	0.00
	1000	0.99	0.98	1.00	0.79	0.13	0.00
	500	0.99	1.00	1.00	0.98	0.94	0.91
	100	1.00	1.00	1.00	1.00	1.00	1.00
PMU 2	**3000**	1.00	0.98	0.98	0.00	0.00	0.00
	1000	0.99	0.99	1.00	0.00	0.00	0.00
	500	0.99	1.00	0.99	0.01	0.04	0.02
	100	1.00	1.00	1.00	0.93	0.98	0.99
PMU 3	**3000**	0.99	0.99	0.98	0.27	0.86	0.95
	1000	1.00	0.99	0.98	1.00	0.99	0.99
	500	1.00	0.99	1.00	1.00	1.00	0.97
	100	1.00	1.00	1.00	1.00	1.00	1.00

Table 3.4: SW test results for current series test

DUT	Sample Size	p-value from SW Test					
		MEs			PEs		
		Ph. A	Ph. B	Ph. C	Ph. A	Ph. B	Ph. C
PMU 1	3000	1.00	0.99	0.98	0.05	0.00	0.00
	1000	0.99	1.00	1.00	0.89	0.49	0.48
	500	1.00	0.99	1.00	0.96	1.00	0.97
	100	1.00	1.00	1.00	1.00	1.00	1.00
PMU 2	3000	0.90	0.94	0.97	0.00	0.00	0.00
	1000	0.99	0.99	0.99	0.00	0.05	0.01
	500	0.99	1.00	1.00	0.18	0.42	0.37
	100	1.00	1.00	1.00	1.00	1.00	1.00
PMU 3	3000	0.63	0.99	1.00	0.89	0.84	0.87
	1000	0.97	0.99	0.98	1.00	0.98	0.97
	500	1.00	1.00	1.00	0.99	1.00	1.00
	100	1.00	1.00	1.00	1.00	1.00	1.00

except for the voltage phase C case; in PMU 2 the Gaussianity assumption can only be considered valid for small data sizes (100 for voltage, 500 for current), whereas in PMU 3 the normality hypothesis is not rejected in all cases.

The SW test results indicate that a Gaussian model can always be adopted to describe the MEs, whereas, when PEs are considered, the PMUs from the same manufacturer may exhibit different behaviors. The assumption of Gaussianity can be regarded as rigorously valid only for small dataset sizes; however, this does not represent a critical limitation for PMU error modeling. This aspect can be better understood through a visual inspection of the datasets, which helps clarify the statistical behavior of the errors.

3.3.4 Graphical analysis of PMU error distributions

To complete the discussion, this section presents a visual inspection analysis of the data provided by the PMUs. Since the results obtained for the three phases are overall equivalent, the statistical distributions discussed herein refer exclusively to phase C; nevertheless, similar considerations can also be extended to the other phases. The analysis focuses on data sets consisting of 1000 samples, considering only those acquired from the parallel–series configuration. The graphical inspection is supported by Probability Density Functions (PDFs) and Q–Q plots, which serve as visual tools to assess the adherence of measurement errors to the Gaussian model and to highlight possible deviations from normality. In the following graphical representations, systematic errors are compensated to emphasize the comparison among the random error components of the devices.

Figure 3.7 shows the voltage and current ME PDFs of all PMUs. The observed distributions display smooth, bell–shaped profiles, confirming the Gaussianity hypothesis established through the SW tests. This outcome confirms that, under steady–state operating conditions, the random component of the PMU measurement process can be effectively modeled through a normal distribution.

Notably, the variation range associated with voltage measurement errors is approximately half that observed for current measurements, highlighting the higher stability of the voltage channels. This difference is consistent with the higher sensitivity of current measurement chains to noise sources. The Gaussian behavior is further evidenced by the Q–Q plot results of voltage and current

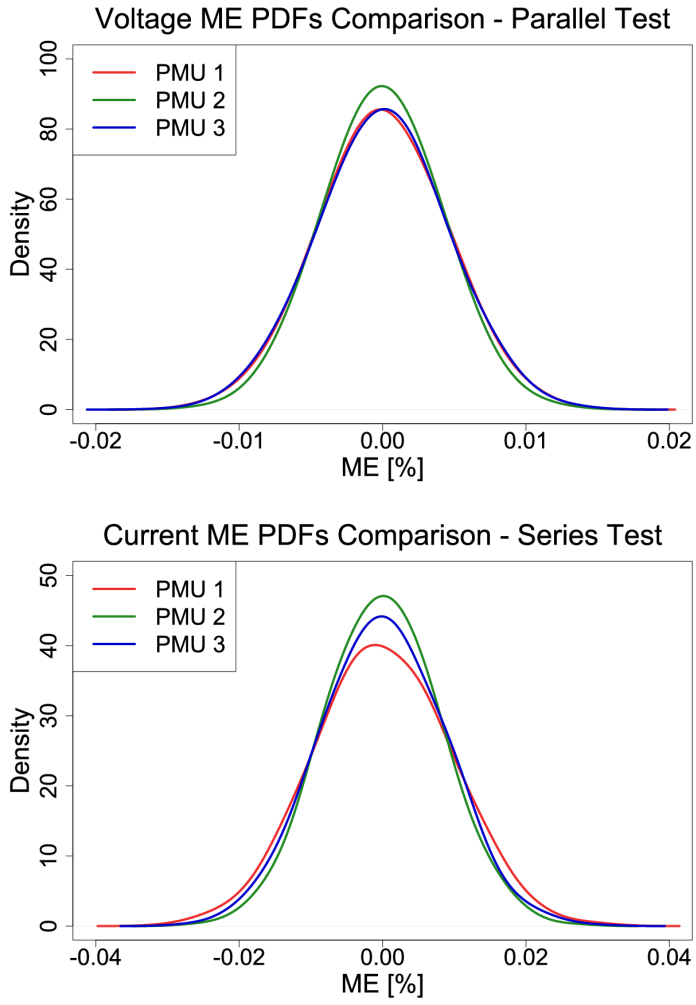

Figure 3.7: Zero-mean voltage and current ME PDFs, parallel-series test.

MEs, shown in Figure 3.8. These plots exhibit an excellent agreement between the empirical error distributions and the theoretical normal distribution, which remains consistent across the entire variation range, extending beyond 3σ. The alignment of the experimental data with the theoretical reference line confirms that the random fluctuations of both voltage and current estimates follow the expected probabilistic trend, with negligible deviations even in the distribution tails. This finding strengthens the reliability of the previously presented quantitative analysis based on significance tests.

Figure 3.9 shows the voltage and current PE PDFs, again focusing only on the random error component. In both cases, the plots of PMUs 1 and 3 are almost overlapped, whereas PMU 2 exhibits a clearly different behavior, with a

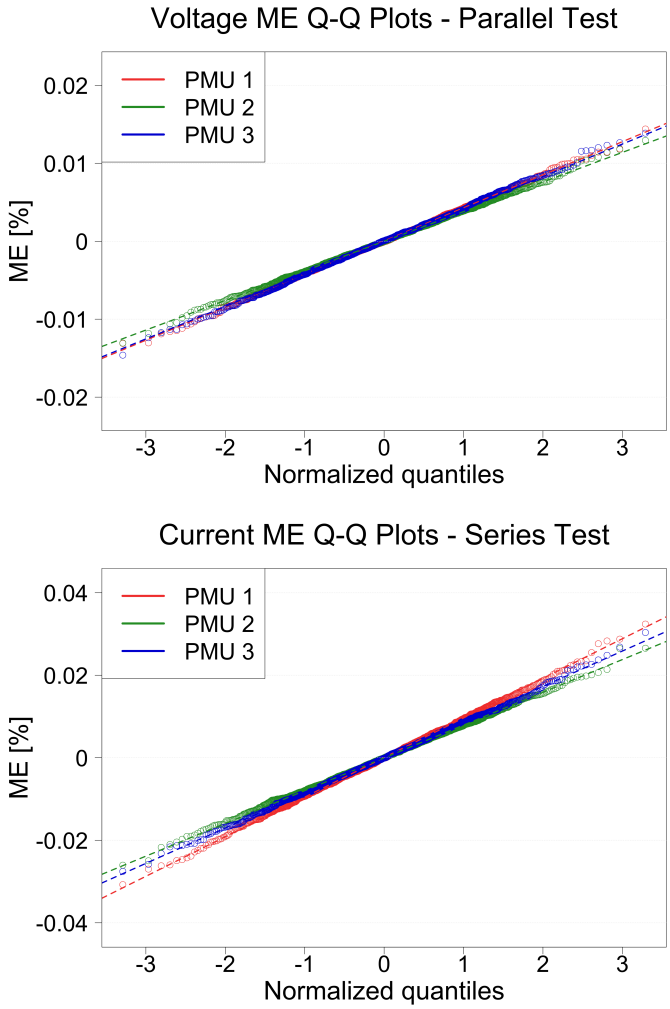

Figure 3.8: Zero-mean voltage and current ME Q-Q plots, parallel-series test.

distribution that significantly deviates from the others. To support the analysis, markers corresponding to $\pm 2\sigma$ have been added to the PDFs, marking the boundaries containing about 95 % of the values. This range is widest for PMU 2, where the normal distribution fits worst, and narrower for PMU 1 and PMU 3, where the Gaussian model proves more suitable. This suggests that data normality tends to deteriorate when random error contributions increase, possibly due to longer uptime or network events affecting PMU operation, while it strengthens as variability decreases. Once again, the Q–Q plots in Figure 3.10 provide a complementary view, confirming the larger deviation of PMU 2 from the theo-

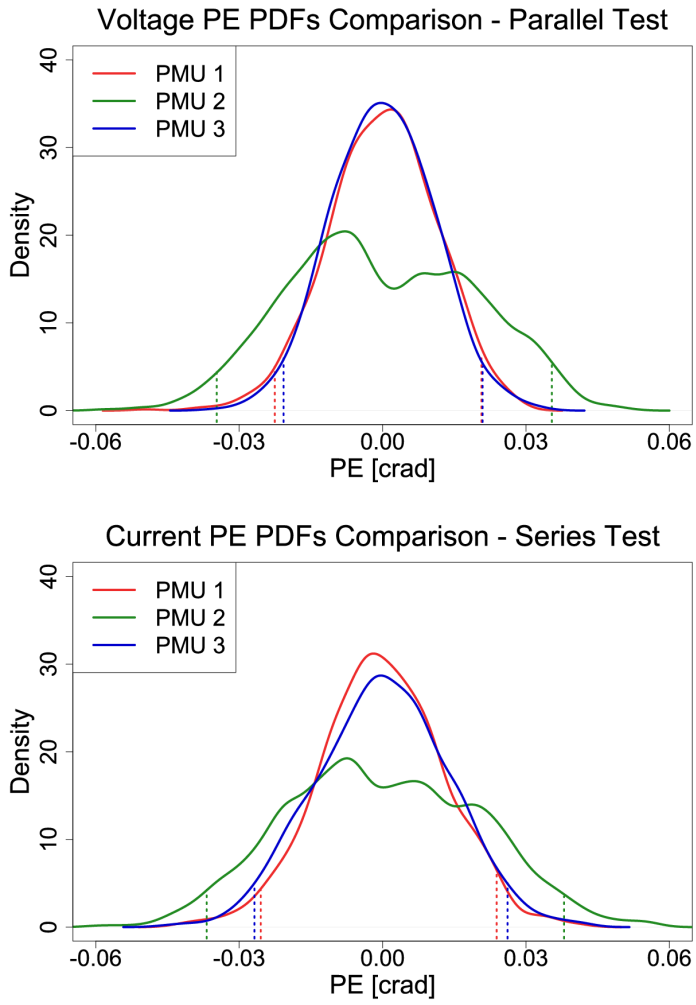

Figure 3.9: Zero-mean voltage and current PE PDFs, parallel-series test. Dashed vertical lines enclose the portion of the distribution containing 95 % of data.

retical normal distribution from approximately $\pm\sigma$ onward, and a greater overall variability, as indicated by the steeper slope of the theoretical line.

To complement these analyses, it is nonetheless meaningful to evaluate the data coverage within the $\pm\sigma$, $\pm 2\sigma$, and $\pm 3\sigma$ intervals. Some results of this evaluation are reported in Table 3.5, which summarizes the outcomes of the characterization just described. The examination of the PDFs and the corresponding coverage percentages confirms that these intervals consistently include the majority of the data across all devices under test. The limited deviations observed among different PMUs further corroborate the adequacy of the Gaussian model, even when perfect normality is not achieved.

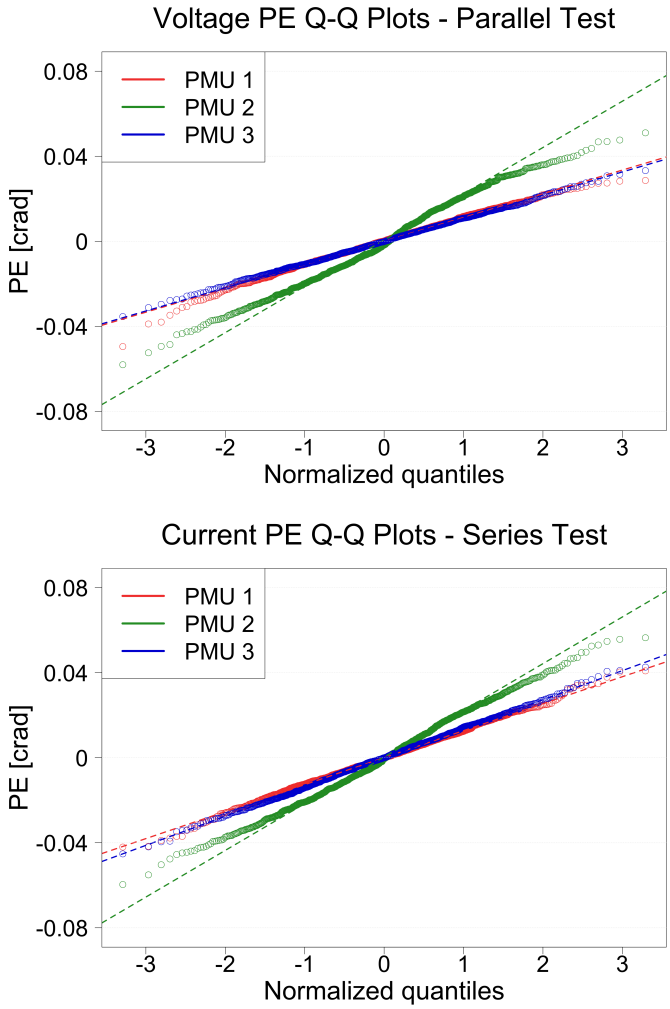

Figure 3.10: Zero-mean voltage and current PE Q-Q plots, parallel-series test.

Table 3.5: Confidence Levels Depending on Coverage Factors in Samples Distribution for PEs

DUT	% of Samples Included					
	Voltage Parallel Test			Current Series Test		
	$\pm\sigma$	$\pm2\sigma$	$\pm3\sigma$	$\pm\sigma$	$\pm2\sigma$	$\pm3\sigma$
PMU 1	68.4	95.6	99.6	70.4	96.0	99.5
PMU 2	64.7	97.5	99.9	65.0	96.4	100.0
PMU 3	66.8	95.3	99.8	66.7	95.7	99.7

3.3.5 Further analysis on current measurements under varying load conditions

To provide a more comprehensive overview of the statistical modeling of MEs and PEs in PMUs, this section presents the results of the statistical analysis performed at different current levels, specifically 0.5 A, 1.0 A, 2.5 A, and 5.0 A, as reported in [60]. Offering such an overview is particularly relevant because, unlike voltage, whose level is fixed by the nominal ratings at the ITs level, the current depends on the load conditions of the electrical grid, which can vary significantly. Therefore, a statistical characterization of PMUs errors at different current levels provides valuable insight into their behavior under diverse operating conditions. In this case, the results refer to two different PMU models from two different manufacturers (PMUs 4 and 5), distinct from those analyzed previously.

The statistical analysis followed the same procedure described in Section 3.2.2. After the preliminary steps devoted to performance assessment through the evaluation of the TVE index and data filtering by means of autocorrelation analysis, significance tests were performed using the SW statistical tool. The focus here is on the statistical results obtained at different current levels. Since the preliminary analyses led to conclusions similar to those drawn from the previous tests, the discussion proceeds directly to the presentation of the Gaussianity test results, reported in Tables 3.6 and 3.7 for PMUs 4 and 5, respectively. The results show a consistent behavior between the two PMUs, comparable with that observed in the previous tests for the MEs, whereas a markedly different statistical behavior is observed for the PEs.

For PMU 4, the p-values are above the 0.05 significance threshold for all test conditions, clearly indicating that the Gaussian model cannot be rejected. This outcome holds for both MEs and PEs, across all phases and current levels. Only minor deviations are observed for the PEs at 2.5 A and 5.0 A when large sample sizes ($n = 3000$) are considered, but these deviations disappear as sample

Table 3.6: SW test results for PMU 4

Test	Sample Size	p-value from SW Test					
		MEs			PEs		
		Ph. A	Ph. B	Ph. C	Ph. A	Ph. B	Ph. C
0.5 A	**3000**	0.98	1.00	1.00	1.00	1.00	0.98
	1000	1.00	1.00	1.00	1.00	1.00	1.00
	500	1.00	1.00	1.00	1.00	1.00	1.00
	100	1.00	1.00	1.00	1.00	1.00	1.00
1.0 A	**3000**	1.00	0.99	1.00	0.98	0.91	0.87
	1000	1.00	1.00	1.00	1.00	1.00	1.00
	500	1.00	1.00	1.00	1.00	1.00	1.00
	100	1.00	1.00	1.00	1.00	1.00	1.00
2.5 A	**3000**	0.74	1.00	1.00	0.19	0.32	0.11
	1000	1.00	1.00	1.00	0.43	0.46	0.42
	500	1.00	1.00	1.00	0.92	0.87	0.63
	100	1.00	1.00	1.00	1.00	0.98	1.00
5.0 A	**3000**	0.99	0.99	0.99	0.29	0.29	0.13
	1000	1.00	1.00	0.99	0.75	0.51	0.39
	500	0.94	1.00	1.00	0.37	0.32	0.34
	100	1.00	1.00	1.00	0.90	0.91	0.89

Table 3.7: SW test results for PMU 5

Test	Sample Size	p-value from SW Test					
		MEs			PEs		
		Ph. A	Ph. B	Ph. C	Ph. A	Ph. B	Ph. C
0.5 A	**3000**	1.00	0.99	0.99	0.00	0.00	0.00
	1000	1.00	1.00	1.00	0.08	0.00	0.06
	500	1.00	1.00	1.00	0.23	0.15	0.25
	100	1.00	1.00	1.00	0.99	1.00	1.00
1.0 A	**3000**	0.52	0.99	0.97	0.00	0.00	0.00
	1000	0.99	1.00	1.00	0.00	0.00	0.00
	500	0.99	1.00	1.00	0.00	0.00	0.00
	100	1.00	1.00	1.00	0.08	0.09	0.07
2.5 A	**3000**	1.00	0.96	0.99	0.00	0.00	0.00
	1000	1.00	1.00	1.00	0.00	0.00	0.00
	500	1.00	1.00	1.00	0.00	0.00	0.00
	100	1.00	1.00	1.00	0.00	0.00	0.00
5.0 A	**3000**	0.97	0.94	0.93	0.00	0.00	0.00
	1000	0.99	0.98	0.99	0.00	0.00	0.00
	500	1.00	1.00	1.00	0.00	0.00	0.00
	100	1.00	1.00	1.00	0.00	0.00	0.00

sizes decrease. This confirms that, for this device, both types of errors can be effectively modeled by normal distributions, and that the data exhibit stationary and homogeneous statistical behavior once deterministic components have been mitigated through the proposed preprocessing.

Conversely, PMU 5 exhibits a distinct behavior. While the MEs generally comply with the Gaussian assumption, the PEs yield p-values close to zero in almost all tests, regardless of the current level or the number of samples considered. Only when the sample size is considerably reduced ($n = 100$) the PEs approach Gaussianity for low current levels (≤ 1 A). The persistently low p-values indicate that the null hypothesis of normality must be rejected in most cases, revealing a systematic deviation from the Gaussian model. Such behavior is consistent with the previous considerations on synchronization and becomes even more pronounced in this case.

Once again, it is useful to examine the obtained distributions graphically to highlight additional shades in their behavior. To this end, and to keep the discussion concise, a selection of Q–Q plots is presented for sample sizes of 1000 samples. Figure 3.11 shows the Q–Q plots of the MEs for current levels of 0.5 A and 5.0 A, representing the two extreme cases. Consistently with the robust results obtained for all sample sizes, in both cases the empirical distribution closely follows the theoretical one across the entire displayed range. However, it is worth noting that the error variation range decreases for both PMUs as the current increases, as evident from the lower plot, which displays smaller slopes. This behavior can be attributed to the higher proximity of the current level to the device FSR.

Figure 3.12 shows the Q–Q plots of the PEs for the same current levels, 0.5 A and 5.0 A. Once again, the results confirm the outcomes of the quantitative analysis performed through the SW test, which indicated an unquestionable Gaussianity for PMU 4 also in the case of PEs, while the same hypothesis was completely rejected for PMU 5. In this regard, it is worth examining the experimental data trend of PMU 5 PEs with respect to the theoretical distribution. s shown, the 0.5 A case confirms the Gaussian behavior of the error distribution, whereas the 5.0 A case displays a step-like pattern, revealing the presence of quantization effects. This behavior suggests the presence of a deterministic mechanism intrinsic to the device operation, not attributable to the calibrator data, as confirmed by its absence in the trends of PMU 4. Once again, this behavior is most likely attributable to the device synchronization system, whose clock correction management can affect the distribution of the PEs differently from the other PMUs. This case certainly deserves further investigation, which lies beyond the scope of this thesis, aimed instead at identifying, as reliably as possible, the cause of the phenomenon. Should synchronization be confirmed

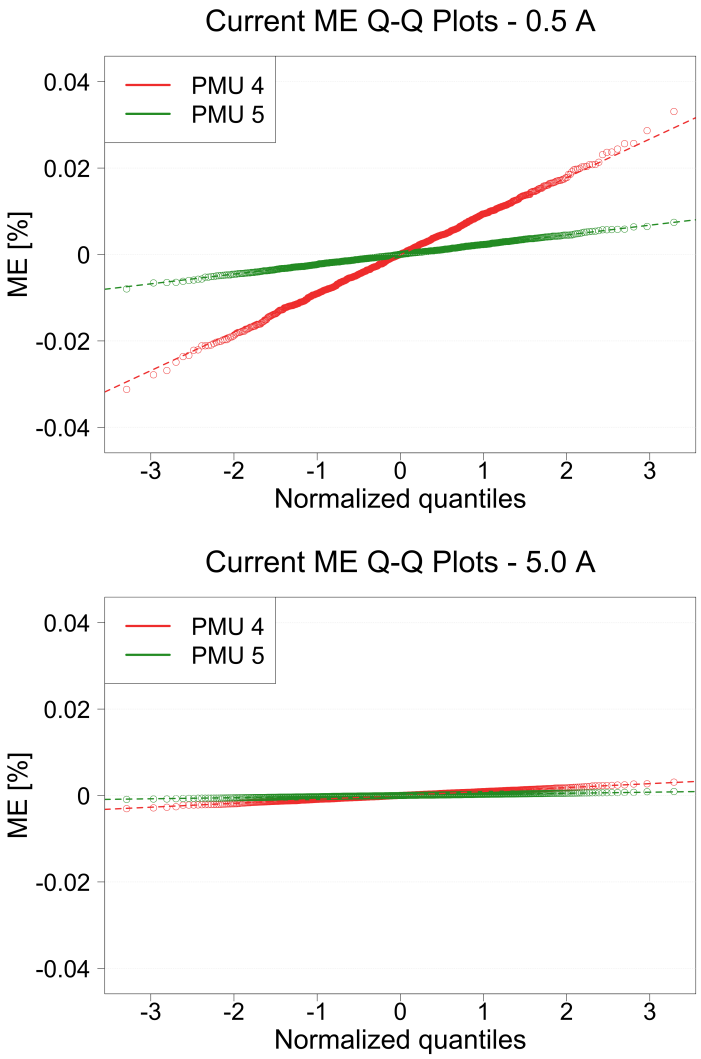

Figure 3.11: Zero-mean current ME Q-Q plots for PMUs 4 and 5 in the 0.5 A and 5.0 A tests.

as the source, it should be incorporated into the statistical model, as it would represent an intrinsic characteristic in the PMU operation. This finding further emphasizes the importance of individually characterizing each device before assuming a universal statistical model for PMU error modeling and uncertainty propagation.

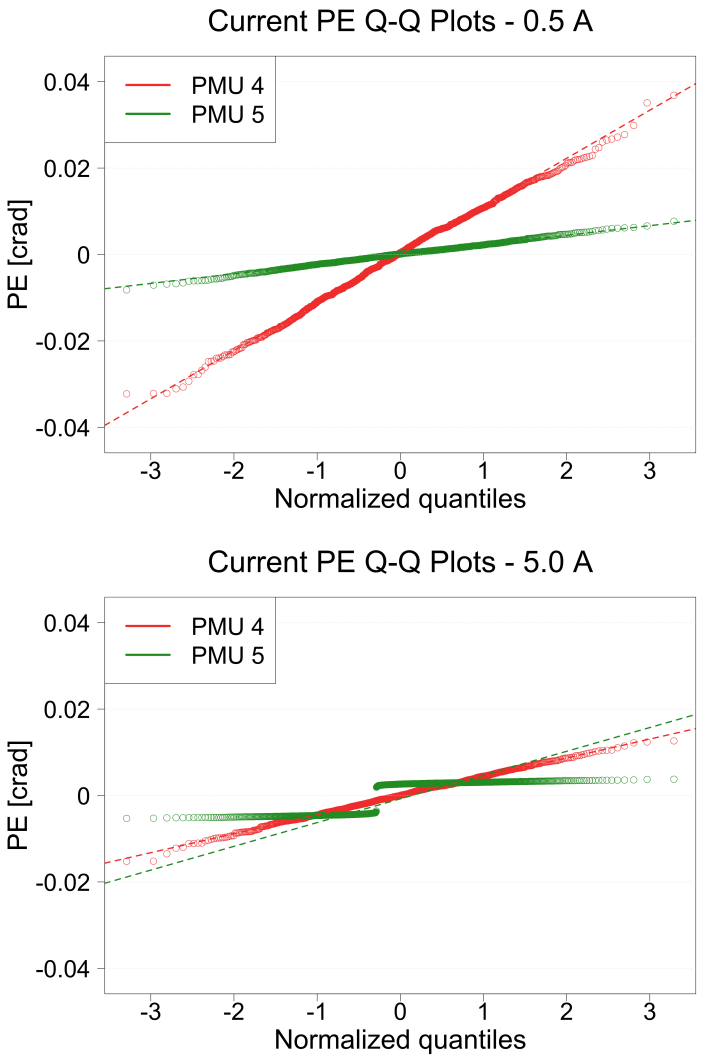

Figure 3.12: Zero-mean current PE Q-Q plots for PMUs 4 and 5 in the 0.5 A and 5.0 A tests.

3.4 Proposed statistical model for PMU errors

The results of the statistical analysis consistently demonstrated that the Gaussian model represents a valid and effective assumption for the MEs, providing a compact yet accurate description of their statistical behavior. This outcome aligns with expectations: once external influencing factors capable of introducing trends or correlations in the data are thoroughly identified and removed, the Gaussian hypothesis naturally emerges as the most suitable choice.

While for the MEs the analysis has dispelled any uncertainty, this is not

always the case for the PEs. The latter exhibit a more complex behavior, being influenced by synchronization mechanisms that introduce deterministic components and potential deviations from ideal Gaussianity. Among the analyzed cases, the one concerning PMU 5 most clearly supports this observation. Unlike the others, it displays a pronounced non-Gaussian component in its PEs, which becomes more evident at higher current levels. This finding underscores the importance of performing an individual device characterization under different operating conditions, particularly when dealing with current measurements.

In conclusion, it is worth providing a final application-oriented insight into the proposed approach. From a broader perspective, the error models derived through the presented methodology constitute the foundation for generating synthetic data in simulation environments and digital twins of power systems. This makes it possible to develop high-level applications such as state estimation, control algorithms, and reliability assessment, with error behavior that faithfully reproduces that of real measurement devices. Ultimately, the characterization process described herein contributes to establishing a reliable metrological basis for the modeling of PMUs, ensuring that future studies and simulation frameworks can rely on statistically grounded and experimentally validated uncertainty models.

Chapter 4

White Rabbit-based synchronization architectures for power system applications

Synchronization represents a fundamental element in distributed monitoring systems of the electrical grid, as it enables the collection of measurements from geographically distant points while preserving their temporal correlation. This capability is particularly important for the monitoring and control of wide-area power systems, where decision-making relies on data acquired from diverse and spatially separated locations. For this reason, it is essential to ensure an adequate level of synchronization, thereby guaranteeing reliable time-stamping of measurement data. Time synchronization affects not only the accuracy of timestamping but also that of phase-angle measurements, whose accuracy strongly depends on the stability of the device's time base and, consequently, on the quality of synchronization itself.

Within this framework, and among the multitude of available synchronization protocols, this chapter explores the applicability of the White Rabbit (WR) protocol to the monitoring of electrical systems. Building upon the work presented in [82], this chapter proposes WR-based synchronization distribution architectures designed to enhance timing accuracy compared to conventional solutions. A key enhancement here introduced is an extended architecture fully implemented on Field Programmable Gate Array (FPGA) technology, specifically conceived to maximize synchronization determinism. The architecture was designed and developed at the Instrumentation and Measurement Laboratory of the University of Cagliari, where a working prototype has also been implemented. In this perspective, the chapter concentrates on WR-based time

dissemination architectures, examining how design choices on time reference, distribution path, and endpoint integration affect timing performance. The discussion reflects a gradual consolidation of architectural awareness, moving from real-time controller solutions, still dependent on an operating system despite their improved determinism, to fully FPGA-based hardware implementations. By pushing synchronization management into dedicated hardware, the proposed architecture achieves a higher level of timing accuracy and stability, making it suitable for demanding power system applications.

4.1 White Rabbit protocol

The WR protocol is an advanced synchronization technology developed to meet the growing demand for ultra-reliable, sub-nanosecond accuracy in time-sensitive applications. It was originally conceived at the European Organization for Nuclear Research (CERN) to synchronize processes within the particle accelerator complex [20]. WR has since been standardized as a High-Accuracy (HA) profile for the latest version of the Precision Time Protocol (PTP) in Annex M of IEEE Standard 1588 [83], which has also been adopted by International Electrotechnical Commission as IEC/IEEE Standard 61588 [23].

This protocol is designed to operate across a wide range of network topologies, from simple point-to-point connections to complex tree and mesh configurations. Synchronization is distributed according to a master and slave hierarchy, propagating from the top of the hierarchy, the WR master, down to the other WR switches and finally to the peripheral nodes. WR networks can include thousands of devices located several kilometers apart and interconnected through existing Ethernet infrastructure, which makes the protocol suitable for a broad spectrum of applications. Furthermore, the WR protocol is inherently scalable, allowing network expansion and the integration of a large number of devices without compromising timing accuracy. This is achieved through precise estimation and compensation of the delay at each node [84].

The WR protocol is built upon a set of standards that define both the physical and timing layers of the communication system:

- IEEE 802.3, which specifies the Ethernet physical layer [85];
- Sync Ethernet (SyncE), which enables the transfer of clock signals over Ethernet links [86];
- IEEE 1588, which defines the PTP packet-based synchronization protocol from which the WR protocol is derived [83].

The combination of these standards allows the WR protocol to achieve outstanding performance, depending on the communication medium. The protocol furthermore incorporates a key technique known as Precise Phase Measurement, which accurately determines the phase offset between master and slave clocks using a digital Dual Mixer Time Difference (DMTD) circuit [20]. This capability enables sub-nanosecond synchronization through precise compensation of the link delay at the physical layer. The best performance is achieved through the use of fiber optic links instead of conventional Ethernet over copper, which offer greater immunity to electromagnetic interference and higher bandwidth. When fiber optics are employed, the synchronization accuracy, expressed as the time deviation of each node with respect to the Coordinated Universal Time (UTC) reference, reaches the sub-nanosecond range with picosecond-level precision [20]. Conversely, when using copper, the achievable accuracy is approximately 30 ns, nearly two orders of magnitude lower than with fiber [87]. In addition to the advantages of using optical fiber, further improvements stem from the adoption of the SyncE protocol, which provides a clock accuracy of 4.6 ppm with respect to the reference time source. This represents a substantial enhancement over the asynchronous Ethernet limit, where a free-running clock typically exhibits an accuracy of 100 ppm [88].

This innovative technology provides a suitable and efficient substitute or enhancement to Global Positioning System (GPS), especially in scenarios where sky access is limited, such as in urban environments, where there is existing telecommunication infrastructure, and where the typical distance between nodes is below 10 km [89], even though WR applications extending up to 500 km are currently being developed [90]. Moreover, WR synchronization is more stable and less geographically dependent than GPS.

4.1.1 Integration in power systems

The use of WR in power systems, in addition to providing remarkable accuracy, offers a significant advantage at the substation level by enabling the transition from local synchronization, as in the case of GPS, to a single wide-area synchronization source that can be shared and retransmitted across multiple substations. This capability is particularly relevant when considering that time synchronization accuracy requirements in power systems vary depending on the specific application. As shown in Table 4.1, the IEC Standard 61850-5:2013 [21] defines seven accuracy classes, ranging from Class T5, intended for phasor and distributed measurement applications with microsecond-level accuracy, to Class TL (Time Synchronization Low), intended for non–time-critical monitoring applications with accuracy exceeding one second.

Table 4.1: Time synchronization accuracy classes for power system applications defined in IEC Standard 61850-5:2013

Class	**Synchronization Accuracy**	**Application**
A	1 µs	Phasor and distributed measurements
B	100 µs	Automated fault recording
C	1 ms	Time tagging of fast/transient events
D	10 ms	Power quality monitoring
E	100 ms	Slow event monitoring and logging
F	> 1 s	Other no time-critical monitoring applications

The specified classes may not fully meet the stringent requirements of advanced time-sensitive applications, since even the synchronization accuracy defined for Class T5 can become inadequate in more demanding scenarios, such as those involving high-order harmonic synchrophasor measurements, where higher accuracy and tighter timing constraints are essential.

Within digital substation communication frameworks based on the IEC 61850 standards, the Rootable GOOSE (R-GOOSE) and Rootable Sampled Value (R-SV) protocols [91] enable the exchange of measurement and control signals between substations through their ability to be encapsulated at higher network layers, for example in Transmission Control Protocol (TCP) or User Datagram Protocol (UDP) data packets. Several studies have investigated the feasibility of sharing measurement and control information between different substations using R-GOOSE and R-SV messages [92]. In this context, time synchronization can also be shared between substations, and the WR protocol represents a strong candidate for wide-area applications, as it enables the synchronization of geographically distant points without compromising time accuracy. One key advantage of relying on a single synchronization source is the elimination of time offsets between devices located in different substations, as well as the prevention of synchronization degradation in a single substation from affecting the ability to accurately correlate data across the entire network. In line with these considerations, the deployment of fiber networks for purposes beyond strictly research activities is rapidly increasing, as demonstrated by the SWITCH [93] and LIFT [94] projects in Switzerland and Italy.

In addition to providing sub-nanosecond synchronization accuracy, WR-based network architectures are designed to ensure reliable delivery of synchronization data even in the presence of potential packet loss. Deterministic timestamping alone does not eliminate the risk of missing or attenuating critical events such as peak shaving. For this reason, WR networks employ dedicated

optical paths, quality of service policies, and redundant topologies to prevent congestion and guarantee seamless failover without performance degradation. Furthermore, the separation of synchronization traffic from measurement data streams minimizes the likelihood that packet loss concurrently impacts both timing and measurement packets [95].

4.2 Implementation of the power-system-oriented White Rabbit architecture

Building on the strengths of the WR protocol, this section explores its use within different architectural configurations designed for time dissemination in power system monitoring networks. Three architectures are discussed, all aimed at distributing the timing information through the WR protocol to synchronize the clock of a device located at the end of the chain, referred to as the WR Slave. The first two architectures [82], developed respectively at the Instrumentation and Measurement Laboratory of the University of Cagliari and at the Federal Swiss Institute of Metrology (METAS), are based on the National Instruments (NI) CompactRIO (cRIO) system and employ, respectively, a GPS receiver and the Fontaine Continue Suisse (FoCS-2) as time sources.

The third architecture represents an advancement over the others, being an evolution of the first one. In this configuration, the cRIO system was replaced by a fully FPGA-based setup, enabling more predictable and consistent control of the synchronization chain. The synchronization accuracy was then evaluated considering the same GPS time source, ensuring a consistent benchmark for performance comparison.

4.2.1 cRIO-based architecture with GPS time source

The first architecture, illustrated in Figure 4.1, was developed at the Instrumentation and Measurement Laboratory of the University of Cagliari. It relies on a Real-Time (RT) cRIO controller and a GPS time reference as its synchronization source.

The first element of the architecture is the Meinberg Lantime M1000 GPS receiver, equipped with a Master Quality Oven Controlled Crystal Oscillator (OCXO-MQ). This device enables the distribution of the synchronization signal to external systems in the form of a Pulse per Second (PPS) pulse, a 10 MHz square wave, or via synchronization packets based on Network Time Protocol (NTP) or PTP protocols. All three signals were used to synchronize the next element in the chain, the WR Switch [96]. This device, manufactured by

SAFRAN, enables the distribution of synchronization to more than one thousand nodes with sub-nanosecond time accuracy through optical fibers using the WR protocol. In this architecture, the NI cRIO 9024 RT controller was selected to interface with the WR network and receive the time synchronization signal distributed over optical fiber, therefore operating as WR Slave. The cRIO technology consists of an embedded industrial controller equipped with a RT processor running the NI Linux RT operating system. These controllers can be coupled with chassis featuring an FPGA, which enables deterministic and high-speed communication with the connected Input/Output (I/O) modules. The cRIO 9024 integrates a processor operating at up to 800 MHz and 512 MB of Dynamic Random Access Memory (DRAM). In this setup, it was paired with the cRIO 9113 chassis, hosting a Virtex-5 LX50 FPGA characterized by a timebase accuracy of 100 ppm and a maximum jitter of 250 ps at 40 MHz.

As shown in the schematic of Figure 4.1, three boards were installed in the

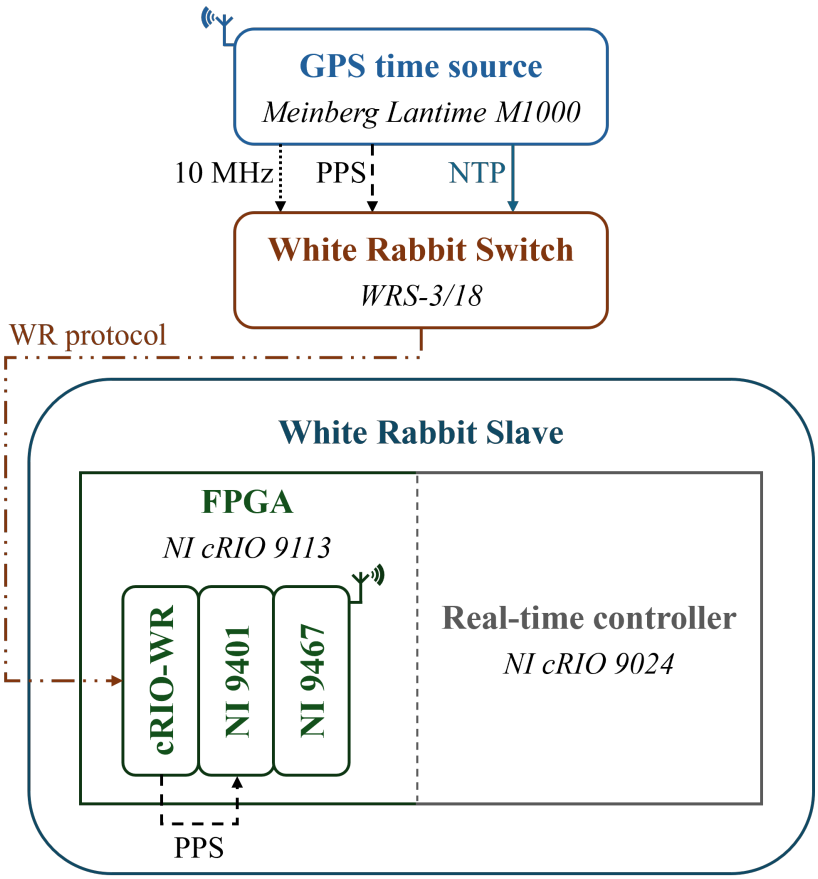

Figure 4.1: The cRIO-based experimental test architecture implemented at the Instrumentation and Measurement laboratory of the University of Cagliari.

cRIO 9113 chassis:

- The NI 9467 is a GPS synchronization module providing PPS accuracy of approximately 100 ns. It was used for preliminary tests carried out in the absence of the WR protocol, during which it supplied the PPS signal to the NI 9401 module. Once the WR system was introduced in the experimental setup, the NI 9467 was replaced by the cRIO-WR module.
- The NI 9401 is a digital I/O interface characterized by a maximum propagation delay of 100 ns.
- The cRIO-WR is a custom module integrating a WR core implemented on a Xilinx Spartan-6 FPGA [97]. It features an Small Form-factor Pluggable (SFP) cage for the fiber-optic transceiver used to transmit and receive the WR protocol, a Universal Serial Bus (USB) connector for user configuration, and a 15-pin D-sub port with programmable I/O.

The cRIO-WR module was configured in slave mode with a point-to-point fiber-optic connection to communicate, through the WR protocol, with the WR Switch operating in grandmaster mode. In addition, the cRIO-WR module was set to generate a PPS signal on its I/O port, which was directly acquired by the NI 9401 module.

4.2.2 cRIO-based architecture with FoCS-2 time source

The second architecture, illustrated in Figure 4.2, was implemented at the Federal Swiss Institute of Metrology (METAS) laboratories in Bern-Wabern and employs a system capable of ensuring traceability to UTC(CH).

The time reference is provided by the FoCS-2, which serves as the primary frequency standard and is ranked among the world's most accurate Caesium atomic clocks. This clock exhibits a drift of only one second over 30 million years, achieving time accuracy in the femtosecond range [98]. The reference generated by the FoCS-2 is distributed through a UTC(CH)-traceable time server, which plays the same role as the Meinberg GPS receiver in the first architecture, providing in output a PPS signal, a 10 MHz clock, and the NTP protocol. These signals are received by the WR Switch, configured again as the grandmaster of the WR network and therefore responsible for distributing synchronization to the subsequent nodes through the WR protocol.

The WR network includes two configurations for the WR Slaves. The first employs a cRIO-WR module that generates a PPS signal, which is sent as input to the NI 9401 digital board, as in the first architecture. The second configuration adopts a higher-performance device, the WR ZEN TP-FL, calibrated at

METAS, which guarantees a worst-case offset of 7 ps with respect to UTC(CH) and likewise generates a PPS signal to be provided to the NI 9401 board.

In this case, the NI 9401 digital board and the cRIO-WR module were hosted by the cRIO 9068, which served as the RT controller. The system is equipped with an ARM Cortex-A9 dual-core processor operating at up to 667 MHz and

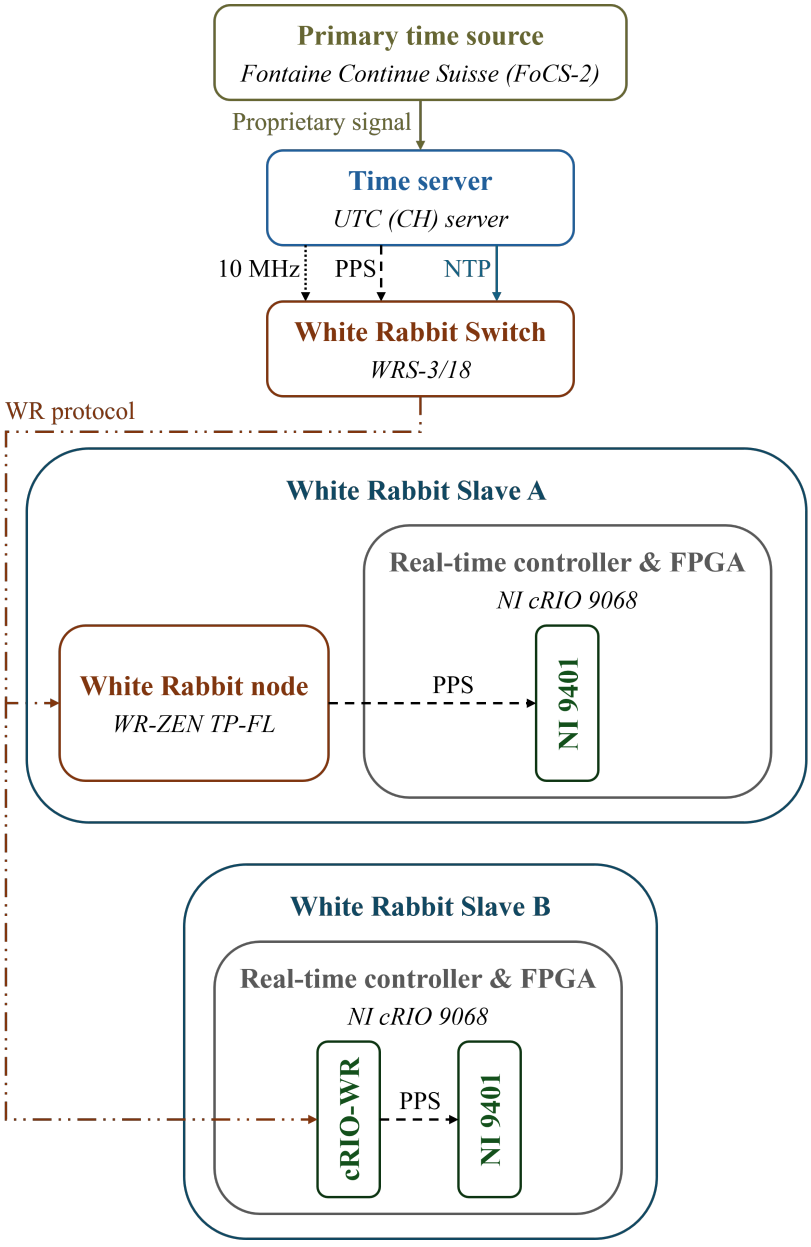

Figure 4.2: Experimental test architecture implemented at the METAS laboratory.

1 GB of Random-Access Memory (RAM). This modular platform also includes a chassis integrating a Xilinx Zynq-7020 System-on-Chip (SOC) featuring a FPGA running at 40 MHz and a RT clock with a guaranteed accuracy of 5 ppm.

4.2.3 Full FPGA-based architecture with GPS time source

Finally, the third architecture, illustrated in Figure 4.3, represents an evolution of the original scheme implemented at the Instrumentation and Measurement Laboratory of the University of Cagliari. The first section of the setup, comprising the Meinberg Lantime M1000 GPS receiver and the WR Switch, remains unchanged and provides the WR signal output through the optical fiber.

The main enhancement was introduced on the WR Slave side, which was completely redesigned as a system entirely implemented on FPGA technology.

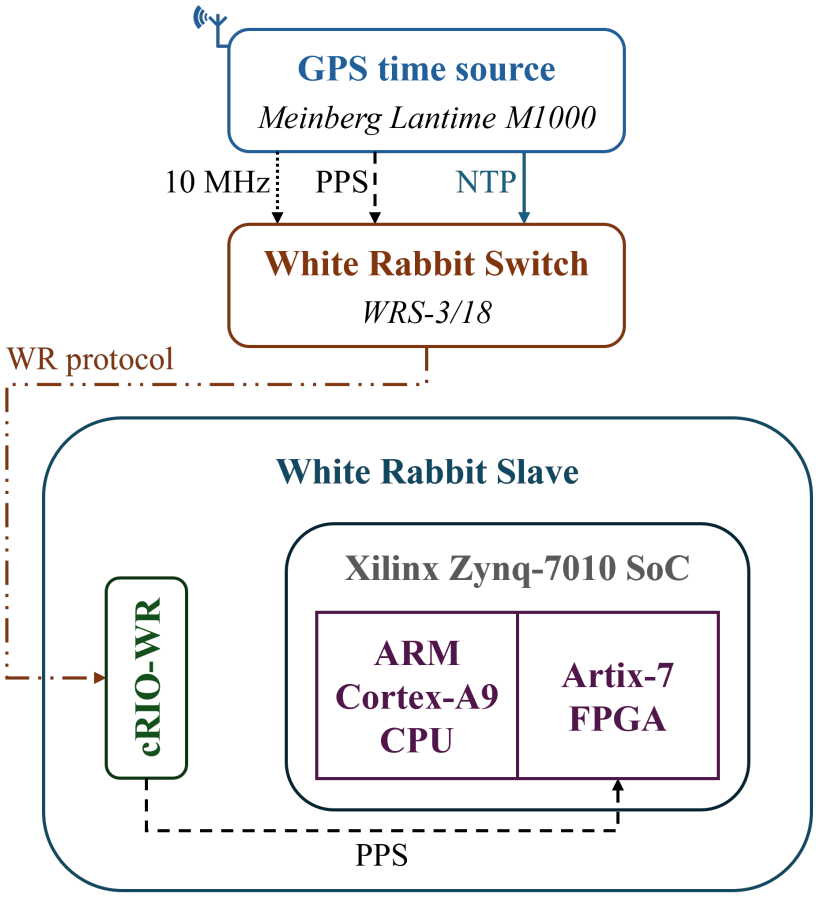

Figure 4.3: The full FPGA-based experimental test architecture implemented at the Instrumentation and Measurement laboratory of the University of Cagliari.

This upgrade aims to mitigate the intrinsic non-deterministic effects arising from the use of the NI 9401 digital board by establishing a direct connection between the PPS synchronization signal and the FPGA clock to be disciplined.

This approach enables the investigation of the performance achievable with a commercial system entirely implemented on FPGA technology. The objective is to enhance the performance achieved by the WR-based architecture shown in Figure 4.1 while maintaining a commercial GPS time source, and to compare it with the results obtained using a reference-grade time source in the architecture of Figure 4.2. To this end, the Xilinx Zynq-7010 SOC, an embedded platform that integrates a real-time ARM Cortex-A9 processor, an Artix-7 FPGA, and both analog and digital I/O was employed. The FPGA, operating with a 40 MHz clock, constitutes the core of the implementation. The digital inputs, directly connected to the FPGA, are used to acquire the PPS signal provided by the cRIO-WR board, which is leveraged to synchronize the internal clock of the FPGA. This configuration, characterized by the presence of a dedicated hardware circuit specifically designed for PPS acquisition and clock synchronization, improves the overall determinism of the system.

4.2.4 Software implementation of the FPGA time synchronization routine

The routine implemented on the cRIO 9024, cRIO 9068, and the Xilinx Zynq-7010 SOC for managing the synchronization signal at the FPGA level is here described. Across all platforms, the internal FPGA clock is disciplined by a LabVIEW-based control application through the FPGA Timekeeper library, which exploits the PPS signal supplied by the three synchronization architectures previously described. Algorithm 2 illustrates the complete synchronization loop implemented on the FPGA, encompassing the detection of the PPS rising edge, timestamp acquisition, offset computation, and correction of the internal time base. All variables and function interfaces are explicitly defined to enable straightforward replication of the logic on comparable platforms.

At each tick of the FPGA clock, occurring every 25 ns given its 40 MHz frequency, the function `DetectRisingEdge` monitors the input PPS signal, which serves as the time reference. As soon as a rising edge is detected, the function `GetFPGATimekeeperTimestamp` records the timestamp of the internal FPGA time base and computes its difference with respect to the nearest full second, storing it as a time offset (steps (i) and (ii) of the algorithm). The computed offset is then used by the function `UpdateFPGATimekeeperClock` to correct the internal time base and then stored in the RT controller log through the function `SaveOffsetRTController` (steps (iii) and (iv)). Finally, the function

`WaitNextTick` ensures the deterministic execution of the synchronization loop by pausing the process until the next clock period (T_{clk}) elapses (step (v)). This mechanism guarantees that monitoring and correction tasks are executed periodically with a fixed timing resolution, synchronized to the FPGA internal clock.

Algorithm 2 PPS-based FPGA clock synchronization

Input: PPS_signal (digital input), FPGA_clock (40 MHz), time-base period T_{clk}
Output: offset_ns, synchronized FPGA_time

```
while system is running do
    if DetectRisingEdge (PPS_signal) then
        i.  Acquire timestamps from both reference and FPGA clock:
            t_PPS ← GetPPSFullSecond ()
            t_FPGA ← GetFPGATimekeeperTimestamp ()
        ii.  Compute time offset between FPGA and PPS rising edge:
             offset ← ComputeOffset (t_FPGA, t_PPS)
        iii.  Apply correction to internal FPGA time-base:
              UpdateFPGATimekeeperClock (δt_offset)
        iv.  Log the measured offset:
             SaveOffsetRTController (δt_offset, t_PPS)
    end
    v.  Wait one FPGA tick before checking input again:
        WaitNextTick (T_clk)
end
```

The same disciplined time base obtained through this synchronization loop can be leveraged in the development of advanced measurement pipelines implemented on the FPGA. Such an approach enables a consistent and traceable temporal reference across the entire signal processing chain, from data acquisition to higher-level functions such as fundamental and harmonic synchrophasor estimation or other time-sensitive applications, thereby enhancing the overall reliability and interoperability of power system measurement chains relying on accurate timing.

4.3 Test results

The performance of the three developed architectures, implementing the WR-based FPGA clock correction according to Algorithm 2, was assessed through dedicated tests, the results of which are discussed in this section. The first architecture, illustrated in Figure 4.1, was evaluated through two test configurations. In the first, referred to as the "GPS" test case, synchronization was achieved using the NI 9467 GPS board, which received the GPS synchronization

signal via a dedicated antenna. In the second, named the "GPS-WR" test case, synchronization relied on the PPS signal generated by the cRIO-WR module, itself synchronized through the WR protocol provided by the WR Switch, which in turn was disciplined by the Meinberg GPS receiver. The second architecture, shown in Figure 4.2, was likewise tested under the two configurations corresponding to the two WR Slave setups presented in the schematic. In the first case, the PPS signal generated by the WR ZEN was used, referred to as the "WR ZEN" configuration, whereas in the second, the PPS signal provided by the cRIO-WR module was employed, hereafter denoted as the "WR Module" configuration. The third and final architecture, shown in Figure 4.3, was tested in the single WR Slave configuration referred to as "GPS-WR-FPGA". In this setup, the PPS signal provided by the cRIO-WR module disciplined the Artix-7 FPGA clock. For each test case, once the FPGA clock was fully locked and transient effects were no longer observed, the FPGA clock offset was recorded for a duration of 2 hours.

Figure 4.4 shows the evolution of the offset of the FPGA clock with respect to the time reference (hereafter referred to simply as offset) as a function of time for all the performed tests. The datasets are superimposed for presentation purposes, although they do not correspond to the same time instants. Red dots represent the GPS case, green the GPS–WR case, blue the WR ZEN case, light blue the WR Module case, and purple the GPS–WR–FPGA case. This color legend will be consistently used throughout the result presentation. As a first observation, none of the five configurations exhibits any drift or repet-

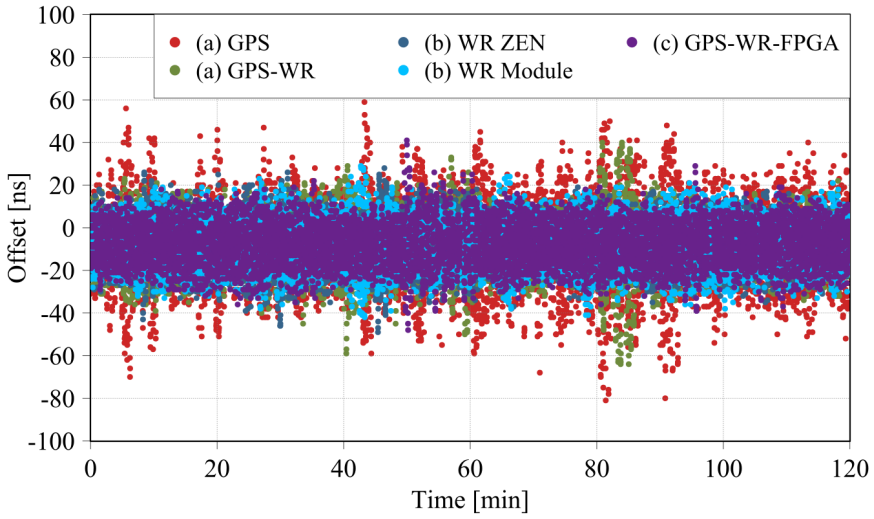

Figure 4.4: Evolution of the FPGA clock offset over time for the five analyzed synchronization configurations.

itive behavior, such as beats or modulations, providing a positive indication of the ergodicity of the data. It is also evident that the average offset is not zero but remains consistent across all configurations, with a value of approximately −8 ns. This average value remains constant over time and therefore represents a systematic error introduced by the system, likely caused by delays in the communication between the FPGA, the board, and the adopted LabVIEW Timekeeper library. Being practically constant, this offset can be easily compensated in real-world applications requiring accurate time tagging, such as synchrophasor estimation.

Regarding data variability, it is useful to refer to the Q-Q plot representation shown in Figure 4.5, which allows a statistical analysis of the distributions obtained for the five cases. The GPS and GPS–WR configurations exhibit the widest range of variation compared to the others, with the former showing peaks reaching approximately 60 ns and −80 ns. Conversely, the WR ZEN and WR Module cases do not display such fluctuations, and their data appear more tightly distributed. In the GPS-WR-FPGA configuration, the benefits in terms of determinism introduced by the full-FPGA scheme are evident, as the dispersion of the purple dots is comparable in magnitude to that observed during the METAS laboratory tests. It is particularly remarkable that such a level of performance was achieved without resorting to any reference-grade time source. In fact, comparable results were obtained while relying exclusively on the same GPS signal provided by the Meinberg Lantime M1000 used in the GPS

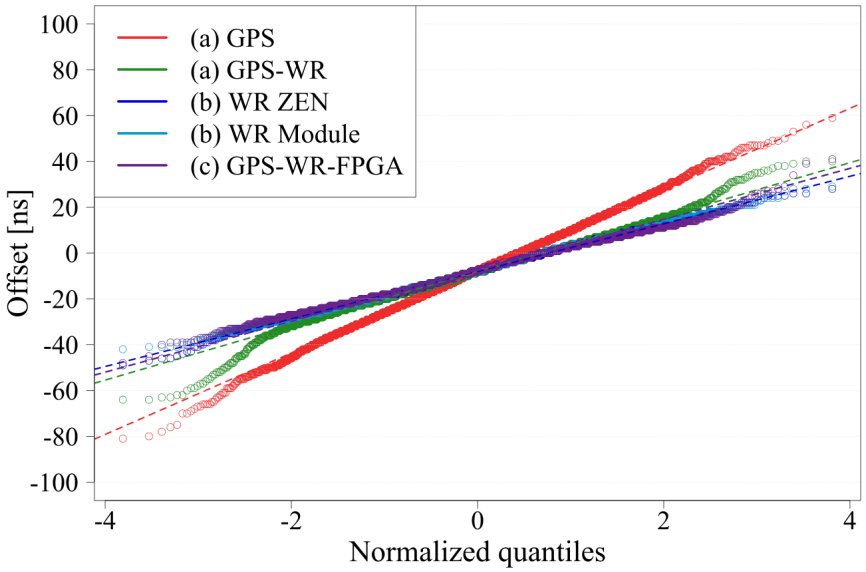

Figure 4.5: Q-Q plots of the offset measurements obtained during the five tests.

and GPS-WR tests, a commercial time source far less accurate and stable than that available in the metrological laboratory setup. This outcome highlights the intrinsic robustness and high degree of determinism of the full-FPGA synchronization scheme, capable of maintaining excellent stability even under standard operating conditions.

To complete the discussion and quantify the observations, Table 4.2 reports the most significant statistical parameters of the data collected in the five test configurations. The table shows that the average value μ does not vary appreciably among the five tests. In particular, the highest offset is observed in the GPS and GPS–WR configurations, and as shown in Figure 4.5, the GPS case exhibits the largest standard deviation σ. The standard deviations decrease significantly in the METAS test configurations, where values around 10.50 ns are achieved. The GPS–WR case, on the other hand, shows a σ comparable to that obtained in the METAS laboratory, although it should be noted that the GPS–WR test was performed using a more expensive high-performance GPS receiver compared to the NI board used in the GPS test. Consistently with the previous discussion, the best result is obtained in the GPS–WR–FPGA case, which achieves a standard deviation of 10.17 ns, as the architectural simplification led to a variability lower than those obtained in the METAS experiments.

Table 4.2: Summary of the main statistical parameters of the offset measurements for the five test configurations

Test	**Offset [ns]**			
	Max	Min	$\boldsymbol{\mu}$	$\boldsymbol{\sigma}$
(a) GPS	59	-81	-8.00	18.30
(a) GPS-WR	40	-64	-8.32	12.12
(b) WR ZEN	28	-49	-7.88	10.52
(b) WR Module	29	-42	-7.85	10.50
(c) GPS-WR-FPGA	41	-48	-7.79	10.17

In summary, the WR protocol provides the best performance in terms of uncertainty compared to the GPS-based configuration. Its combination with a minimal FPGA-based architecture, where delays and non-deterministic behaviors are limited, enables the full exploitation of its potential performance. Nonetheless, there remains room for improvement, as the 40 MHz maximum frequency and the intrinsic clock jitter of the FPGA prevent the achievement of the sub-nanosecond accuracy that WR can theoretically provide. These results confirm the potential of the proposed architecture, showing a significant improvement over the preliminary findings presented in [82] and outperforming typical configurations based on the Power Utility Profile (PUP) of the PTP [99].

4.4 Concluding remarks and practical implications for power systems

The proposed architectures for WR protocol distribution demonstrated excellent performance in terms of time accuracy. The analysis highlighted both the benefits and limitations arising from the choice of primary time sources and, above all, from the hardware used to receive and manage the WR signal at the endpoint, the WR Slave. The most remarkable outcome, leveraging the stability and precision offered by the WR system, was achieved with the GPS–WR–FPGA architecture. In this configuration, synchronization management after the fiber-based WR dissemination is entirely implemented on an FPGA platform. The dedicated programmable circuitry minimizes non-deterministic effects on clock alignment, yielding results comparable to those obtained with reference-grade time sources.

These results confirm the potential of WR as a robust synchronization technology for power system monitoring, where sub-microsecond timing accuracy can significantly enhance the performance of time-sensitive applications. Particularly promising examples include its integration into Merging Units (MUs) and Harmonic Phasor Measurement Units (H-PMUs).

Within the IEC 61850 framework, the WR protocol naturally fits within the context of the increasing sampling rates defined by the latest IEC 61869 standards [100], which reflect the demand for higher measurement accuracy and faster data availability in advanced protection and power quality applications. Modern MUs can now operate at tens or even hundreds of kilohertz, and in some cases up to the megahertz range, to support high-resolution waveform analysis and real-time event detection. As sampling frequencies rise, synchronization accuracy becomes increasingly critical to ensure data consistency across the network. Conventional Global Navigation Satellite System (GNSS)- or PTP-based systems approach their limits under sub-microsecond alignment requirements. By contrast, the WR framework offers deterministic, hardware-compensated synchronization with nanosecond-level precision over Ethernet, making it an ideal enabler for next-generation MUs and Intelligent Electronic Devices (IEDs) in digital substations.

In the MU-IED scheme, advanced functionalities for harmonic monitoring can also be integrated, supporting the analysis of disturbance propagation and the identification of dominant sources of voltage distortion. In such applications, synchronization accuracy plays a decisive role, as timing inaccuracies translate into Phase-Angle Errors (PEs) that are amplified at harmonic frequencies, directly affecting the estimation of phase-angles and, consequently, the reliability

of the computed harmonic phasors. Even small timing deviations can introduce phase shifts that scale with frequency, degrading the overall measurement accuracy and limiting the capability to perform coherent comparisons among geographically distributed units. The WR system therefore stands out as a key enabler for next-generation H-PMUs, where its nanosecond-level precision effectively mitigates these effects and reduces the phase-angle uncertainty that typically constrains harmonic measurements.

Conclusions

The rapid evolution of modern power grids, increasingly relying on communication-oriented architectures and high sampling-rate measurements, has made data quality and synchronization accuracy crucial aspects of reliable monitoring. In this context, this thesis addressed the problem of awareness and reliability of measurement data, proposing tailored methodologies and architectures developed with an application-oriented perspective and validated through extensive experimental campaigns. The research explored this broad theme along three complementary directions: improving measurement data interpretation in the presence of grid events through real-time event detection with Matrix Profile (MP); enhancing awareness of the statistical behavior of synchrophasor measurements through a statistical characterization of Phasor Measurement Unit (PMU) measurement errors; and adopting the White Rabbit (WR) protocol to achieve high-accuracy time synchronization and enable advanced monitoring and control applications in power systems.

The study on the MP focused on the identification of events in both Sampled Value (SV) streams and synchrophasor data at the Phasor Data Concentrator (PDC) level. The main contribution consisted in shifting the focus from traditional offline analysis of long time series to online processing over short windows with immediate feedback. This naturally entailed an assessment of the algorithm's execution time, as its purpose was no longer to perform a post-mortem analysis of time series but rather to provide timely and reliable indications in real time. The MP technique was characterized to achieve remarkable performance in detecting Power Quality (PQ) events such as voltage dips and, in the case of PDCs, was adapted to correlate events originating from separate synchrophasor data streams, thereby reproducing a realistic operating scenario. The outcome is a practical framework capable of detecting transients and data anomalies directly at the edge, improving situational awareness and enabling prompt reactions by downstream applications.

The study on the statistical behavior of PMU measurement errors was developed within a broader metrological context, aiming to establish a systematic and

replicable methodology for device characterization. It was observed that statistical models are often derived from heterogeneous datasets, which may distort the extraction of a representative model for the device under test. The proposed methodology was supported by a dedicated experimental architecture, specifically designed to minimize external influences that could otherwise alter the device behavior. The statistical investigation demonstrated that the Gaussian model provides a valid and effective description of the Magnitude Errors (MEs), once external factors and hidden trends are identified and mitigated. These results confirm that a rigorous experimental protocol and systematic treatment of uncertainty lead to a simple yet robust stochastic representation. The Phase-Angle Errors (PEs) exhibited a more complex behavior, as they can include deterministic components introduced by device synchronization mechanisms. The case study of a specific PMU model highlighted a clear deviation from ideal Gaussianity under high current operating conditions, emphasizing the importance of device-oriented characterization across different operating regimes.

The investigation on the WR protocol for device synchronization introduced and evaluated advanced architectures for its dissemination in real-field power system applications, quantifying their impact on timing performance. The design process followed a clear path aimed at maximizing determinism in the synchronization of the end device, namely the WR Slave. As an effective solution, a timing management architecture was proposed downstream of the optical link carrying the WR protocol, fully implemented on an Field Programmable Gate Array (FPGA) platform. By performing synchronization management within programmable logic, this approach minimized non-deterministic effects on clock alignment and achieved results comparable to those obtained in previous tests with reference-grade time sources. These findings confirmed the WR protocol as a robust technology for time-sensitive applications in power system monitoring.

Overall, the thesis contributed to strengthening the reliability and interpretability of measurement data through a unified methodological vision that integrates event detection, device characterization, and time synchronization. It shows that bringing intelligence closer to the measurement edge enables systems to move from simple data acquisition to active and context-aware information extraction. Moreover, the thesis stresses that a careful statistical and metrological analysis of instrument behavior is necessary to ensure that higher-level monitoring and control functions are based on reliable quantitative information. At the same time, the work highlights how accurate timing, enabled by the WR protocol, represents a key enabler for coherent and deterministic measurements across distributed infrastructures.

In a broader perspective, the presented studies outline a consistent path toward synchronized monitoring systems that are not only more accurate, but

also inherently more aware. Overall, these results aim to advance the trustworthiness of measurement data in digital substations and Wide Area Monitoring Systems (WAMSs), consolidating the link between data quality and system reliability. The significance of these results lies in their potential to open new frontiers, such as the development of realistic digital twins for emulating measurement uncertainty models and the design of advanced applications requiring reliably acquired and coordinated data at high sampling rates. Beyond the specific context of power systems, some of the proposed methodologies provide a transferable framework applicable to several domains within the field of measurement theory, including biomedical signal analysis such as Photoplethysmography (PPG) data processing.

Bibliography

[1] IEEE Std C37.118.2-2024 (Revision of IEEE Std C37.118.2-2011), *IEEE Standard for Synchrophasor Data Transfer for Power Systems*, 2024.

[2] *IEC 61850: Communication networks and systems for power utility automation*, International Electrotechnical Commission, 2021.

[3] A. Monti, C. Muscas, and F. Ponci, *Phasor Measurement Units and Wide Area Monitoring Systems*. Academic Press, 2016.

[4] *Measuring relays and protection equipment - Part 118-1: Synchrophasor for power systems - Measurements*, International Electrotechnical Commission, 2018.

[5] IEEE Std C37.247-2019, *IEEE Standard for Phasor Data Concentrators for Power Systems*, 2019.

[6] P. Castello, C. Muscas, P. A. Pegoraro, G. M. Giannuzzi, P. Pau, C. Maiolini, and R. Zaottini, "An Active Phasor Data Concentrator Suitable for Control and Protection Applications," in *2019 International Conference on Smart Grid Synchronized Measurements and Analytics (SGSMA)*, 2019.

[7] IEEE Std C37.244-2013, *IEEE Guide for Phasor Data Concentrator Requirements for Power System Protection, Control, and Monitoring*, 2013.

[8] A. Derviškadić, P. Romano, M. Pignati, and M. Paolone, "Architecture and Experimental Validation of a Low-Latency Phasor Data Concentrator," *IEEE Transactions on Smart Grid*, vol. 9, no. 4, 2018.

[9] K. Zhu, S. Rahimi, L. Nordström, and B. Zhang, "Design phasor data concentrator as adaptive delay buffer for wide-area damping control," *Electric Power Systems Research*, vol. 127, 2015.

[10] IEEE Std C37.118.2-2011 (Revision of IEEE Std C37.118-2005), *IEEE Standard for Synchrophasor Data Transfer for Power Systems*, 2011.

[11] P. Castello, G. Frigo, D. Sitzia, and S. Sulis, "Phasor Data Concentrator for Detection and Analysis of Events in Synchrophasor Data Streams," in *2025 IEEE 15th International Workshop on Applied Measurements for Power Systems (AMPS)*, 2025.

[12] *Communication networks and systems for power utility automation – Part 9-2: Specific Communication Service Mapping (SCSM) – Sampled values over ISO/IEC 8802-3*, International Electrotechnical Commission, 2011.

[13] UCA International Users Group, *Implementation guideline for digital interface to instrument transformers using IEC 61850-9-2*, 2004.

[14] M. Agustoni, P. Castello, and G. Frigo, "Phasor Measurement Unit With Digital Inputs: Synchronization and Interoperability Issues," *IEEE Transactions on Instrumentation and Measurement*, vol. 71, 2022.

[15] P. Castello, S. Sulis, G. Frigo, and M. Agustoni, "Power Quality Meters Based on Digital Inputs: A Feasibility Study," in *2022 20th International Conference on Harmonics & Quality of Power (ICHQP)*, 2022.

[16] Q. Yang, D. Keckalo, D. Dolezilek, and E. Cenzon, "Testing IEC 61850 Merging Units," in *2017 Western Protective Relay Conference*, 2017.

[17] J. Perez, "A guide to digital fault recording event analysis," in *2010 63rd Annual Conference for Protective Relay Engineers*, 2010.

[18] G. Cipolletta, A. D. Femine, D. Gallo, C. Landi, and M. Luiso, "Design approach for a stand alone merging unit," in *Proceedings of the 16th IMEKO TC10 Conference*, 2019.

[19] A. Mingotti, F. Costa, L. Peretto, and R. Tinarelli, "Characterization Procedure for Stand-Alone Merging Units Based on Hardware-in-the-Loop Technology," *Energies*, vol. 14, no. 7, 2021.

[20] J. Serrano, M Lipinski, T Wlostowski, E Gousiou, E. van der Bij, M Cattin, and G Daniluk, "The White Rabbit project," in *Proc. 2nd Int. Beam Instrumentation Conf.*, Sep. 2013.

[21] IEC Standard 61850-5:2013, *Communication Networks and Systems for Power Utility Automation – Part 5: Communication Requirements for Functions and Device Models*, 2013.

[22] IEC/IEEE Standard 61850-9-3-2016, *Communication Networks and Systems for Power Utility Automation – Part 9-3: Precision Time Protocol Profile for Power Utility Automation*, 2016.

[23] IEC/IEEE 61588-2021, *IEC/IEEE International Standard - Precision Clock Synchronization Protocol for Networked Measurement and Control Systems*, 2021.

[24] P. Castello, G. Gallus, P. A. Pegoraro, and S. Sulis, "Measurement Platform for Latency Characterization of Wide Area Monitoring, Protection and Control Systems," *IEEE Transactions on Instrumentation and Measurement*, vol. 73, 2024.

[25] *IEEE 1159-2019 - Recommended Practice for Monitoring Electric Power Quality*, 2019.

[26] *IEC 61000-2-5:2017 Electromagnetic compatibility (EMC) – Part 2-5: Environment – Description and classification of electromagnetic environments*, 2017.

[27] J. L. Afonso, M. Tanta, J. G. O. Pinto, L. F. C. Monteiro, L. Machado, T. J. C. Sousa, and V. Monteiro, "A Review on Power Electronics Technologies for Power Quality Improvement," *Energies*, vol. 14, no. 24, 2021.

[28] *IEC 61000-2-12:2003 - Electromagnetic compatibility (EMC) – Part 2-12: Environment – Compatibility levels for low-frequency conducted disturbances and signalling in public medium-voltage power supply systems*, International Electrotechnical Commission, 2003.

[29] P. Castello, C. Muscas, D. Sitzia, S. Sulis, and J. Rens, "Performance Analysis Based on Real-Field Data of a Method for Locating the Source of Voltage Dips," in *2023 IEEE 13th International Workshop on Applied Measurements for Power Systems (AMPS)*, 2023.

[30] *Electromagnetic compatibility (EMC) - Part 4-30: Testing and measurement techniques - Power quality measurement methods*, International Electrotechnical Commission, 2021.

[31] "IEEE Recommended Practice for Power Quality Data Interchange Format (PQDIF)," *IEEE Std 1159.3-2019 (Revision of IEEE Std 1159.3-2003)*, 2019.

[32] P. Castello, C. Muscas, P. A. Pegoraro, D. Sitzia, S. Sulis, G. M. Giannuzzi, M. Pede, C. Maiolini, P. Pau, F. Bassi, and C. Coluzzi, "Enhanced PMU-based Wide Area Measurement System with Integrated Power Quality and Fault Analysis," in *2022 International Conference on Smart Grid Synchronized Measurements and Analytics (SGSMA)*, 2022.

[33] C.-C. M. Yeh, Y. Zhu, L. Ulanova, N. Begum, Y. Ding, H. A. Dau, D. F. Silva, A. Mueen, and E. Keogh, "Matrix Profile I: All Pairs Similarity Joins for Time Series: A Unifying View That Includes Motifs, Discords and Shapelets," in *2016 IEEE 16th International Conference on Data Mining (ICDM)*, 2016.

[34] Y. Zhu, Z. Zimmerman, N. S. Senobari, C.-C. M. Yeh, G. Funning, A. Mueen, P. Brisk, and E. Keogh, "Matrix Profile II: Exploiting a Novel Algorithm and GPUs to Break the One Hundred Million Barrier for Time Series Motifs and Joins," in *2016 IEEE 16th International Conference on Data Mining (ICDM)*, 2016.

[35] P. Castello, S. Fullone, P. A. Pegoraro, and D. Sitzia, "Z-Normalized Euclidean Distance-Based Approach for Heart Rate Estimation and Artifact Identification in PPG Signals," in *2025 IEEE International Workshop on Metrology for Industry 4.0 & IoT (MetroInd4.0 & IoT)*, 2025.

[36] P. Castello, D. Sitzia, S. Sulis, and G. Frigo, "Utilizing Matrix Profile for Enhanced Detection of Events in Sampled Values," in *2024 IEEE 14th International Workshop on Applied Measurements for Power Systems (AMPS)*, 2024.

[37] P. Castello, G. Frigo, D. Sitzia, and S. Sulis, "Characterization of Matrix Profile Technique for Enhanced Detection of Events in Sampled Values Data Streams," *IEEE Transactions on Instrumentation and Measurement*, vol. 74, 2025.

[38] M. Bollen, "Voltage recovery after unbalanced and balanced voltage dips in three-phase systems," *IEEE Transactions on Power Delivery*, vol. 18, no. 4, 2003.

[39] M. S. Manikandan, S. R. Samantaray, and I. Kamwa, "Detection and Classification of Power Quality Disturbances Using Sparse Signal Decomposition on Hybrid Dictionaries," *IEEE Transactions on Instrumentation and Measurement*, vol. 64, no. 1, 2015.

[40] M. De Santis, C. Noce, P. Varilone, and P. Verde, "Analysis of the origin of measured voltage sags in interconnected networks," *Electric Power Systems Research*, vol. 154, pp. 391–400, 2018.

[41] C. Noce, M. D. Santis, L. D. Stasio, P. Varilone, and P. Verde, "Detecting the Origin of the Voltage Sags Measured in the Smart Grids," in *2019 International Conference on Clean Electrical Power (ICCEP)*, 2019.

[42] P. Castello, C. Muscas, P. A. Pegoraro, S. Sulis, G. M. Giannuzzi, M. Pede, C. Maiolini, P. Pau, F. Bassi, and C. Coluzzi, "Integration of power quality and fault data into a PMU-based Wide Area Monitoring System," in *2021 IEEE 11th International Workshop on Applied Measurements for Power Systems (AMPS)*, 2021.

[43] Y. Ge, A. J. Flueck, D.-K. Kim, J.-B. Ahn, J.-D. Lee, and D.-Y. Kwon, "Power System Real-Time Event Detection and Associated Data Archival Reduction Based on Synchrophasors," *IEEE Transactions on Smart Grid*, vol. 6, no. 4, 2015.

[44] D.-I. Kim, T. Y. Chun, S.-H. Yoon, G. Lee, and Y.-J. Shin, "Wavelet-Based Event Detection Method Using PMU Data," *IEEE Transactions on Smart Grid*, vol. 8, no. 3, 2017.

[45] S. Hasan, K. M. Muttaqi, and D. Sutanto, "Detection and Characterization of Time-Variant Nonstationary Voltage Sag Waveforms Using Segmented Hilbert–Huang Transform," *IEEE Transactions on Industry Applications*, vol. 56, no. 4, 2020.

[46] M. He, Z. Teng, A. Mingotti, Q. Tang, H. Wen, and L. Peretto, "A Novel Approach to Automatically Detect Power Quality Disturbances Based on Dynamic Pocket Network," in *2023 IEEE 13th International Workshop on Applied Measurements for Power Systems (AMPS)*, 2023.

[47] S. Zhong and A. Mueen, "MASS: distance profile of a query over a time series," *Data Mining and Knowledge Discovery*, vol. 38, 2024.

[48] J. Shi, N. Yu, E. Keogh, H. K. Chen, and K. Yamashita, "Discovering and Labeling Power System Events in Synchrophasor Data with Matrix Profile," in *2019 IEEE Sustainable Power and Energy Conference (iSPEC)*, 2019.

[49] *Power quality measurement in power supply systems - Part 2: Functional tests and uncertainty requirements*, International Electrotechnical Commission, 2021.

[50] *Electromagnetic compatibility (EMC) - Part 4-15: Testing and measurement techniques - Flickermeter - Functional and design specifications*, International Electrotechnical Commission, 2010.

[51] *Instrument transformers - The use of instrument transformers for power quality measurement*, International Electrotechnical Commission, 2012.

[52] S. G. Mallat, "A theory for multiresolution signal decomposition: The wavelet representation," *IEEE Transactions on Pattern Analysis and Machine Intelligence*, vol. 11, no. 7, 1989.

[53] S. Santoso, W. M. Grady, E. J. Powers, J. Lamoree, and S. C. Bhatt, "Characterization of distribution power quality events with fourier and wavelet transforms," *IEEE Transactions on Power Delivery*, vol. 15, no. 1, 2000.

[54] M. Battilana, *Robust Peak Detection Algorithm Using Z-Scores*, `https://github.com/MatteoBattilana/robust-peak-detection-algorithm`, 2014.

[55] M. Fritsch and M. Wolter, "High-Frequency Current Transformer With Variable Air Gap for Power Cable Monitoring," *IEEE Transactions on Instrumentation and Measurement*, vol. 73, 2024.

[56] A. J. Wilson, A. Riza Ekti, J. Follum, S. Biswas, C. Annalicia, J.-Y. Joo, O. Aziz, and J. Lian, "The Grid Event Signature Library: An Open-Access Repository of Power System Measurement Signatures," *IEEE Access*, vol. 12, 2024.

[57] G. Frigo, P. A. Pegoraro, and S. Toscani, "Tracking power system events with accuracy-based PMU adaptive reporting rate," *International Journal of Electrical Power & Energy Systems*, vol. 153, 2023.

[58] S. M. Law, "STUMPY: A Powerful and Scalable Python Library for Time Series Data Mining," *Journal of Open Source Software*, vol. 4, no. 39, 2019.

[59] P. Castello, C. Muscas, P. A. Pegoraro, D. Sitzia, and S. Sulis, "On the Variability of Random Errors Distribution in PMUs: An Experimental Characterization," in *2025 IEEE International Instrumentation and Measurement Technology Conference (I2MTC)*, 2025.

[60] P. Castello, G. Gallus, C. Muscas, P. A. Pegoraro, D. Sitzia, and S. Sulis, "A Statistical Investigation of PMU Errors in Current Measurements," in *2023 IEEE International Instrumentation and Measurement Technology Conference (I2MTC)*, 2023.

[61] M. Pau and P. A. Pegoraro, "WLS-Based State Estimation for Unobservable Distribution Grids Through Allocation Factors Evaluation," *IEEE Transactions on Instrumentation and Measurement*, vol. 73, 2024.

[62] D. Carta, A. Benigni, C. Sitzia, P. A. Pegoraro, and S. Sulis, "Performance Assessment of Synchronized Phasor Measurement-Based Parameter Estimation for Distribution Networks," in *2022 International Conference on Smart Energy Systems and Technologies (SEST)*, 2022.

[63] P. A. Pegoraro, C. Sitzia, A. V. Solinas, S. Sulis, D. Carta, and A. Benigni, "Improved Fault Detection and Location Method in Three-Phase Distribution Networks Leveraging Traceable PMU Measurements," *IEEE Transactions on Instrumentation and Measurement*, vol. 74, 2025.

[64] T. Ahmad and N. Senroy, "Statistical Characterization of PMU Error for Robust WAMS Based Analytics," *IEEE Transactions on Power Systems*, vol. 35, no. 2, 2019.

[65] C. Huang, C. Thimmisetty, X. Chen, E. Stewart, P. Top, M. Korkali, V. Donde, C. Tong, and L. Min, "Power Distribution System Synchrophasor Measurements With Non-Gaussian Noises: Real-World Data Testing and Analysis," *IEEE Open Access Journal of Power and Energy*, vol. 8, 2021.

[66] G. Na, W. Song, C. Lu, and X. Chen, "Gaussian Mixture Models and its Parameter Estimation to Describe the Distributions of PMU Random Errors in Power Systems," in *2023 10th International Conference on Power and Energy Systems Engineering (CPESE)*, 2023.

[67] S. Wang, J. Zhao, Z. Huang, and R. Diao, "Assessing Gaussian Assumption of PMU Measurement Error Using Field Data," *IEEE Transactions on Power Delivery*, vol. 33, no. 6, 2018.

[68] D. Salls, J. R. Torres, Antos, C. Varghese, J. Patterson, and A. Pal, "Statistical Characterization of Random Errors Present in Synchrophasor Measurements," in *2021 IEEE Power & Energy Society General Meeting (PESGM)*, 2021.

[69] S. Čubonović, D. Ćetenović, and A. Ranković, "The Impact of the Non-Gaussian Measurement Noise on the Performance of State-of-the-Art State Estimators for Distribution Systems," en, *Serbian Journal of Electrical Engineering*, vol. 21, no. 1, 2024.

[70] P. Castello, C. Muscas, and P. A. Pegoraro, "Statistical Behavior of PMU Measurement Errors: An Experimental Characterization," *IEEE Open Journal of Instrumentation and Measurement*, vol. 1, 2022.

[71] A. Mingotti, L. Peretto, R. Tinarelli, A. Angioni, A. Monti, and F. Ponci, "Calibration of Synchronized Measurement System: from the Instrument Transformer to the PMU," 2018.

[72] C. Laurano, P. A. Pegoraro, C. Sitzia, A. V. Solinas, S. Sulis, and S. Toscani, "Refined Modeling and Compensation of Current Transformers Behavior for Line Parameters Estimation Based on Synchronized Measurements," *IEEE Open Journal of Instrumentation and Measurement*, vol. 2, 2023.

[73] *Omicron CMC 256plus*, https://www.omicronenergy.com/en/products/cmc-256plus/.

[74] R. R. Aleixo, T. S. Lomar, L. R. M. Silva, H. L. M. Monteiro, and C. A. Duque, "Real-Time B-Spline Interpolation for Harmonic Phasor Estimation in Power Systems," *IEEE Transactions on Instrumentation and Measurement*, vol. 71, 2022.

[75] J. Li, H. Liu, and T. Bi, "Tunnel Magnetoresistance-Based Noncontact Current Sensing and Measurement Method," *IEEE Transactions on Instrumentation and Measurement*, vol. 71, 2022.

[76] R. Murray and J. A. de Kock, "Quantifying the Impact of Varying Inductive Burden When Inductive Current Transformers Are Used for Harmonic Current Measurements for Grid Code Compliance," *IEEE Transactions on Instrumentation and Measurement*, vol. 73, 2024.

[77] J. Klusacek, R. Langella, J. Meyer, and J. Drapela, "Performance of Smart Revenue Meters Under Bidirectional Active Energy Flows in Energy Communities," *IEEE Transactions on Instrumentation and Measurement*, vol. 73, 2024.

[78] *8588a reference multimeter*, https://us.flukecal.com/products/electrical-calibration/bench-multimeters/8588a-reference-multimeter.

[79] S. S. Shapiro and M. B. Wilk, "An analysis of variance test for normality (complete samples)," *Biometrika*, vol. 52, no. 3/4, 1965.

[80] *R: The R Project for Statistical Computing*, https://www.r-project.org/.

[81] *IEEE Synchrophasor Measurement Test Suite Specification–Version 3*, Jul. 2019.

[82] G. Frigo, P. Castello, G. Gallus, P. A. Pegoraro, and S. Toscani, "Internal Time Reference Enhancement via White Rabbit Synchronization: A Power System Measurement Perspective," in *Proc. 2024 Int. Conf. on Smart Grid Synchronized Measurements and Analytics*, May 2024.

[83] IEEE Standard 1588-2019, *IEEE Standard for a Precision Clock Synchronization Protocol for Networked Measurement and Control Systems*, 2020.

[84] J. L. Gutiérrez-Rivas, F. Torres-González, E. Ros, and J. Díaz, "Enhancing White Rabbit synchronization stability and scalability using P2P transparent and hybrid clocks," *IEEE Transactions on Industrial Informatics*, vol. 17, no. 11, Nov. 2021.

[85] IEEE Standard 802.3-2018, *IEEE Standard for Ethernet*, 2018.

[86] ITU-T Recommendation G.8262, *Timing Characteristics of Synchronous Ethernet Equipment Slave Clock*, 2007.

[87] E. Waterman, M. Helm, J. Zirngibl, and H. Stubbe, "White Rabbit: High precision PTP," in *Seminar Innovative Internet Technologies and Mobile Communications*, Aug. 2020-Mar. 2021.

[88] J. Aweya, "Implementing synchronous Ethernet in telecommunication systems," *IEEE Commun. Surveys Tuts.*, vol. 16, no. 2, 2nd Quarter 2014.

[89] A. Derviškadić, G. Frigo, and M. Paolone, "Impact of Time Dissemination Technologies on Synchrophasor Estimation Accuracy," in *Proc. Int. Conf. on Smart Grid Synchronized Measurements and Analytics*, May 2019.

[90] N. Kaur, F. Frank, J. Pinto, P. Tuckey, and P.-E. Pottie, "A 500-km Cascaded White Rabbit Link for High-Performance Frequency Dissemination," *IEEE Trans. Ultrason., Ferroelectr., Freq. Control*, vol. 69, no. 2, Feb. 2022.

[91] IEC Technical Report 61850-90-5:2012, *Communication Networks and Systems for Power Utility Automation - Part 90-5: Use of IEC 61850 to Transmit Synchrophasor Information According to IEEE C37.118*, 2012.

[92] C. M. Adrah, D. Palma, Øivind Kure, and P. E. Heegaard, "A network design algorithm for multicast communication architectures in smart transmission grids," *Electric Power Systems Research*, vol. 187, 2020.

[93] D. Husmann, J. Faist, F. Mauchle, F. Merkt, S. Willitsch, and J. Morel, "Swiss Fiber Network for Dissemination of Optical Frequencies in the L-band of a Telecommunication Network," in *Proc. 2022 European Conf. on Optical Communication*, Sep. 2022.

[94] F. Levi, D. Calonico, A. Mura, M. Frittelli, C. Calosso, M. Zucco, C. Clivati, G. A. Costanzo, R. Ambrosini, G. Galzerano, P. De Natale, D. Mazzotti, N. P. D. V. Sutyrin, and G. M. Tino, "LIFT-the Italian link for time and frequency," in *Proc. 2013 Joint European Frequency and Time Forum & Int. Frequency Control Symp.*, Jul. 2013.

[95] M. Lipiński, T. Włostowski, J. Serrano, and P. Alvarez, "White rabbit: A PTP application for robust sub-nanosecond synchronization," in *2011 IEEE International Symposium on Precision Clock Synchronization for Measurement, Control and Communication*, 2011.

[96] *Safran WR Switch - Low Jitter*, `https://safran-navigation-timing.com/white-rabbit-switch-low-jitter`.

[97] *CompactRIO White Rabbit (CRIO-WR)*, `https://gitlab.com/ohwr/project/crio-wr/-/wikis/home`.

[98] A Jallageas, L Devenoges, M Petersen, J Morel, L. G. Bernier, D Schenker, P Thomann, and T Südmeyer, "First uncertainty evaluation of the FoCS-2 primary frequency standard," *Metrologia*, vol. 55, no. 3, Apr. 2018.

[99] D. Macii and S. Rinaldi, "Time Synchronization for Smart Grids Applications: Requirements and Uncertainty Issues," *IEEE Instrumentation & Measurement Magazine*, vol. 25, no. 6, 2022.

[100] IEC Standard 61869-9:2016, *Instrument transformers - Part 9: Digital Interface for Instrument Transformers*, 2016.

List of Figures

List of Tables

Acronyms

AC Alternating Current

ACF Autocorrelation Function

ADC Analog-to-Digital Converter

CDF Cumulative Distribution Function

CERN European Organization for Nuclear Research

CNN Convolutional Neural Network

CPU Central Processing Unit

cRIO CompactRIO

d@PDC detection at PDC level

DAQ Data Acquisition

DC Direct Current

DFR Digital Fault Recorder

DP Distance Profile

DRAM Dynamic Random Access Memory

DUT Device Under Test

DWT Discrete Wavelet Transform

FFT Fast Fourier Transform

FoCS-2 Fontaine Continue Suisse

FPGA Field Programmable Gate Array

fps frame per second

FSR Full-Scale Range

GESL Grid Event Signature Library

GMM Gaussian Mixture Model

GNSS Global Navigation Satellite System

GOOSE Generic Object Oriented Substation Event

GPS Global Positioning System

H-PMU Harmonic Phasor Measurement Unit

HiL Hardware-in-the-Loop

I/O Input/Output

IED Intelligent Electronic Device

IRIG Inter-Range Instrumentation Group Timecodes

IT Instrument Transformer

MASS Mueen's Algorithm for Similarity Search

ME Magnitude Error

METAS Federal Swiss Institute of Metrology

ML Machine Learning

MMS Manufacturing Message Specification

MP Matrix Profile

MU Merging Unit

MZS Modified Z-Scores

NI National Instruments

NTP Network Time Protocol

OCXO-MQ Master Quality Oven Controlled Crystal Oscillator

ORNL Oak Ridge National Laboratory

OSI Open Systems Interconnection

PDC Phasor Data Concentrator

PDF Probability Density Function

PE Phase-Angle Error

PMU Phasor Measurement Unit

PPG Photoplethysmography

PPS Pulse per Second

PQ Power Quality

PQDIF Power Quality Data Interchange Format

PQM Power Quality Meter

PTP Precision Time Protocol

PUP Power Utility Profile

R-GOOSE Rootable GOOSE

R-SV Rootable Sampled Value

RAM Random-Access Memory

RMS Root Mean Square

ROCOF Rate of Change of Frequency

RT Real-Time

RVC Rapid Voltage Change

SAMU Stand-Alone Merging Unit

SCADA Supervisory Control and Data Acquisition

SFP Small Form-factor Pluggable

SNR Signal-to-Noise Ratio

SOC System-on-Chip

STAMP Scalable Time series Anytime Matrix Profile

STOMP Scalable Time series Ordered-search Matrix Profile

SV Sampled Value

SW Shapiro-Wilk

SyncE Sync Ethernet

TCP Transmission Control Protocol

THD Total Harmonic Distortion

TSO Transmission System Operator

TVE Total Vector Error

UDP User Datagram Protocol

USB Universal Serial Bus

UTC Coordinated Universal Time

WAMS Wide Area Monitoring System

WR White Rabbit

List of Publications

Journal articles

- P. Castello, G. Frigo, D. Sitzia, and S. Sulis, "Characterization of Matrix Profile Technique for Enhanced Detection of Events in Sampled Values Data Streams," *IEEE Transactions on Instrumentation and Measurement*, vol. 74, 2025

Conference papers

- P. Castello, C. Muscas, P. A. Pegoraro, D. Sitzia, S. Sulis, G. M. Giannuzzi, M. Pede, C. Maiolini, P. Pau, F. Bassi, and C. Coluzzi, "Enhanced PMU-based Wide Area Measurement System with Integrated Power Quality and Fault Analysis," in *2022 International Conference on Smart Grid Synchronized Measurements and Analytics (SGSMA)*, 2022.

- P. Castello, G. Gallus, C. Muscas, P. A. Pegoraro, D. Sitzia, L. Campisano, G. M. Giannuzzi, C. Maiolini, and P. Pau, "Latency Characterization of a Wide Area Monitoring Protection and Control Application in the Italian Transmission System," in *2022 IEEE 12th International Workshop on Applied Measurements for Power Systems (AMPS)*, 2022.

- P. Castello, G. Gallus, C. Muscas, P. A. Pegoraro, D. Sitzia, and S. Sulis, "A Statistical Investigation of PMU Errors in Current Measurements," in *2023 IEEE International Instrumentation and Measurement Technology Conference (I2MTC)*, 2023.

- P. Castello, C. Muscas, D. Sitzia, S. Sulis, and J. Rens, "Performance Analysis Based on Real-Field Data of a Method for Locating the Source of Voltage Dips," in *2023 IEEE 13th International Workshop on Applied Measurements for Power Systems (AMPS)*, 2023.

- D. Sitzia, P. Castello, C. Muscas, P. A. Pegoraro, S. Sulis, and S. Yildiz, "Performance Evaluation of Particulate Matter Low-Cost Sensors Under Power Supply Variations," in *2024 IEEE International Instrumentation and Measurement Technology Conference (I2MTC)*, 2024.
- P. Castello, C. Muscas, P. A. Pegoraro, D. Sitzia, and S. Sulis, "Influence of Apparent Wind on Particulate Matter Monitoring through Low-Cost Sensors," in *2024 IEEE International Workshop on Metrology for Industry 4.0 & IoT (MetroInd4.0 & IoT)*, 2024.
- P. Castello, D. Sitzia, S. Sulis, and G. Frigo, "Utilizing Matrix Profile for Enhanced Detection of Events in Sampled Values," in *2024 IEEE 14th International Workshop on Applied Measurements for Power Systems (AMPS)*, 2024.
- P. Castello, P. A. Pegoraro, D. Sitzia, and S. Sulis, "PMU Measurement Accuracy Awareness Provided by Power Quality Indices," in *2024 21st International Conference on Harmonics and Quality of Power (ICHQP)*, 2024.
- P. Castello, C. Muscas, P. A. Pegoraro, D. Sitzia, and S. Sulis, "On the Variability of Random Errors Distribution in PMUs: An Experimental Characterization," in *2025 IEEE International Instrumentation and Measurement Technology Conference (I2MTC)*, 2025.
- C. Cazal, Y. Kannan, D. Sitzia, G. Frigo, P. A. Pegoraro, F. Ponci, and A. Monti, "Harmonic Measurement in DC: a Case for Synchrophasors," in *2025 IEEE International Instrumentation and Measurement Technology Conference (I2MTC)*, 2025.
- P. Castello, S. Fullone, P. A. Pegoraro, and D. Sitzia, "Z-Normalized Euclidean Distance-Based Approach for Heart Rate Estimation and Artifact Identification in PPG Signals," in *2025 IEEE International Workshop on Metrology for Industry 4.0 & IoT (MetroInd4.0 & IoT)*, 2025.
- P. Castello, G. Frigo, D. Sitzia, and S. Sulis, "Phasor Data Concentrator for Detection and Analysis of Events in Synchrophasor Data Streams," in *2025 IEEE 15th International Workshop on Applied Measurements for Power Systems (AMPS)*, 2025.

Oral presentations

- Poster presentation of the paper: D. Sitzia, P. Castello, C. Muscas, P. A. Pegoraro, S. Sulis, and S. Yildiz, "Performance Evaluation of Particulate

Matter Low-Cost Sensors Under Power Supply Variations," in *2024 IEEE International Instrumentation and Measurement Technology Conference (I2MTC)*, 2024.

- Presentation of the paper: P. Castello, C. Muscas, P. A. Pegoraro, D. Sitzia, and S. Sulis, "Influence of Apparent Wind on Particulate Matter Monitoring through Low-Cost Sensors," in *2024 IEEE International Workshop on Metrology for Industry 4.0 & IoT (MetroInd4.0 & IoT)*, 2024.

- Presentation of the paper: P. Castello, G. Frigo, D. Sitzia, and S. Sulis, "Phasor Data Concentrator for Detection and Analysis of Events in Synchrophasor Data Streams," in *2025 IEEE 15th International Workshop on Applied Measurements for Power Systems (AMPS)*, 2025.